Investigation of high-power diode lasers by spectroscopic techniques

vorgelegt von
Master of Science
Tien Quoc Tran
aus Hanoi, Vietnam

von der Fakultät IV – Elektrotechnik und Informatik
der Technischen Universität Berlin
zur Erlangung des akademischen Grades
Doktor der Naturwissenschaften
- Dr. rer. nat. -

genehmigte Dissertation

Promotionsausschuss:

Vorsitzender:	Prof. Dr.-Ing. Klaus Petermann
Berichter:	Prof. Dr. rer. nat. Günther Tränkle
Berichter:	Prof. Dr.-Ing. Christian Boit

Tag der wissenschaftlichen Aussprache: ***26. November 2007***

Berlin 2008
D 83

Zusammenfassung

Hochleistungslaserdioden (HPDL) überstreichen den Wellenlängenbereich vom Sichtbaren bis ins nahe Infrarot und erreichen Gesamtwirkungsrade von über 70 %. Trotzdem stellen Probleme mit der Langzeitstabilität immer noch einen Engpass dar. Daher erscheinen weitere analytische Arbeiten sinnvoll, insbesondere wenn sie zur Verbesserung von Herstellungstechnologien dienen.

In dieser Arbeit wird die optische Spektroskopie als Hauptwerkzeug eingesetzt. Dabei wird ein Schwerpunkt auf die photoelektrische Spektroskopie gelegt, was die Nutzung von Methoden wie der Photostromspektroskopie (PCS), Laserstrahl-injizierte Ströme (LBIC) und Nahfeld-injizierte Ströme (NOBIC) einschließt.

Im experimentellen Teil zeigen wir, wie es gelang die PCS-Technik den Erfordernissen von Messungen an verschiedenen HPLDs anzupassen. Das schloss den Aufbau neuer Messplätze für Messungen von Photoströmen (PC) an Bauelementen, die definierten externen Verspannungen ausgesetzt waren, sowie zur Messung von unkonfektionierten Proben, ein. Arbeiten zur Kalibrierung der PCS-Methode mit anderen optischen Techniken vervollständigen das Wissen.

Wir haben Schlüsseleigenschaften von Halbleiterlasern erforscht, die den Herstellungsprozess, mechanische Verspannungen, thermische Durchstimmeigenschaften, Defekte, sowie das Wechselspiel zwischen Verspannungen und Defekten einschließen.

1. Mechanische Verspannungen in Halbleiterlasern als eine Hauptquellen von Degradationsprozessen wurden quantifiziert. Durch Analyse mehrer optischer Übergänge im QW war es in bestimmten Fällen sogar möglich, Aussagen zur Symmetrie der Deformation des Kristallgitters zu machen. Derartige Aussagen sind mit konkurrierenden Methoden, wie der Raman-Spektroskopie meist nicht möglich. Wesentliche neue Ergebnisse beinhalten:

- Wir zeigen erstmals Ergebnisse über Verspannungsuntersuchungen an HPDL-Stacks mit Hilfe von photoelektrischen Messmethoden.
- Die zeitliche Entwicklung von mechanischen Verspannungen wurde während des Betriebes der Bauelemente unter hoher Last beobachtet und quantifiziert.
- Die Beobachtung und Analyse von zusätzlichen Verspannungsbeiträgen, die in der Nähe von geätzten Separationsgräben auftreten. Wir zeigen, dass dieser Verspannungsbeitrag eng an die durch Konfektionierung eingebrachte Verspannung gekoppelt ist, aber eine höhere Symmetrie aufweist (z.B. zweiachsig).

2. Wir erforschten die thermischen Durchstimmeigenschaften von HPDLs am Arbeitspunkt.

- Erstmalig wurde dabei eine Temperaturabhängigkeit der Durchstimm-Rate gefunden. Zusätzlich gelang die Separation desjenigen Beitrages, der seine eigentliche Ursache im Abbau von uniaxialem, durch Konfektionierung eingebrachtem Druck, bei erhöhten Temperaturen hat.

- Der Vergleich der Durchstimmeigenschaften von Standard- und ausdehnungsangepassten (Cu und Cu-W) Wärmesenken zeigt eine substanzielle Verbesserung der Homogenität der thermischen Durchstimmeigenschaften beim Einsatz letzterer.

3. Mikroskopische Defekte spielen eine wichtige Rolle im Verständnis der Alterungsprozesse, die an HPDLs beobachtet werden. Defekte werden innerhalb der Bauelementearchitektur lokalisiert und Schlüsselparameter wie Aktivierungsenergien bestimmt.

- Die Dynamik von Defektsignaturen während des Bauelementebetriebes deutet insbesondere bei solchen Bauelementen auf eine Konzentrationszunahme hin, in denen auch vor der Alterung Defekte nachweisbar waren.
- Wir führten die ersten photoelektrischen Analysen an rot emittierenden Bauelementen aus. Die Analyse tiefer Zentren mittels NOBIC zeigte, dass diese unmittelbar mit dem im Wellenleiter geführten Licht interagieren können.

4. Wir diskutieren die Wechselwirkung von Verspannungen und Defekten in HPDLs. Bei Erhöhung der Konzentration von Defektzentren in Einzelemittern wurde eine Zunahme kompressiver Verspannungen beobachtet. Dabei ist es möglich zwischen dem Einfluss unterschiedlicher Defektzentren zu unterscheiden. Zentren mit Niveaulagen in der Mitte der Bandlücke, flache Zentren und Zustände im Zustandsdichteschwanz zeigen völlig unterschiedliche funktionale Zusammenhänge zwischen ihrer Konzentration und der beobachteten mechanischen Deformation des Kristallgitters in ihrer Umgebung. Es gibt eine starke Korrelation zwischen dem Auftreten flacher Zentren und einer Gitterdeformation, während Zentren mit Niveaulagen nahe der Mitte der Bandlücke offenbar keinen nachweisbaren Einfluss auf die Gitterdeformation haben. Diese neue Art der Analyse sollte hilfreich bei der Aufstellung von Szenarien sein, welche Degradationsabläufe zu erklären versuchen und so schlussendlich helfen, Schwachstellen in Bauelementekonstruktionen und Technologien aufzuspüren.

Wir gehen davon aus, dass unsere experimentellen Ansätze auch auf andere optoelektronische Bauelemente übertragbar sind.

List of abbreviations

HPDL	High Power Diode Laser
PC	Photocurrent
PCS	Photocurrent Spectroscopy
μPCS	Micro Photocurrent Spectroscopy
LBIC	Laser Beam Induced Current
NOBIC	Nearfield Optical Beam Induced Current
PL	Photoluminescence
μPL	Micro Photoluminescence
EL	Electroluminescence
CL	Cathodoluminescence
DOP	Degree of Polarization
ROP	Rotating Degree of Polarization
FT	Fourier Transform
SNR	Signal to noise ratio
BA	Broad-area
hh	heavy-hole
lh	light-hole
e	electron
QW	Quantum well
SQW	Single Quantum well
DQW	Double Quantum well
MOVPE	Metalorganic Vapor Phase Epitaxy
COMD	Catastrophic Optical Mirror Damage
SOT	Small Outline Transitor
FEM	Finite Element Method

Contents

Introduction

High-power diode lasers (HPDLs) are coherent light sources and cover the wavelength region from red (630 nm) to the near-infrared (1600 nm). These devices are the base of many applications such as in materials processing, telecommunications, health-care applications, solid-state laser pumping, optical data storage, RGB-laser display, etc. During the last 20 years, HPDL technology has impressively developed. Recently, the HPDLs as a special segment of overall semiconductor laser market are growing annually [1-3]. HPDLs-systems are becoming more compact with the products based on HPDL array technology. A typical type of HPDL arrays is the laser bar that is usually 1 cm in lateral width and therefore called cm-bar. In 2006, Jenoptik Laserdiode reported a continuous-wave optical output power of above 500 W from one single HPDL cm-bar [4]. Another achievement of HPDL technology is the high power conversion efficiency, which has surpassed the value of 70 % [5]. These facts show an enormous potential of the HPDLs.

However, also this technology still requires improvements to meet novel applications, in particular for the “information society” of tomorrow. For this purpose, there are some research projects on HPDLs in the European Union. One of them is the WWW.BRIGHT.EU project [6] that orientates studies towards new concepts of HPDLs, namely high-brightness laser diodes. A high value of the parameter “brightness” can be obtained by the improvement of HPDL fabrication technology with the goal of minimizing the beam divergence and maximizing the output power. Many current applications, e.g. Raman and Erbium doped fiber amplification, cutting/welding of sheet metal, surgery and photodynamic therapy, are expecting high-brightness laser diodes. In this project, HPDL bars with multi-emitters play a key role. Almost all efforts are concentrated on improving their properties (growing, processing and packaging) and coupling the output power from the bar by optical fiber or micro-optics. Another objective of the project is to cover market demand after devices for special wavelength regions, e.g. improvements of red-emitting devices for health-care

applications or 9xx nm for telecommunications. So far, high-brightness laser diodes still suffer certain reliability problems. Therefore, the objective of long-lifetime high-brightness laser diodes pushes the research on reliability forward. Although the device lifetime of some kinds of HPDLs is relatively long, reliability problems related to HPDLs represent still a bottleneck. For example, while the lifetime of 9xx nm emitting HPDLs can reach the value of hundred thousand hours [7], red-emitting devices provide reliable operation of a few thousands hours only [8,9]. An important part of the work reported in thesis was done within the framework of the project WWW.BRIGHT.EU.

The reliability of HPDLs is strongly correlated with two issues, namely external strains and the generation and/or motion of defects. Strains can be generated in quantum-well (QW) structures of HPDLs at various stages of the fabrication and testing process. Considering devices after a certain operation time, the observed *external* strains, i.e. such that are introduced after the epitaxial growth, in HPDL arrays are caused by following contributions:

- processing-induced strain (deposition of metallization layers, etching of grooves, etc),
- packaging-induced strain, and
- strain created by the generation of defects.

The external strains are one major source of degradation processes, which take place within HPDL arrays. Therefore, they directly influence the reliability of these devices. Defects in HPDLs are also known as source of degradation. They play an important role in all degradation scenarios, e.g. their creation becomes enhanced in the high power operation regime of HPDL bars, thus accelerating the degradation process. The reaction of them with other phenomena occurring in degradation process is very complex [10-12]. Therefore, knowledge about defects in specific device structures as well as in particular operation regimes is always required in order to minimize them at least in the device fabrication process.

In many of these cases, non-destructive methods are needed to be applied if the devices under test must be further available after the measurements for further investigations. For example, after the initial measurements, further next stages of aging must be monitored if we attempt to observe strain and defect evolutions during operation.

A further strong motivation for the introduction, test, and application of spectroscopic methods for device analysis is the search for screening methods. Screening of devices, i.e. a selection of devices based on their expected lifetime, would be extremely useful for industry, since conventional lifetime tests are both costly and time-consuming.

Now we consider the methodology related to the analysis of HPDLs. The study method should give enough information but minimize the measuring effort. The selected methodologies should, e.g., include the capability to predict degradation. This allows to reduce the testing time (typically is thousand hours) at expensive aging stages. Among all available methods, the optical techniques show advantages and the potential to fulfill most requirements. By using a screening method, namely laser beam induced current (LBIC), and spectroscopic methods after screening such as photocurrent spectroscopy (PCS) or photoluminescence (PL) related techniques, we are able to avoid long time aging test with costly equipment, but still get enough information about the degradation process. However, in some particular cases, a more complex technique such as near-field optical beam induced current (NOBIC) and destructive method such as cathodoluminescence (CL) need to be applied as complementary investigation tools to get more knowledge about the nature of physical phenomena in HPDLs.

The above collected arguments motivate our studies on reliability of HPDLs in the framework of the EU project WWW.BRIGHT.EU. The analyses will base on optical techniques that are mostly non-destructive methods and deliver important results. The investigations are carried out to provide additional information (origin, nature, mechanism and interaction with other parameters) that helps improving fabrication technology and eventually the lifetime of the devices. In this thesis, we will concentrate on the analysis of strain and defects, on the relation between these parameters, and how their interplay accompanies the degradation processes. The thesis will be organized as following:

- First, a brief introduction on some fundamental optical properties of quantum semiconductor structures that are relevant is done in chapter 1. The key problem, the relation between strains and resulting modifications of electronic band structure of semiconductor QWs, is outlined in detail.
- The experimental methodology and apparatus for the application of photoelectrical techniques including PCS, micro-photocurrent spectroscopy (μPCS), LBIC, NOBIC and PL related techniques, e.g. μPL and polarized PL, which are used as main investigation tools, will be presented in the first part of chapter 2. After that, descriptions of the HPDLs under test provide information about epitaxial structures and the lateral layout of devices as well as their basic device characteristics as determined by standard characterization.
- In chapter 3, we deal with strain analysis in HPDL arrays that are usually influenced by packaging-induced stresses. The investigation is based on optical techniques (PCS, μPCS, μPL, and polarized PL). The results from various experimental approaches of this chapter show a reliable strain measurement methodology to determine the strain present in HPDL arrays.

- Chapter 4 focuses on the discussion about results of thermal tuning properties of HPDLs in relation to other parameters, e.g. strain.
- The defects and defect-related degradation effects in HPDLs are the main topic of chapter 5. By using optical techniques, we are able to monitor the evolution and determine the location of defects in HPDL structures. Beside that, the results in this chapter show that the optical techniques can provide a possibility to predict degradation by monitoring particular signatures, e.g. existence of defects or broadening of Urbach parameter.
- Chapter 6 will discuss the correlation between strain and defects. Analyzing the interplay between strain and defects provides a clearer understanding of strain and defects creation scenarios that can contribute to the improvement of device performance during the fabrication process.

Finally, the summary concludes the thesis.

Chapter 1.

Optical properties of quantum semiconductor structures

1.1. Optical spectra of quantum semiconductor structures

1.1.1. Interband absorption in quantum wells

Interband transitions between valence and conduction band states determine the optical properties of GaAs-based semiconductor quantum wells (QWs) in the visible and near infrared ranges of the electromagnetic spectrum. Figure 1.1 represents interband optical transitions in a typical AlGaAs/GaAs QW structure. The interband absorption spectrum shows structures, which provide important information about the status of the QWs, e.g. shifts of band edges of layers, the presence of band tail states, and the energetic spacing between discrete levels within the QWs of a device structure.

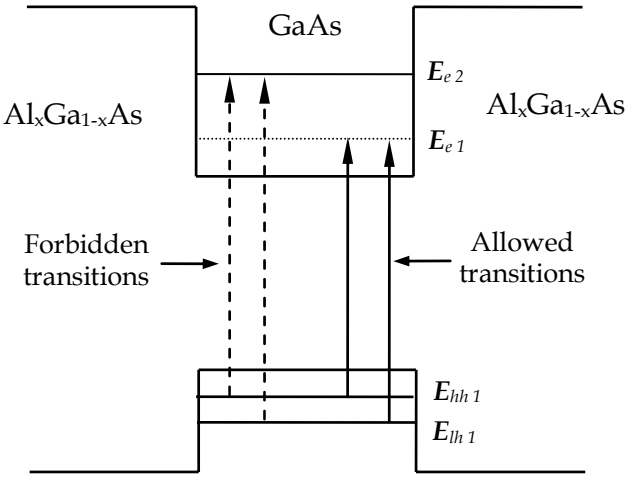

Figure 1.1: Interband optical transitions in a QW

In this section, we introduce essential points of the interband absorption in semiconductor QW structures.

We assume the electromagnetic wave to be gradually absorbed when it propagates through materials. However, in the case of QWs, the absorption is localized within a very thin layer (two-dimensional), which thickness is smaller than de Broglie wavelength. Therefore, the calculation of the absorption coefficient for QW structures must involve the presence of quantum effects.

The interband absorption coefficient in a QW structure is calculated based on interband transition probabilities for particles confined in the QW that is given by Fermi's golden rule [13-15]. The expression for the dimensionless relative interband absorption between states ***n*** and ***n'*** given by:

$$\alpha = \frac{(2\pi e)^2}{\omega c\sqrt{\varepsilon}L^2}\sum_{nn'}\left|\langle n|\mathbf{e}\cdot\hat{\mathbf{v}}|n'\rangle\right|^2\delta(E_n - E_{n'} + \hbar\omega)(f_n - f_{n'}) \quad , \qquad (1.1)$$

where **e** is unit vector in the direction of polarization; $\hat{\mathbf{v}}$ is the electron velocity operator; $\boldsymbol{\omega}$ is excitation photon frequency; f_n and $f_{n'}$ are Fermi functions of ***n*** and ***n'*** states and L^2 is the normalized area. This formula explicitly relates the optical properties of a QW to its electronic energy spectrum E_n and the matrix elements of the velocity operator $\hat{\mathbf{v}}$.

In the vicinity of the band edge, the energy dispersion of electrons and holes can be assumed to be parabolic. In assumption of a filled valence band and an empty conduction band (i.e., setting Fermi functions $f_v = 1$ and $f_c = 0$), we obtain the following expression for the absorption spectrum:

$$\alpha = \frac{e^2}{\omega c\sqrt{\varepsilon}}\sum_{nn'} p_{nn'}(\mathbf{e})\rho_{nn'}(\hbar\omega) \quad , \qquad (1.2)$$

where $p_{nn'}$ (**e**) is a polarization-dependent factor and $\rho_{nn'}$ ($\hbar\omega$) is the joined density of states, which is represented by the following expression:

$$\rho_{nn'}(\hbar\omega) = A\,(\hbar\omega - E_{nn'})\frac{m_{nn'}}{\pi\hbar^2} \quad , \qquad (1.3)$$

$$\frac{1}{m_{nn'}} = \frac{1}{m_{cn}} + \frac{1}{m_{nn'}} \quad , \qquad (1.4)$$

In the above expressions A is a constant; $E_{nn'}$ is the transition energy between the bottom of subband ***n*** and ***n'***; $\boldsymbol{m}_{cn}$ and $\boldsymbol{m}_{cn'}$ are the effective masses of respective subbands. $\boldsymbol{m}_{nn'}$ is called the reduced mass for this pair of subbands.

Figure 1.2 shows the resulting variation of absorption versus excitation photon energy in a QW and bulk (for comparison). In both cases, the absorption is proportional to the respective joined density of states. Therefore, while in the bulk the absorption varies as $(\hbar\omega - E_g)^{1/2}$, in QWs the absorption does not change for one pair of subbands. According to (1.1), each pairs of subbands contributes a step to the absorption spectrum, in case that the transition are allowed (i.e. the matrix element $p_{nn'}$ is nonzero). As more subbands are involved in the QW, the absorption has a staircase-like shape [16,17].

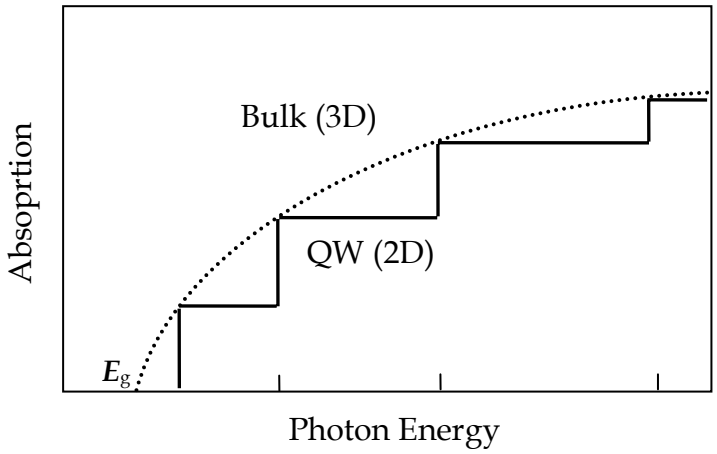

Figure 1.2: Expected variation of absorption in a QW (solid) and in bulk (dotted)

The absorption spectrum presented in Figure 1.2, however, only occurs in case of an ideal QW structure with non-interacting carriers. In practice, the absorption spectrum is strongly modified by broadening phenomena and exciton effects [15,18]. The broadening phenomenon is quite pronounced in experimental spectra and makes the absorption spectrum differ from rectangular steps not only on the left but also on the right side of a step. Figure 1.3 shows the broadening phenomenon in absorption spectrum of an individual step of QW. This behaviour depends on the presence of a number of factors such as temperatures, growth conditions, doping level, density of carriers, strength of electron-electron and electron-phonon interaction, etc. [15]. The second effect, which we should mention here, is

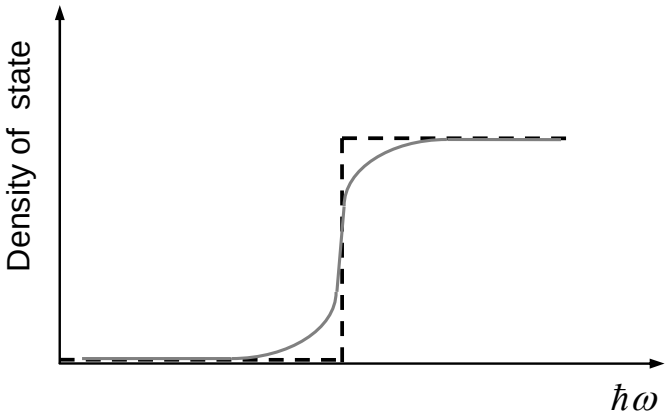

Figure 1.3: Broadening of an individual step in QW (dash line: no broadening; solid line: broadening effect).

appearance of excitonic absorption peaks in the absorption spectra. The exciton is a bound state of electron and hole. The excitons arise because of the Coulomb interaction between carriers. Since there are two kinds of holes: heavy and light holes, they lead to two respective exciton types (hh-e and lh-e transitions) with different binding energies [19]. These exciton transitions are observed in absorption spectra of QW structures. Figure 1.4 represents an absorption spectrum including exciton effects.

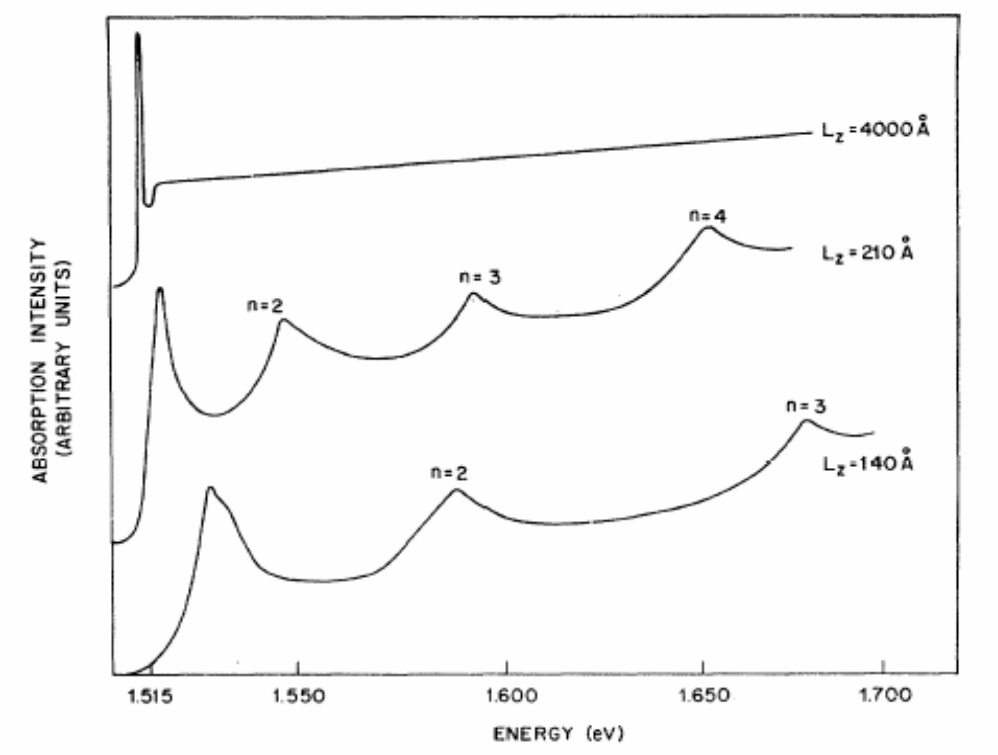

Figure 1.4: Exciton effect in absorption spectra from QW and bulk GaAs at 2 K [20].

1.1.2. Selection rules and quantum-well absorption spectra

In the preceding section, we did not address effects that are caused by polarized electromagnetic waves and influence the absorption spectrum. This section will discuss the polarization dependence of interband transitions in QW structures that are related to the selection rule of optical transitions in quantum semiconductors.

Many semiconductor materials are condensed as cubic crystals, and their linear optical properties are isotropic. The anisotropy factor, which is contained in the inteband matrix element, is absent in case of bulk materials because of the high symmetry. However, this factor is important for QW structures and in quantum confined systems in general even when the energy spectrum, $\boldsymbol{E_n}$, and the distribution function, f_n, are spin-independent and isotropic in a two-dimension plane. It depends

on the orientation of the electric field vector of the electromagnetic radiation with respect to the direction of growth of QW [15,16].

To understand the origin of the anisotropy factor, which makes matrix element in QW polarization dependent, we reproduce the expression for squared matrix elements of bulk semiconductor, p_{if} (detailed explanation see Ref. [16]). We consider highly symmetric directions only and take $k = 0$. Note that i and f represent initial and final state, respectively, and *hh-e* and *lh-e* denotes transitions from the heavy-hole level to the conduction band and the light-hole level to the conduction band, respectively. We now obtain:

- z-polarization:

$$\textbf{\textit{hh-e}}: \text{ no coupling } (|p_{if}|^2 = 0) \quad , \qquad (1.5.\text{ a})$$

$$\textbf{\textit{lh-e}}: |p_{if}|^2 = (2/3)\, p_{cv}^2 \quad , \qquad (1.5.\text{ b})$$

- x-polarization:

$$\textbf{\textit{hh-e}}: |p_{if}|^2 = (1/2)\, p_{cv}^2 \quad , \qquad (1.6.\text{ a})$$

$$\textbf{\textit{lh-e}}: |p_{if}|^2 = (1/6)\, p_{cv}^2 \quad , \qquad (1.6.\text{ b})$$

- y-polarization:

$$\textbf{\textit{hh-e}}: |p_{if}|^2 = (1/2)\, p_{cv}^2 \quad , \qquad (1.7.\text{ a})$$

$$\textbf{\textit{lh-e}}: |p_{if}|^2 = (1/6)\, p_{cv}^2 \quad , \qquad (1.7.\text{ b})$$

where p_{cv}^2 is momentum matrix element for transitions between conduction and valence band [16].

In all cases, the total contribution from *hh-e* and *lh-e* states to the squared matrix element for all polarizations is $(2/3)\, p_{cv}^2$. Moreover, the field is assumed to be along one of the symmetry directions. However, in practice, the electromagnetic field can be along an arbitrary direction. Therefore, the magnitude of $|p_{if}|^2$ will be changed.

In QWs, we denote the growth direction (i.e., <001> direction) as the z-direction (see Figure 1.5). If the electric field vector is along the y-direction the field is transverse electric (TE) polarized. It is called transverse magnetic (TM) polarized if the field vector is along z-direction.

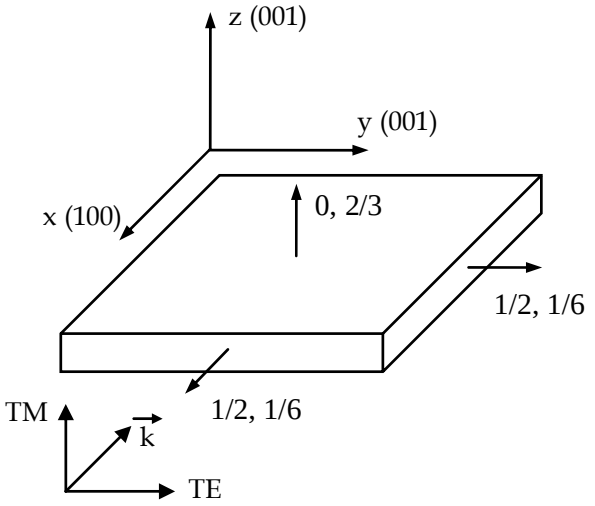

Figure 1.5: Relative band edge optical transition strengths (***hh, lh***) of a QW structure [21].

We now rewrite the above

results for TE and TM polarizations:

- TE polarization:

$$\textbf{\textit{hh-e}} : |p_{if}|^2 = (1/2)\, p_{cv}^2 \quad , \qquad (1.8.\text{ a})$$

$$\textbf{\textit{lh-e}} : |p_{if}|^2 = (1/6)\, p_{cv}^2 \quad , \qquad (1.8.\text{ b})$$

- TM polarization:

$$\textbf{\textit{hh-e}} : |p_{if}|^2 = 0 \quad , \qquad (1.9.\text{ a})$$

$$\textbf{\textit{lh-e}} : |p_{if}|^2 = (2/3)\, p_{cv}^2 \quad , \qquad (1.9.\text{ b})$$

These results know as selection rules for optical transitions in quantum wells absorption spectra in the particular case of a incident field polarized along the x-direction in the QW plane. Normalizing the magnitudes of the matrix element, we obtain the relative strengths of absorption in the QW in Table 1.1.

Table 1.1: Dipole selection rules for in-plane absorption

	TE polarization	TM polarization
hh-e transition	3/4	0
lh-e transition	1/4	1

The values in this table are used to analyse *hh-e* and *lh-e* absorption peaks that appear in the QW absorption spectra in experiments with the polarized excitation electromagnetic fields.

In general, for finite values of *k*, the values of the anisotropy factor are altered. If we define a quantity $\cos\theta = E(k)/E$ that represents the arbitrary polarization direction, the anisotropy factors can be expressed as in Table 1.2.

Table 1.2: Anisotropy factors for absorption transitions in QWs

	TE	TM
hh-e transition	$\frac{3}{4}(1+\cos^2\theta)$	$\frac{3}{2}\sin^2\theta$
lh-e transition	$\frac{1}{4}(5-3\cos^2\theta)$	$\frac{1}{2}(4-3\sin^2\theta)$

Based on these polarization characteristics of the optical transitions in QWs, we can distinguish and quantify them in our experimental absorption spectra.

1.1.3. Defect-related absorption in semiconductor structures

Defects play an important role in semiconductors. They strongly influence optical properties and cause, e.g., degradation effects in semiconductor devices. Defects are imperfections of crystal structure or are caused by the presence of foreign atoms in the semiconductor. In this section, we mainly focus on point defects in a specific approach that is based on their activation energy because this can provide a direct correlation to absorption spectrum of a semiconductor structures.

A shallow defect resembles a hydrogen atom with a positive nucleus (hole) binding an electron. Therefore, we can use hydrogen atom model (effective mass approximation) for the calculation of properties such as ionization energy (i.e. activation energy) and state wave functions [22,23]. At room temperature, shallow defects are frequently degenerated with extended band tail states. Thus they may contribute to the Urbach parameter [24] that tells us about the smoothness of the epitaxial layers in semiconductor structures. The ionization energy of shallow defect levels is comparable to the thermal energy kT=26 meV at room temperature, i.e. it is on the order of several ten meV. Therefore, the shallow defect levels are energetically located close to the band edges (see Fig. 1.6).

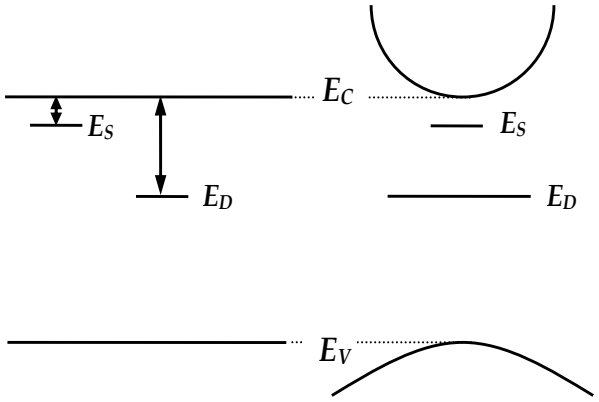

Figure 1.6: Illustration of a shallow and a deep level in real space and momentum space [25].

Strongly localized defects generate the deep levels within the forbidden gap. They can not be described by the hydrogen model (non-hydrogen-like defect). The deep level problem can be solved if there are suitable means of solving the Schrödinger equation with a strong, short-range potential. The deep defect levels are caused not only by point defects but also by spatially extended defects (e.g. dislocations, surface states) [25]. The energy levels of deep defects are more separated from the band edges (Figure 1.6). In many cases, they are close to the center of the gap. The name “midgap level” is frequently used for such deep levels. The activation energy of the deep defect levels is much higher than kT.

In the investigation of defects, it is convenient for explanation of experiments when we describe the defect levels by corresponding activation energies, so called “level depths”, which can be fitted in absorption spectra according to Ref. [26].

Now, we discuss the contribution of defects to the absorption spectra of QW semiconductor structures. In the staircase-like shape absorption spectra of QWs, the

lowest absorption edge is caused by transition between hh1- and e1-levels. For convenience in discussion, it is called hh1-e1 edge. When light illuminates into the semiconductor structures, both types of optical transitions, interband and defect, are involved into the absorption process. The optical transitions caused by defects will appear at energy contributions energetically below the hh1-e1 absorption edge. The level depth of a defect level (ΔE_{di}) we define as the distance between respective level (E_{di}) and hh1-e1 edge (E_{hh}). The defect level E_{di} is taken from onset position of defect band, which appears in an absorption spectrum. Thus, the depth of the i^{th} level can be determined as following: (ΔE_{di}) = (E_{di}) - (E_{hh}). The intensity of defect levels in absorption spectra can provide relative defect concentrations in QW structures.

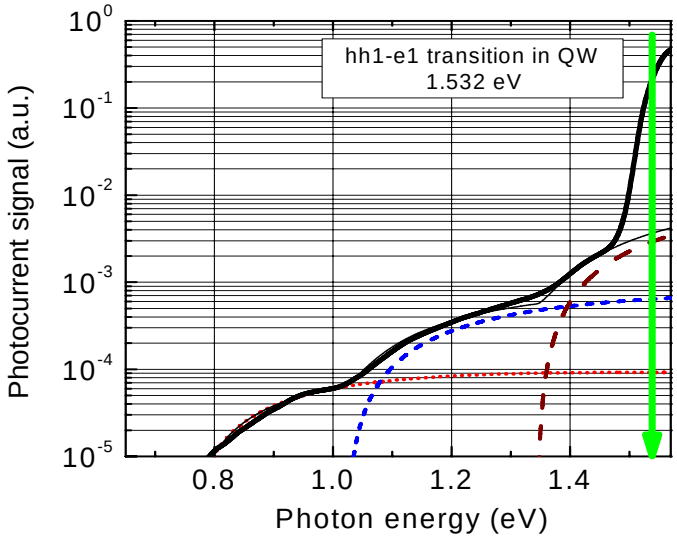

Figure 1.7: Fourier transform photocurrent spectrum of a QW structure from a HPDL showing defect-related absorption: the arrow marks onset of hh1-e1 transition in QW; the dotted, short dashed and dashed lines are fits corresponding to deep defect levels [27].

Figure 1.7 shows a Fourier Transform photocurrent (FT PC) spectrum of a QW structure from a HPDL. This spectrum partly resembles the absorption spectrum for in-plane absorption. Therefore, in many cases, we can use it as absorption spectrum. A detailed explanation of the mechanisms contributing to PC spectra will be presented in the next section. In Fig. 1.7, we see a distinct contribution of defect bands below the hh1-e1 edge at 1.532 eV as “shoulders” in the FT PC spectrum. The numerical analysis of the spectrum by calculating defect absorption bands according to an early model established in Ref. [26]. The onset of defect level absorption is located at 0.752, 1,021 and 1.347 eV. The three lines (dotted, short dashed and dashed) mark fits corresponding to three deep levels ($\Delta E_1 = (0.78 \pm 0.02)$ eV and $\Delta E_2 = (0.51 \pm 0.02)$ eV and $\Delta E_3 = (0.185 \pm 0.020)$ eV), whereas the full line is the sum of the three

contributions, which perfectly matches the experiment in the spectral range before the onset of the hh1-e1 optical transition.

1.1.4. Generation of photocurrent spectra in semiconductors

PCS is used as an alternative to absorption spectroscopy. It is one of the early techniques [28,29] and widely applied in studies of semiconductor structures, especially in semiconductor optoelectronic devices, e.g. solar cells [30,31], diode lasers [32,33]. The analysis of PCS, sometimes, is rather difficult because there are several effects contributing to the photocurrent of semiconductor structures.

In PCS, the generation of a photocurrent can be separated into two main processes. Firstly, the semiconductor structure is illuminated by an excitation beam (white light sources or lasers). The photons reaching the sample surface are absorbed and subsequently create non-equilibrium electron-hole pairs. For excitation photon energy above the bandgap of a semiconductor material, the absorption occurs close to the surface. The photons, which have energies lower than the bandgap, are penetrated deeper into the structure if there is no defect level. The penetration depth depends on the absorption coefficient of the semiconductor material at the particular excitation wavelength and determines the “depth resolution” of the PCS technique. Absorption generates non-equilibrium carriers that might be either free or localized in Coulomb-wells formed, e.g., by the QW or defect centers. At room-temperature, i.e. the standard temperature for device testing, these bound carriers, get immediately freed by thermionic emission. Therefore one calls them quasi-free [34]. At low temperature, tunneling dominates the escape even in a single QW and introduces strong field dependence to the effective activation barrier [30].

Non-equilibrium carriers can contribute to a photocurrent by their motion. The motion might be either caused by internally built-in or externally applied electric fields. This might be the potential of a pn-junction or be induced by an external bias, respectively. The spatial extent of these fields increases the effective diffusion length [35]. The carrier motion due to the external or internal field is measured as the photocurrent after the electric circuit is closed externally by an Ampere meter. The PCS technique has a certain “self-focusing” capability because the carriers generated by photons that get absorbed in regions without potential gradients, e.g. in the substrate, can not contribute to the PCS. Therefore, despite the whole semiconductor structure facet is illuminated, e.g. front facet of diode lasers; information comes exclusively from the depletion region around the pn-junction, i.e. from the optical active region of these diode lasers [34].

Additionally, there are two phenomena influencing the generation of photocurrents, namely surface and bulk recombination of photo-generated electron-

hole pairs [25,36]. They may significantly reduce the photocurrent signal in measurements.

Although PCS is weak in absolute quantification of absorption because of the influence of several complicated processes, it still contains information about relative absorption. Therefore, the PCS technique may also be considered a method for measuring the absorption spectrum along semiconductor structures, e.g. waveguides (including the QWs) of optoelectronic devices. These spectra provide information such as absorption of defects (Fig. 1.7), interband absorption edge, excitonic absorption peaks, etc. Moreover, polarized photocurrent spectra also allow analyzing and distinguishing between interband transitions in QW structures.

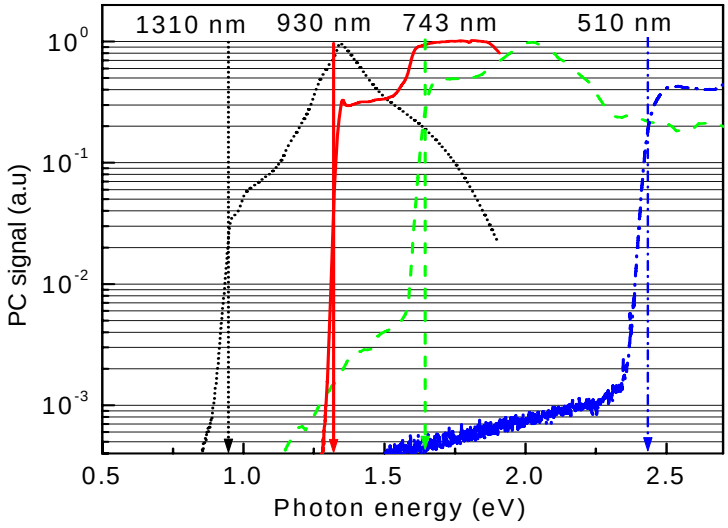

Figure 1.8: Normalized photocurrent spectra obtained from four diode lasers with different emission wavelengths [34].

Figure 1.8 shows normalized photocurrent spectra obtained from four different diode lasers, namely from 1.3 μm (dotted line) and 930 nm (full line) mono-mode QW diode lasers as well as spectra from 743 nm (dashed line) and 510 nm (dashed-dotted line) emitting diode laser devices. The emission photon energies and wavelength are marked by arrows (same type as the corresponding spectra) and labels, respectively [34].

1.2. Modification of Quantum well band structure in presence of strain

1.2.1. Elastic properties of semiconductors

The elastic properties of semiconductors strongly influence other characteristics, e.g. the optical properties. An elastic deformation of semiconductor

crystal causes a shifting of electronic band structure and thus changing of absorption and emission properties. In this section, we will introduce briefly the essential points of these properties.

Stress, i.e. force per unit area, which is applied to a semiconductor causes strain in the crystal lattice (change of the lattice constant). For sufficiently small deformations of the crystal, the relation between strain and stress obeys Hooke's law, i.e. the strain is directly proportional to the stress [37] :

$$\boldsymbol{\sigma}_{ij} = \boldsymbol{C}_{ijkl}\boldsymbol{\varepsilon}_{kl}, \quad , \qquad (1.10)$$

where $\boldsymbol{C}$ is a 4th order tensor called the elasticity tensor (or Young's modulus) and the components $\boldsymbol{C}_{ijkl}$ are called the *elastic stiffness constants* (or moduli of elasticity); $\boldsymbol{\sigma}$ and $\boldsymbol{\varepsilon}$ are symmetric 2nd order tensors of stress and strain, respectively. *Shear* components $\boldsymbol{\sigma}_{ij}$ $(i \neq j)$ of stress will cause the crystal to rotate or twist unless the equal and opposite components exist. If equal and opposite components do exist, the shear stress will deform a cubic lattice into nonrectangular shape (i.e., the crystal axes will become non-orthorgonal). *Normal* components $\boldsymbol{\sigma}_{ij}$ $(i = j)$ of stress will cause the crystal to expand or contract along the crystal axes, but in contrast to the action of shear stresses, the deformed lattice remains rectangular. Alternatively, we also can rewrite (1.15) as follows:

$$\boldsymbol{\varepsilon}_{ij} = \boldsymbol{S}_{ijkl}\boldsymbol{\sigma}_{kl} \quad , \qquad (1.11)$$

with $\boldsymbol{S}$ is the tensor of elastic modulus in which the quantities $\boldsymbol{S}_{ijkl}$ are called *elastic compliance constants***.**

The number of independent elastic stiffness constants is reduced if the crystal has symmetry elements. In the cubic crystal, the 36 constants of both $\boldsymbol{C}_{ijkl}$ and $\boldsymbol{S}_{ijkl}$ reduce to three (i.e., only three stiffness constants are independent). If shear components are absent the relation between stress and strain can be reduced as:

$$\begin{bmatrix} \sigma_{xx} \\ \sigma_{yy} \\ \sigma_{zz} \end{bmatrix} = \begin{bmatrix} C_{11} & C_{12} & C_{12} \\ C_{12} & C_{11} & C_{12} \\ C_{12} & C_{12} & C_{11} \end{bmatrix} \begin{bmatrix} \varepsilon_{xx} \\ \varepsilon_{yy} \\ \varepsilon_{zz} \end{bmatrix} \quad , \qquad (1.12)$$

In common semiconductors, C_{11}, $C_{12} > 0$ with $C_{11} > C_{12}$, and both are usually described in units of 10^{11} dyn/cm^2. Now, we consider three particular cases, namely hydrostatic, biaxial and uniaxial (stresses or strain) that will be frequently assumed in discussion about strain of semiconductor structures. The detail calculation for relation between stress and strain was done in Refs. [21,38,39]

- ***Hydrostatic strain:***

When three stress components are equal ($\boldsymbol{\sigma}_{xx} = \boldsymbol{\sigma}_{yy} = \boldsymbol{\sigma}_{zz} = \boldsymbol{\sigma}$), the crystal suffers hydrostatic strain. The three strain components are consequently the same ($\boldsymbol{\varepsilon}_{xx} = \boldsymbol{\varepsilon}_{yy} = \boldsymbol{\varepsilon}_{zz} = \boldsymbol{\varepsilon}$). If the stress is directed outward ($\boldsymbol{\sigma} > 0$), the resulting strain is referred to as

hydrostatic *tensile* strain, while the inward stress ($\sigma < 0$) causes a hydrostatic *compressive* strain. The tensile and compressive strain concepts are analogous to biaxial strain and uniaxial strain.

- ***Biaxial strain:***

The biaxial strain is an effect that happens when the stress is applied to all x and y faces of the cube such that ($\sigma_{xx} = \sigma_{yy}$), and no stress is acted to the z faces, such that ($\sigma_{zz} = 0$). In semiconductor structures, the growth of epilayers with a lattice constant different from the substrate causes biaxial strain in the epilayer. The resulting lattice deformation can be calculated using (1.12). By symmetry, with $\sigma_{xx} = \sigma_{yy} = \sigma$, the strain in both x and y directions must be equal and we can set $\varepsilon_{xx} = \varepsilon_{yy} = \varepsilon$. Under biaxial strain, the lattice deformation along the z direction will be opposite to the deformation along either x or y directions.

- ***Uniaxial strain:***

Stress may be applied along one direction of a crystals. In this case, uniaxial strain appears (for example, x direction). The stress components along y and z directions do not exist ($\sigma_{yy} = \sigma_{zz} = 0$). This strain configuration matches packaging-induced strain arising in HPDL bar, which represent a main focus in the thesis.

1.2.2. Modification of the band structure under stress

The modification of the electronic band structure due to strain is an important property of semiconductor structures. With the above knowledge on how a particular stress leads to a particular strain, we now discuss about the relationship between strain and band structure of semiconductors.

The detailed explanations and calculations of band structure under stress for bulk semiconductor are provided by Refs. [16,21,38]. The fundamental theory describes how lattice deformations affect the Hamiltonian has been provided by Pikus and Bir [40]. The strain effect was treated as strain perturbation to the Hamiltonian that allows describing the interaction between the bands: the heavy-hole, the light-hole, and split-off bands. To build a Hamiltonian that involves strain, the Luttinger-Kohl (L-K) model was used [41]. In this method, the various wave vectors appearing in L-K Hamiltonian and Luttinger's parameters were substituted by strain tensor components and lattice deformation potentials which relate shifts of the valence band to the strain tensor. An additional strain-dependent spin-orbit interaction Hamiltonian [42,43] also exists, however, the deformation potentials associated with this interaction are more than an order of magnitude smaller [42] than those associated with Pikus-Bir Hamiltonian. Therefore it will be neglected. When we consider the existence of strain in a crystal, there will be two energy components contributing to the Hamiltonian

(called H and S in the following). They are related to the strain tensor through lattice deformation potentials.

The component H is proportional to the change in volume of the lattice crystal lattice created by strain. H is referred to as the hydrostatic component of the strain. The energy H appears with the same sign in every diagonal terms of the Hamiltonian. Therefore, we conclude that changes in crystal volume result in a rigid shift of all three valence bands either up or down in energy, depending on whether the volume change is positive or negative.

The energy S represents the shear components. The shear strain energy is proportional to the asymmetry in the strain parallel and perpendicular to the stress plane. The heavy-hole band is isolated from the other two bands, however, the light-hole and split-off band are coupled through non-diagonal term ($\sqrt{2}\,S$). If S is negligible compared to spin-orbit energy (E_{so}), the coupling between light-hole band and split-off band can be neglected, and the dominant contribution from S shows up in the heavy-hole and light-hole diagonal terms, where it is seen to split the heavy-hole and light-hole band in opposite directions.

The strain Hamiltonian is written in terms of the hole energy, and a positive energy moves further into the valence band. For biaxial compressive strain, H and S are both positive, indicating an increase in the bandgap and the energy of the heavy-hole is lower than that of the light-hole. For biaxial tensile strain, H and S are both negative and the light-hole energy shifts to lower energy than heavy-hole. Figure 1.9 shows the band edge shifts of the three valence bands for both types of biaxial strain. The conduction band experiences a shift due to the hydrostatic component of the strain only. We can define a separate ΔE_c with a corresponding deformation potential

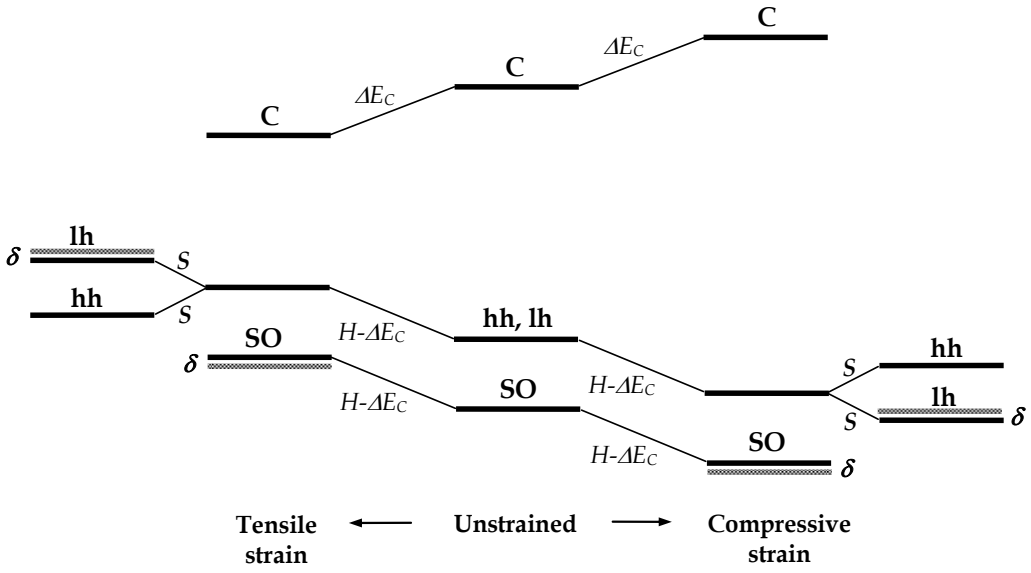

Figure 1.9: Qualitative band energy shift of conduction band and three valence bands for biaxial compressive and tensile strain. The grey energies include lh-SO band coupling [21].

associated with the motion of conduction band. The experiment performing to separate the ΔE_c from the total bandgap has been done by Nolte and et al. [44]. Mostly, we are only interested in total strained bandgap shift that is visible in the absorption spectra.

To quantify the energy shift, we have to evaluate H and S. Now we consider an example for the quantification of the energy shift in case of applied biaxial strain. With assumption of only normal components of stresses considered, we get detailed results for H and S as following. The strains due to lattice mismatch are given by:

$$\varepsilon_{xx} = \varepsilon_{yy} = \frac{a_o - a_s}{a_o} = \varepsilon \quad , \qquad (1.13)$$

where a_o and a_s are native and strained lattice constants, respectively. V_h and V_s are deformation potentials of hydrostatic and shear strain, respectively. With the definitions of H and S:

$$H = V_h(\varepsilon_{xx} + \varepsilon_{yy} + \varepsilon_{zz}) \quad , \qquad (1.14)$$

$$S = V_s(\tfrac{1}{2}(\varepsilon_{xx} + \varepsilon_y y) - \varepsilon_{zz}) \quad , \qquad (1.15)$$

Using results from biaxial strain above, we obtain:

$$H = (-V_h).2\frac{C_{11} - C_{12}}{C_{11}}\varepsilon \ , \quad , \qquad (1.16)$$

$$S = (-V_s)\frac{C_{11} + 2C_{12}}{C_{11}}\varepsilon \ . \quad , \qquad (1.17)$$

The sign of the strain ε determines the sign of both H and S because V_h , $V_s < 0$ in common semiconductors. Considering δ is the additional repulsion between the light-hole and the split-off bands ($\delta \approx 2S^2/E_{so}$), the bandgap shifts can be computed:

$$\Delta E_{hh} = H - S \ , \quad , \qquad (1.18)$$

$$\Delta E_{lh} = H + S - \delta \ , \quad , \qquad (1.19)$$

$$\Delta E_{so} = H - S + \delta \ , \quad , \qquad (1.20)$$

In the cases of existence of shear stress, shear component of the elastic stiffness component and additional deformation potentials V_{sh} related to shear stress are included in the calculation. The parameters for the strain calculation of some important III-V semiconductors are provided by Adachi [45,46] and Landolt-Börnstein [47].

To predict the band structure away from band edge, the strain Hamiltonian must be added to the L-K Hamiltonian and the combination must be diagonalized. The total split energy between the heavy hole and light hole bands is defined as S_{sp}. Using (1.18) and (1.19) we obtain:

$$S_{sp} = E_{lh} - E_{hh} = 2S - \delta \approx 2S\,(1 - S/E_{so}) \quad , \qquad (1.21)$$

where the latter approximation expands δ to the second order in S (with the assumption $S << E_{so}$). The calculations that consider both cases (with and without split-off band coupling) have been done by Chuang [48]. This calculation partly includes the split-off band coupling. Therefore, it improves the accuracy of the subband structure calculation compare to the case in which we ignore this coupling in the L-K Hamiltonian.

In semiconductor QWs, for the description of the modification of electronic band structure in presence of strain, Smith and Mailhiot used the k.p formalism to develop a complete theory that is appropriate for theoretical calculations of induced strain effects [49]. In this theory, averaged pseudo-potential form factors for constituent materials are used. The calculations provide a basis set for the zone-center Bloch states. The combination of the Löwdin perturbation theory [50] and the k.p operator allows the calculation of all relevant bands (conduction, heavy-hole, light-hole and split-off). The perturbation theory is done to first order for wave functions and to second order for energies. The spin-orbit interaction and stress interaction, due to possible lattice mismatch, are taken between the explicitly included states. This general approach also calculates the bulk-material eigen-functions for use in subsequent calculations, and allows for full band mixing among the four explicitly-treated bulk bands [51]. The band mixing arises due to such effects as quantum confinement and strains. The theoretical formalism properly accounts for symmetry considerations and bulk-material-specific characteristics throughout the QW band structure calculation. QW states are found via an eigen-value equation that is derived from the matching of the individual bulk-material states at the material interfaces using the normal component of the current density operator [52,53]. The details of the formal results of this theory as well as numerical solutions for applications are given in [49,54,55]. Based on this theory, we are able to model the modification of the QW band structures due to an induced strain with an assumption of negligible spin-depended strain interaction. Similar to the treatment used for bulk structure, the modelling of QW band structure also employs the strain Hamiltonian that is based on deformation potential constants. These constants for III-V semiconductor materials can be obtained from Refs. [45-47] and the more recent Ref.[56]. The formalism can applied for stresses along different directions and an arbitrary strain configuration.

The electronic band structures of GaInAs/AlInAs structures growing in different crystal directions were studied in Refs.[54,55] and the results are typical examples for the modification of band structures in QWs under stress calculated by Smith and Mailhiot theory. One of these results is presented in Fig. 1.10 for $Ga_{0.47}In_{0.53}As/Al_{0.33}In_{0.67}As$ (tensile strain) and $Ga_{0.47}In_{0.53}As/Al_{0.63}In_{0.37}As$ (compressive strain) for structures grown along the [100] crystallographic axis. This result shows the shifts of the lh and hh bands to take place into different directions.

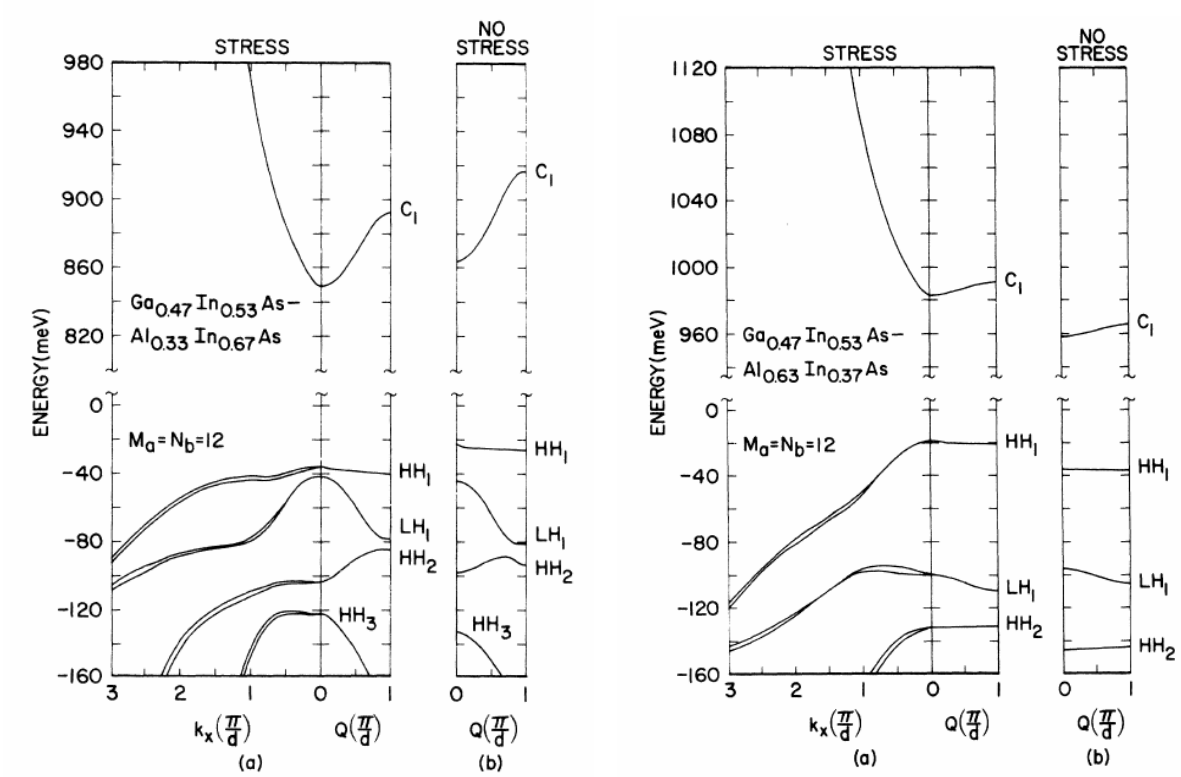

Tensile strain *Compressive strain*

Figure 1.10: Electronic band structures calculated for GaInAs/AlInAs structures with 1% lattice-mismatched tensile (left-side panel) and compressive (right-side panel) strain; in each panel (a) and (b) graph are calculation results either included and excluded strain effect, respectively [54].

1.2.3. Theoretical calculation for a relation between spectral shift of optical transitions and strain in quantum-well structures and devices

In the previous section, we already introduced the theoretical background for electronic band structure calculations of semiconductor QWs. This formalism allows describing QW band structures as a function of externally induced strain. The band structure relates directly to interband transitions in semiconductor QWs. Therefore, a spectroscopic method that based on optical interband transitions can be applied for strain analysis of QW structures and devices. However, such method requires complete numerical results, which can interpret strain from optical spectra, and vice versa. In this section, we present the results of a theoretical calculation of coefficients for the change in interband transition energy as a function of induced strain and predictions about strain behaviors for QW structures and devices.

Strain analysis by spectroscopic means mostly uses the two lowest energy interband transitions in QWs, namely hh1-e1 and lh1-e1 transitions. The shifts in the hh1-1e and lh1-e1 transition energy with strain as discussed in previous section are

strongly correlated. By analyzing these transitions in the optical spectra, we can obtain strain information in semiconductor QW structures and devices.

There are two additional effects, which must be considered before proceeding with the calculation of results, namely the change of the exciton binding energy with strain and the quantum–confined Stark effect (QCSE) [57]. These effects definitely contribute to the net change of the interband transition energies with an externally induced strain. However, both of them are relatively weak for small strains in calculations for the range of well widths from 4 - 12 nm, which are typically used in devices [58]. In Ref. [59], it has been shown that for the hh1-e1 transition, the exciton binding energy shifts by less than 1 meV for an applied stress along the <110> direction of up to 16 kbar that leads to in-plane hydrostatic strain components of about 1.9 % [52]. This value is more than one order higher than typical value of externally induced strain arising in the semiconductor QW structures under investigation, e.g. HPDL bars. Therefore, the shift of hh1-e1 transition due to the change in exciton binding energy is negligible. The exciton associated with the lh1-e1 transition is much more sensitive to an induced strain [59]. However, the lh1-e1, exciton binding energy shifts by only about 1 meV when hydrostatic strain components change from zero to about 0.25 % [52]. That also is much higher than the value we observed in our devices in practice. For QCSE, a magnitude of 0.30 % packaging-induced strain component causes a shift due to the QCSE of less than 1 meV [52]. This value of the externally induced strain is still three times the typical value frequently observed in our devices (0.1%). With these evidence, we can conclude that under externally induced strain shifts of interband transition energies due to change in exciton binding energy and QCSE are negligible (far below 1 meV) and are usually not considered.

In strain analysis, we are mostly interested in strain configurations specific for QW devices. Here, we choose the case of uniaxial stress along the <110> direction, because it serves as a model for packaging-induced strain in HPDL bars. Let us describe briefly the uniaxial packaging-induced strain model that is applied for a particular device, namely a “cm-bar”. This model includes four strain components existing in the QW structure. Three of these components are hydrostatic in nature, ε_{xx}, ε_{yy}, and ε_{zz}. The fourth

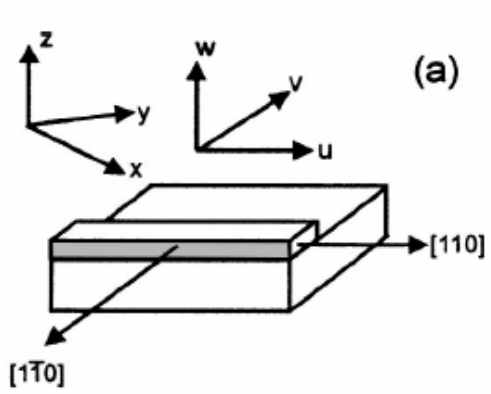

Figure 1.11: Schematic diagram of the “cm-bar” architecture. The x-y-z is crystal coordinate system and device-specific u-v-w-coordinate system is rotated by 45^0 within the QW plane.

strain component is a shear strain, ε_{xy}, which lies in the plane of the QW. The shift of the interband transition energy with the packaging-induced strain is reported in terms of the induced strain along the long axis u of the "cm bar" (see Figure 1.11). The coordinates used for the descriptions of a laser bar usually is denoted as *u*-*v*-*w*.

Fig. 1.12 shows results for the shift in the interband transition energy as a function of packaging-induced strain along the <110> direction. These results are calculated for an $In_{0.06}Ga_{0.86}Al_{0.08}As/Ga_{0.7}Al_{0.3}As$ QW with a well width of 8.0 nm in the case of zero intrinsic strain. We should emphasize two important aspects extracted from Fig. 1.12. The first one is the difference in the responses of heavy-hole and light-hole shifts with the strain. This feature is essential for distinguishing the interband transitions in optical spectra, especially in tensile intrinsically strained QW structures, which have heavy-hole and light-hole subbands very close together. It may even happen that the lh1 subband may lie energetically above the hh1 subband [60].

The second aspect, which is highlighted in Fig. 1.12, is the linear relation between the transition energy shifts and strain. This relation applies for both compressive and tensile packaging-induced strain. However, the slopes are clearly different for compressive packaging-induced strain but not too much for tensile strain. With this linear relation, we can determine the energy shifts as a function of strain by using these slopes. Thus we use the slopes as coefficients for strain analysis. The behavior of the subband energy shifting with packaging-induced strain was analyzed for a wide range of well widths [58] and a wide range of intrinsic strains. However, as soon as the packaging-induced strain increases above about 0.20 % than nonlinearity in the transition energy shift with strain becomes increasingly significant. Therefore, the use of a linear fit and a single slope becomes less appropriate [52] and the above

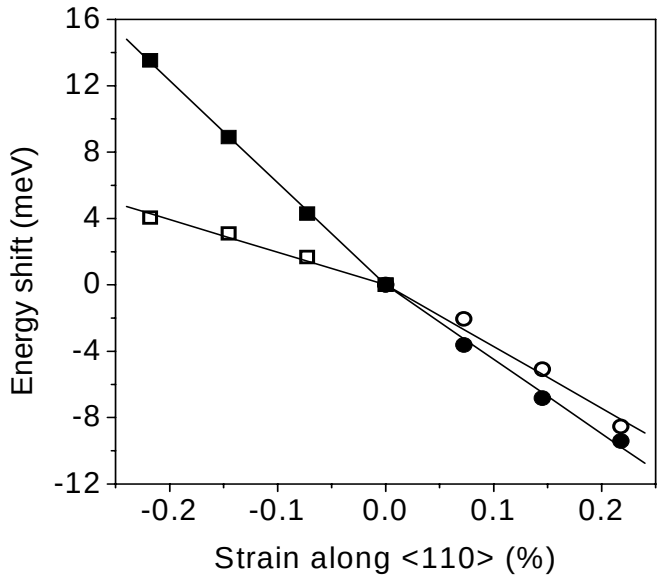

Figure 1.12:

Transition energy shifts as a function of packaging induced strain along the <110>-direction for the case of zero intrinsic strain. The hh1-e1 transition, compression, open squares; lh1-e1 transition, compression, solid square; hh1-e1 transition, tension, open circles; lh1-e1 transition, tension, solid circles [52].

discussed concept of the use of the coefficients fails.

The theoretical calculation was performed for different situations of intrinsic strains that are of biaxial symmetry in the plane of the QW. The results show that the change in transition energy with strain is still linear even for intrinsic strain magnitudes of up to at least ±0.45 % [52]. The explanation for this is the nonlinearity in the change in transition energy with strain caused by band mixing that result from the presence of shear strain components or anisotropic in-plane strains [60-64].

Now, we address the energy-shift-per-strain coefficients calculated for various QW parameters (e.g. well width and intrinsic strain are altered). These coefficients for a particular intrinsic strain and well width QW are important for applications. Firstly, for the well width dependence, the results in the Ref. [58] show a negligible influence of various well widths ranging from 4 nm to 12 nm on the coefficients. Thus, the coefficients determined for a well width of about 8.0 nm can be also used for QWs with a range of well widths 4 – 12 nm, which are often used in QW devices. Secondly, for the intrinsic strain dependence, the coefficients were calculated in strain configurations with $\varepsilon_{uu} = \varepsilon_{vv}$ ranging from -0.45 % (compressive strain) to +0.45 % (tensile strain).

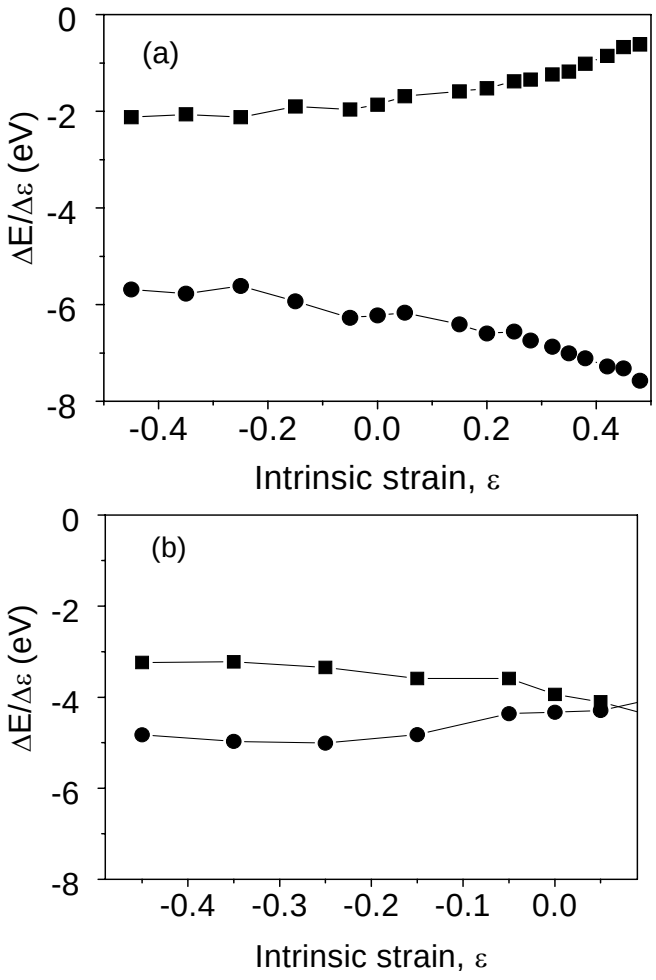

Figure 1.13:

Strain sensitivity for QW interband transitions as a function of packaging-induced strain. The sensitivity are defined as the shift in energy per packaging-induced strain along <110> direction, or u axis. (a) and (b) are the sensitivities for compressive and tensile, packaging-induced strain, respectively with hh1-e1 transition, squares; lh1-e1 transition, circles [52].

Fig. 1.13 shows the energy shift coefficients as a function of intrinsic strain. These results were calculated for an $In_{0.06}Ga_{0.86}Al_{0.08}As$/ $Ga_{0.7}Al_{0.3}As$ QW with a well width of 8.0 nm. The hh1-e1 and lh1-e1 transition coefficients for the cases of compressive and tensile packaging-induced strain are displayed in Fig. 1.13 (a) and (b), respectively. For compressive intrinsic strain, i.e., negative strain values in Fig 1.13 (a) and (b), the coefficient associated with the lh1-e1 transition is always larger in magnitude than the hh1-e1 transition coefficient. Although the change of compressive intrinsic strain is not particularly large, it still causes a variation of the energy shift coefficients. For tensile intrinsic strain, the coefficients change more rapidly for both the hh1 and the lh1 transitions in the case of combination between compressive packaging-induced strain and tensile intrinsic strain. This behavior becomes more complicated when both, the intrinsic strain and the packaging-induced strain are tensile; the coefficients change abruptly, and even change their sequence in some cases. This behavior is a direct consequence of the shifts in valence subband energies under the influence of tensile strains [60,65,66]. According to Ref. [52], this complicated behavior, depends on the well width and the specific materials being used in the well and barrier.

Table 1.3 summarizes the theoretical results. The calculated coefficients, which can also be denoted by the alternative term “strain sensitivity”, account for the change in interband transition energy as a function of induced strain ($\Delta E/\Delta\varepsilon$) for different situations (e.g. change of intrinsic strains), which are relevant for the analysis of our experimental results in the upcoming chapters. All QW results were calculated for the structure identical to the one that was used for calculation of the results shown in Fig. 1.13. The calculated coefficients cover the cases of bulk and QW including the presence of intrinsic strains when externally uniaxial, biaxial and hydrostatic stresses are applied.

Table 1.3: Relation between spectral shift of optical transitions and train [52]

a. Applied stress along [110], with biaxially-symmetric, in-plane, intrinsic strain (eV)

	Bulk $Al_{0.3}Ga_{0.7}As$ 0.0 intrinsic	QW 0.0 intrinsic	Bulk $Al_{0.3}Ga_{0.7}As$ -0.45 % intrinsic	QW -0.45 % intrinsic	Bulk $Al_{0.3}Ga_{0.7}As$ 0.45 % intrinsic	QW 0.45 % intrinsic
Compressive *hh1-e1*	-1.18	-1.86	-2.05	-2.12	-3.52	-0.672
Compressive *lh1-el*	-7.29	-6.22	-6.22	-5.69	-5.13	-7.32
Tensile *hh1-e1*	-1.42	-3.94	-3.85	-3.24	-2.43	-1.56
Tensile *lh1-e1*	-7.29	-4.33	-4.65	-4.83	-6.47	-6.88

b. Biaxial applied strain, with biaxially-symmetric, in-plane, intrinsic strain (eV)

	Bulk $Al_{0.3}Ga_{0.7}As$ 0.0 intrinsic	Bulk $Al_{0.3}Ga_{0.7}As$ -0.46 % intrinsic	Bulk $In_{0.06}Ga_{0.86}Al_{0.08}As$ -0.46 % intrinsic	QW -0.46 % intrinsic
Compressive or Tensile *hh1-e1*	-11.7	-11.7	-11.4	-10.3
Compressive or Tensile *lh1-e1*	-16.1	-16.0	-15.5	-14.1

c. Hydrostatic applied strain, with biaxially-symmetric, in-plane, intrinsic strain (eV)

	Bulk GaAs 0.0 intrinsic	Bulk $Al_{0.3}Ga_{0.7}As$ 0.0 intrinsic	Bulk $In_{0.06}Ga_{0.86}Al_{0.08}As$ -0.46 % intrinsic	QW -0.46 % intrinsic
Compressive or Tensile *hh1-e1*	-24.69	-24.69	-24.18	-23.84
Compressive or Tensile *lh1-e1*	-24.69	-24.69	-24.18	-23.69

Now, we discuss an important trend that is discovered by considering the coefficients in Table 1.3. We confine the discussion to situations of compressive intrinsic strain and compressive in-plane applied strains. If we take the ratio of the hh1- and lh1-related $\Delta E/\Delta\varepsilon$ coefficients for various applied strain conditions, for the cases of a uniaxial stress applied along the 110-direction, a biaxially-symmetric in-plane applied strain, and a hydrostatic applied strain, we obtain respective values of 0.16 to 0.37, ~0.73, and ~1. These values indicate a tendency. If the applied strain becomes more symmetric; the changes in the hh1- and lh1-related transitions as a function of applied strain become increasingly similar, as shown in Fig. 1.14. This is consistent with the behavior of the zone-center states under the various applied strains [52].

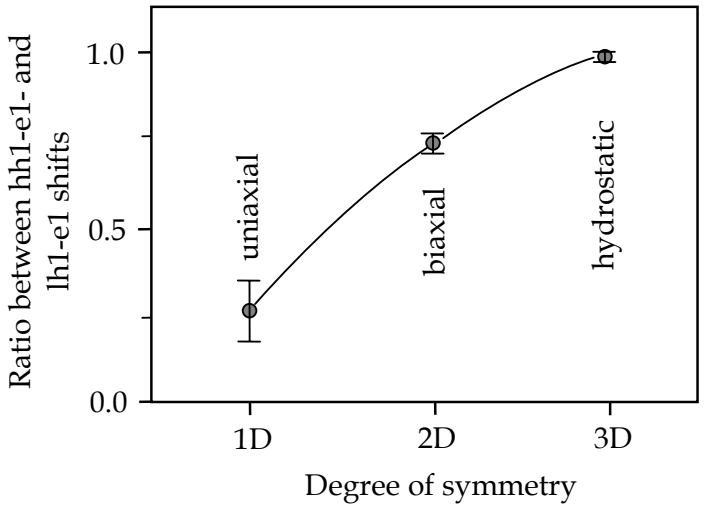

Figure 1.14: The relationship of the ratio between hh1-e1 and lh1-e1 shifts and strain symmetry

This tendency provides a useful tool to estimate the strain configuration in the case of compressive strain. If the shifts of both the hh1- and lh1-related transitions

with strain are measurable, we can determine the ratio of these shifts. Therefore, we can get rough information about symmetry of strain configuration in the investigated structure. A value of the ratio close to 1 implies a highly symmetric strain configuration. A small value for the ratio implies a low-symmetry strain configuration, possibly including a shear strain contribution

A similar trend is not observed for cases of tensile in-plane strain. The explanations may be given that tensile strains (in-plane) can lead to strong mixing of the hh1 and lh1 subbands, which leads to a more complicated behaviour of the hh- and lh-related interband transitions.

The method described here for the analysis of strain can be widely applied to QW devices and structures with a wide range of well widths and intrinsic strains. Using these numerical results and combining with spectroscopic means, we now able to do strain analysis of semiconductor QW structure and devices. The theoretical model already had been compared to experiment results and showed agreement with experiment [52]. Therefore, in the next chapters, we will use these results to discuss about strain behavior in HPDLs.

Chapter 2.

Experiment

2.1. Spectroscopic methodology for studies of semiconductors optoelectronic devices

2.1.1. Overview about the optical techniques used

A detailed analysis of the properties of semiconductor optoelectronic devices is important and representative methods are, e.g. X-ray diffraction, Raman scattering spectroscopy, luminescence, and absorption-related methods.

The X-ray diffraction technique accesses directly information about atomic distances in the crystal lattice. This is useful to investigate strain and temperature distributions in the devices [67,68]. The Raman scattering spectroscopy is also known to be useful for optoelectronic device studies [69-71]. The principle of this method is based on analysis of modification of quantized atomic vibrations (phonons). Thus it provides results about quality and temperature of crystal lattice, strain, carrier concentration, etc. [72]. Other optical techniques, which are also frequently used for the investigation of semiconductor optoelectronic devices, especially for HPDLs, are electroluminescence (EL), CL, thermography, PL and PCS. This section introduces briefly these techniques, which will be applied in the experimental sections.

The EL technique is based on emission from semiconductor devices under current. Therefore, this method is useful only for studies of electric-optical conversion devices, e.g. light-emitting diodes (LEDs) or diode lasers. EL topography (or microscopy) can be obtained from the active region of devices. The resolution is determined by using appropriate optical microscope objectives. Typically, a micrometer scale can be resolved. The EL microscopy technique shows the spatial distribution of emission intensity. It allows for the observation of the generation and

growth of defects in the active region [11,73]. One derivative of the EL method, namely EL spectroscopy (spectrally resolved), provides analysis of defects in optoelectronic devices [74]. Especially, this technique is useful for studies of HPDLs. Results about defects and strain in HPDL structures, which are related closely to reliability and lifetime, have been reported [75,76] and continuously further developed for study of novel structures of HPDLs [77].

The CL signal results from excitation by electrons with keV energy [78,79]. In this method, we get, e.g., panchromatic CL images or CL spectra. The panchromatic CL images are detected from reflected or transmitted CL radiation [80]. These images show the status of a semiconductor structure, especially the defects that are located at the surface or in the volume of device [78,79,81]. The luminescence emitted from the device is spectrally resolved by a monochromator and imaged on to a CCD camera providing a CL spectrum. The CL spectra allow for the spectroscopic analysis of device. Additionally, complementary temperature dependence and time-resolved CL measurements are possible. The spatial resolution of CL is on the order of few hundred nanometers [79]. The CL technique has been applied efficiently in studies of many kinds of semiconductor optoelectronic devices among them also HPDLs [81,82]. But the required sample preparation, if inner parts of devices should be accessed, is a time consuming process.

The application of thermograpy to optoelectronic devices is based on multi-spectral imaging system that operate in two optical channels, the near infrared at 1.5-2 μm and the mid infrared at 2.4-5.5 μm. Experimental setup of this technique only requires a thermo camera with macro- and microscopic objective that lead to different spatial resolutions (e.g. 25 and 5 μm, respectively) [83,84]. During the measurement, alternative filters have been used to block unexpected emission from sample coming from the device to the thermo camera. Imaging thermography is a powerful tool for reliability screening of HPDLs, especially, temperature profiling and defect recognition [83-85].

PL is one of the most important optical methods for analysis of semiconductor materials and devices. PL is mostly excited by lasers with photon energies above the bandgap of the material. The luminescence radiated from the semiconductor sample can provide information on optical transitions or crystal symmetry. This information allows for analysis of properties of semiconductor devices, e.g. homogeneity, strain, defects, etc [86-88]. In this thesis, we will use two approaches of the PL technique: micro-PL that includes spectral resolved and polarized PL. The PL setup can perform spatially resolved measurements for both micro- and polarized-PL techniques.

Now, we consider an absorption related method, namely PCS. In this technique, which is based on the photoelectric properties of semiconductor device under investigation, samples are used as photodetector to convert excitation light and then

generate the PC signal. The PC intensity versus excitation photon energy indicates various optical properties of devices. The PC setup allows measurements of PC spectra with spectral as well as spatial resolution. We can perform single spectra measurements only, or scan spectra versus local position. The PC data provide information directly for analysis of absorption properties, which are related to strain and defects in optoelectronic device structures. These characteristics strongly influence the reliability of devices. In this thesis, PCS and related techniques (LBIC and NOBIC) have been used as essential method in all of investigation of optoelectronic devices.

2.1.2. Experimental setup for photocurrent measurements

PCS has been introduced in the previous chapter. In this section, we will present the experimental approaches for measurements of PC spectra. Both, the conventional technique as well as the advanced technique (Fourier-Transform spectroscopy) for PC measurements are described in detail. Due to advantage of being a non-destructive technique, in this thesis the PCS has been applied to all investigated semiconductor structures.

A conventional PC measurement setup includes three main parts, namely excitation, spectral resolution, and detection. The excitation source for a PC setup is white-light lamp that provides broadband of excitation spectrum. The light beam goes through a grating monochromator that provides dispersion of light. At the exit slit of the monochromator, the output beam is modulated and focused by a chopper before it illuminates the surfaces of the sample. The PC signal is detected by a lock-in amplifier. For example, a conventional setup with halogen lamp and SPEX 1681 monochromator and SR830 DSP lock-in amplifier provides spectral resolution of 0.5 - 2 nm (in the wavelength range from 600 -1100 nm) . For polarized PC measurements, a polarizer can be inserted into the light beam in front of the sample. In the sample holder, a Peltier cooler is implemented for temperature stabilization. This is required because PC spectra are temperature depended. The conventional PC setup as described here can provide single PC spectra for many types of semiconductor samples. Another condition of the application of this technique is the necessity to have contacts at the sample enable measuring the light induced-current.

A conventional PC setup shows some disadvantages. Thus, we introduce an alternative technique, namely Fourier transform (FT) PCS, which is considered an advanced measurement method for obtaining PC spectra. The setup with a PC Fourier transform spectrometer is shown in Figure 2.1. The main part of this setup is based on a BRUKER IFS66v FT spectrometer. White light generated from a halogen lamp (150 W) is modulated by a Michelson interferometer generating an interferogram (an

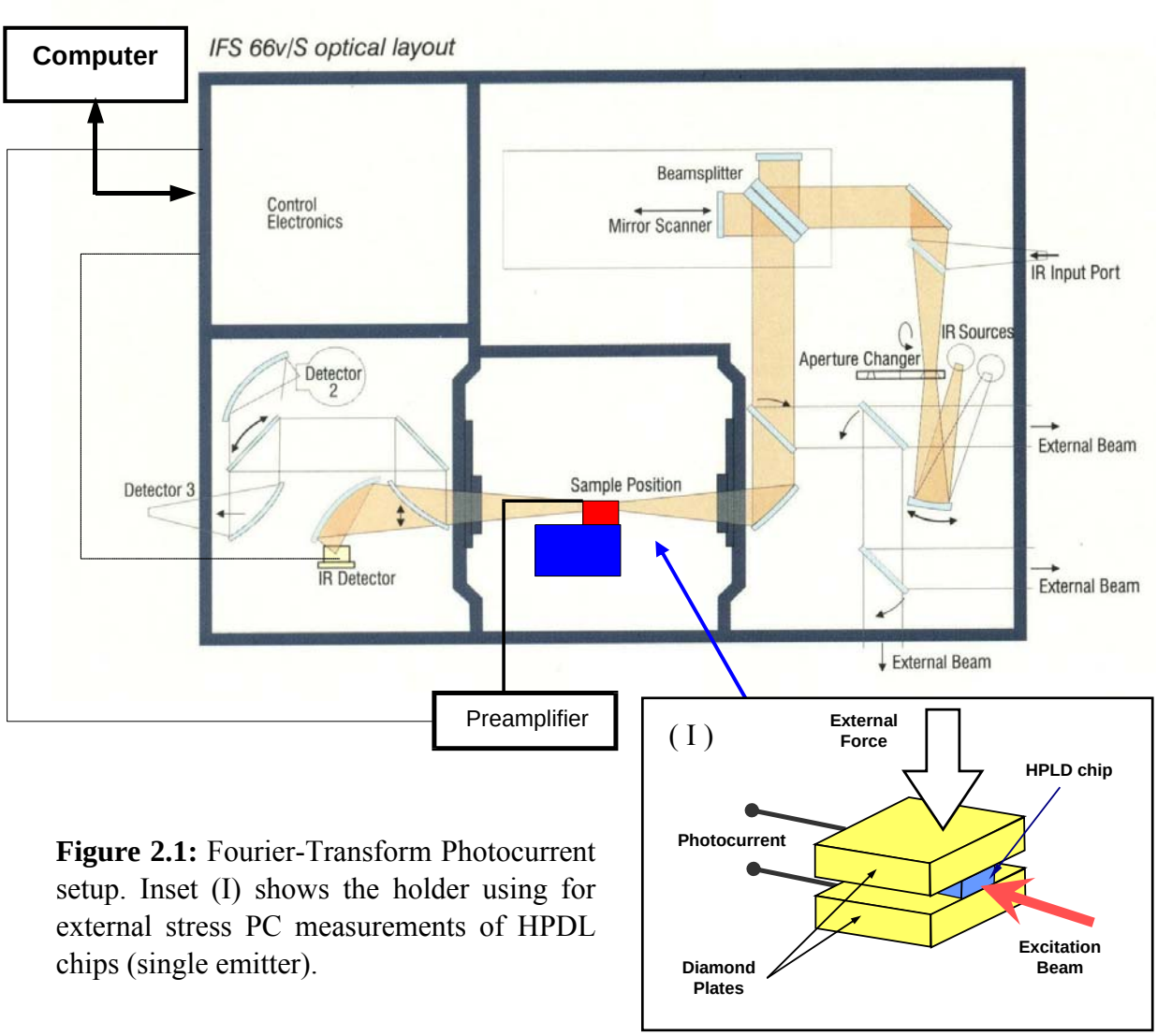

Figure 2.1: Fourier-Transform Photocurrent setup. Inset (I) shows the holder using for external stress PC measurements of HPDL chips (single emitter).

"interference image"). The in this way modulated light irradiates the sample surface and induces a photoelectric signal (current). This current is amplified by a high sensitivity low noise current pre-amplifier (Stanford Research SR 570) before fed into the electronic unit of the FT spectrometer. Afterwards, the electronic unit and software perform a Fourier transform routine on the interferogram to obtain the PC spectrum. The maximum resolution of the FT spectrometer is about 0.01 nm (at a wavelength of 800 nm). The spectral range of the spectrometer being equipped with halogen lamp and CaF_2 beam splitter expands from visible to mid-infrared (10 μm). However, this range might be reduced if we use optics (lens or microscope objective) that absorbs the light within this range. As in the conventional setup, a temperature controller is installed in sample compartment of FT spectrometer as well.

The comparison between conventional PC and FT PCS techniques mainly bases on the achievable signal to noise ratio (SNR) of the PC spectra. In PC spectra, a higher SNR value leads to a better quality of the spectrum. If noise is random, the SNR value increases proportionally to the square root of the number of scans [89]. Fig. 2.2 illustrates this correlation. In this Fig., three lines represent different improvements of

SNR of three samples versus the number of scans. The dashed line, dotted line, and the solid line correspond to different raw SNR ratios that are determined from the PC spectrum after a complete scan. These data are picked up from typical values that we measured with FT spectrometer. There are two advantages of FT-spectroscopy that usually are mentioned: throughput and multiplex, when we compare FT and conventional grating spectrometers. The conventional PC setup suffers from a significant reduction of incoming intensity after the excitation beam goes through monochromator. On the other hand, the FT spectrometer can offer a much higher energy-gathering capability. As we know, the SNR of the spectrum increases proportionally with throughput [89]. Therefore, FT PC setup can provide significantly better raw SNR. In case of the multiplex advantage, a monochromator records a small spectral band at a time, whereas FT spectrometer allows recording of interferogram that contains all spectral bands. This advantage also provides an improvement of the SNR value. Practically, the conventional setup requires longer scan time to achieve the same SNR as an FT PC setup. Furthermore, the SNR will be improved if we accept a lower spectral resolution. This is used in the conventional PC setups. In the FT PC setup presented here, with resolution of 0.5 nm (at 800 nm), typically, the SNR is on the order of 10^3 - 10^5 connected with measuring times from 10 s to 24 hours.

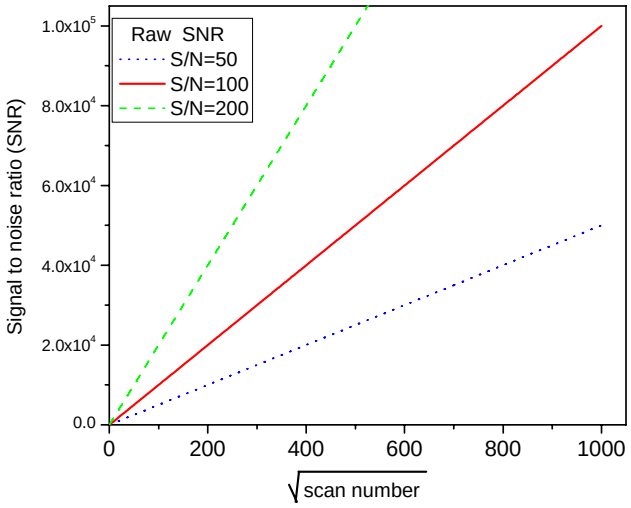

Figure 2.2: SNR versus scan number of FTIR PC setup

There are several ways to use the FT spectrometer for PC measurements. The first option is similar to conventional monochromator-based option. A single PC spectrum is collected for samples, from which we need only the absorption structure of material layers or defect levels. In the second option, PC spectra are performed at different local position of sample by scanning procedures. Therefore this option is called PC scan. In the PC scan measurements, a translation stage is installed in the sample compartment. Investigated samples that are mounted on the stage can be moved horizontally with a step width of ~26 µm. To improve the spatial resolution of PC scan, we employ a microscope objective to reduce the light spot size to a diameter of 30 µm. Thus, combining spot size and translation step allow PC scan measurement

with a spatial resolution of 30 µm. The measurements performed at this spatial resolution will be called µPCS.

The FT PC setup is very flexible. We can reconstruct the sample holder for different kinds of HPDLs and/or alternative experiments. Now, we introduce a particular sample holder construction for PC measurements of HPDL chips under external artificial stresses (see inset in Fig. 2.1). The holder is constructed in a three-dimension translation stage. Two diamond plates were mounted on this stage with the top plate freely movable in the vertical axis. The HPDL chip is clamped in between the two plates. Gold layers that cover the diamond plates provide a good electrical contact for PC measurements. External stresses are applied on the top plate by weight blocks. This construction allows measurements of PC spectra versus external stresses.

PC measurements of HPDLs as well as other optoelectronic devices are done for almost all studies related to strain and defects. To achieve a sufficient result with the PCS technique in a particular experiment, we have to choose an appropriate apparatus parameter set, which represents the optimum balance of requirements (spectrum quality, measuring time and spatial resolution).

2.1.3. Laser-beam-induced-current technique

This section will describe PC-related techniques, namely LBIC and its extension with higher spatial resolution NOBIC. These techniques can be considered as PC measurements with white light excitation being substituted by monochromatic (laser) light.

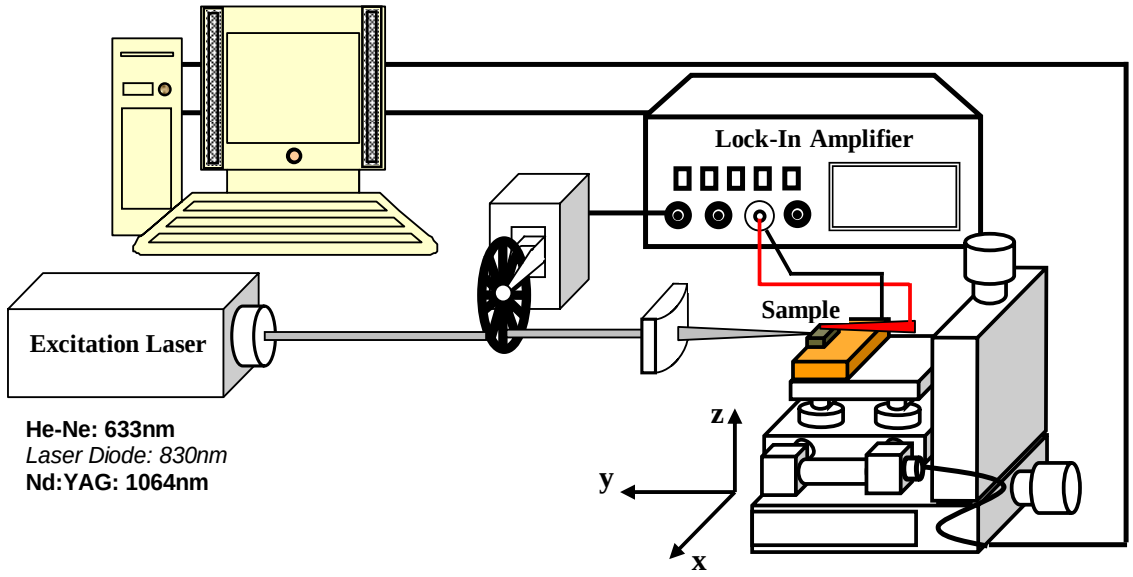

Figure 2.3: LBIC measurement setup

LBIC is a well-known technique for analysis of semiconductor structures and devices containing potential gradients. The experimental setup of LBIC technique is shown in Fig. 2.3. It has three main parts: excitation beam, sample scanning stage and signal processing equipment. Excitation beam of LBIC measurements employs a laser source for illuminating the sample surface to generate a PC signal. If the excitation laser is used for efficient creation of non-equilibrium carrier pairs, its wavelength must be chosen above the energy gap of the structure that will be investigated [34l]. Our LBIC system supports several excitation laser wavelengths from visible (He-Ne: 633 nm, Diode laser 730 nm) to the near infrared (Diode laser: 830nm, Nd:YAG: 1064 nm) region. Therefore, this setup allows studying different optoelectronic devices operating at visible and infrared region. The laser beam is focused by a cylindrical lens before being irradiated onto the surface of a sample. The second part of the setup includes the sample holder on a three-dimension-translation stage. This stage is controlled by a computer and provides possibilities of line or two-dimensional scans with sub-micron steps. The sample holder is mounted onto a Peltier cooler that allows temperature stabilization to ensure reproducibility of given measurement conditions. Detection is done by a lock-in amplifier (NF 5610B). To use the lock-in technique, the laser beam must be modulated by the chopper with frequencies typically in the range of 1-3 kHz. The modulated laser-induced PC signal from the sample is amplified before transferred to the computer for data analysis. Since the LBIC setup uses laser sources, this allows reducing of focused beam size until the diffraction limit. Thus the spatial resolution of whole system can achieve the value of about 1 μm. LBIC measurements show the intensity distribution of the PC signal amplitude versus local position at the sample surface in the forms of line or maps depending on analysis requirements of the sample. The LBIC method does not provide any spectral information. We can find the advantage of the technique in the aspects of high spatial resolution and less time consumption compare to PC measurements. There are some standard applications of LBIC. First, we can use LBIC to recognize the lateral structure of HPDLs. This measurement is quick and provides useful information for possible next steps of the investigation. The second way, LBIC can be a used is to be a tool to analyse defects located in HPDLs. This application can be accomplished when we use an excitation laser wavelength for LBIC scanning longer than emission wavelength of HPDLs. The distribution of defects as well as its concentration can be located and estimated.

Now, we introduce NOBIC, another option of PC-related methods. The NOBIC technique, which uses the emission mode of a Near-field Scanning Optical Microscope, might be considered as an extension of LBIC with a better spatial resolution [90]. In the NOBIC experiments, the sample surface is excited by evanescent light transmitted through a 150 nm-size aperture at end of near-field scanning optical microscope probe tip. Excitation sources for our NOBIC experiments

are tunable continuous-wave laser sources (Ti: sapphire 730 nm) or a He-Ne laser (633 nm). A Y-coupler was employed for feeding light from these laser sources into the fiber tip. This solution allows to carefully control the amount of light coupled into the fiber tip (error less than 5%) [91]. The photo-induced current generated from sample is detected as a function of the tip position. The probe tip is made from a tapered single mode optical fiber with a tip diameter of 150 nm. The sample, which is mounted on an x-y-z piezo, is scanned relative to the probe tip. During the scanning measurement, the tip-to-sample distance was kept constant at 5 ± 1 nm. Similar to LBIC, NOBIC measurements can also provide a line scan as well as a map. Scanning area in the surface of sample is typically 10x10 μm^2 and the spatial resolution is ~ 150 nm [92]. An example of the use of this high resolution is the investigation of the defect characteristics of QW structures in HPDLs being discussed in the next chapter. Because of the inherent experimental challenge, NOBIC is not a standard method, and therefore NOBIC should be used as an advanced method when we need higher spatial resolution measurement that LBIC can not provide.

2.1.4. Micro-photoluminescence

The µPL technique is a PL measurement performed on the surface of semiconductor devices under test with a spatial resolution on the micrometer scale. The µPL experimental setup includes: excitation laser beam, focusing optics systems, sample scanning stage and detection part (see Fig. 2.4). The excitation lasers that are equipped for µPL system employ He-Ne (633 nm) or also an alternative source, e.g. Argon 514 nm. The laser beam is focused before irradiating the sample surface. The PL radiation from semiconductor material goes through microscope optical system. Finally, a CCD array combined with a spectrometer (Jobin-Yvon) detects the PL signal and provides PL spectra from the sample. PL line scans or mapping images are performed by scanning of excitation beam onto sample surface. This task is done by an x-y translation stage [93]. Typically, the spatial resolution of µPL is on the micrometer scale depending on excitation wavelength and numerical aperture of the microscope optics, i.e. 1 µm is achieved with a 100x microscope objective [77,93]. The measurement is automated

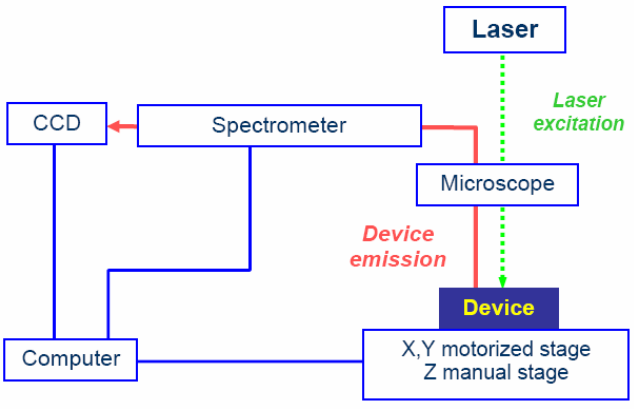

Figure 2.4: Micro-PL setup

and data analysis is done by special software. In typical scans, for each local point, the PL-peak photon energy is plotted. Therefore, the lines scans or two dimensions images provide information on photon energy shifts, which are known as a representation of strain distributions (as discussed in the previous section 1.2.2). For HPDL arrays, in practice, μPL scans can be done in two ways. First the more simple measurement is performed in the substrate at a certain distance parallel to the soldering layer (p-down contact) of the laser, where extraction of strain data is of practical relevance. Second, one can focus the excitation beam to the QW layer and scan horizontally along the array. This measurement provides useful information about the QW. But it is rather difficult to keep the focus within 1 μm and at the position of QW layer when scanning parallel to this layer [94].

2.1.5. Polarized Photoluminescence

Polarized PL is one of the PL-based methods and can be used for the investigation of III-V semiconductor materials [95]. Potentially, polarized PL that belongs to the integrated luminescence techniques may provide very fast measurements [96,97]. Thus it is one efficient way to estimate strain in HPDLs. In this section, we present two methodology approaches: degree of polarization (DOP) of PL and rotating degree of polarization (ROP) of PL.

The experimental setup for both DOP and ROP is shown in Figure 2.1.5 (Ref. [96]). In order to allow for lock-in amplification the excitation laser (He-Ne) is modulated by a chopper before irradiating the sample. The luminescence from the sample is collected through a microscope objective in confocal arrangement and passes through a filter to block all residual He-Ne light. Afterwards, the PL beam comes to a rotating linear polarizer before it arrives at the photo-detector. The samples are scanned by the measurement system under computer control using a translation stage. The spatial resolution of the whole system is approximately 1 μm [95]. Measurement of the DOP or ROP of the luminescence does not require spectral resolution. Typically a sample (i.e., HPDL array) is aligned such that the *x* direction lies in the

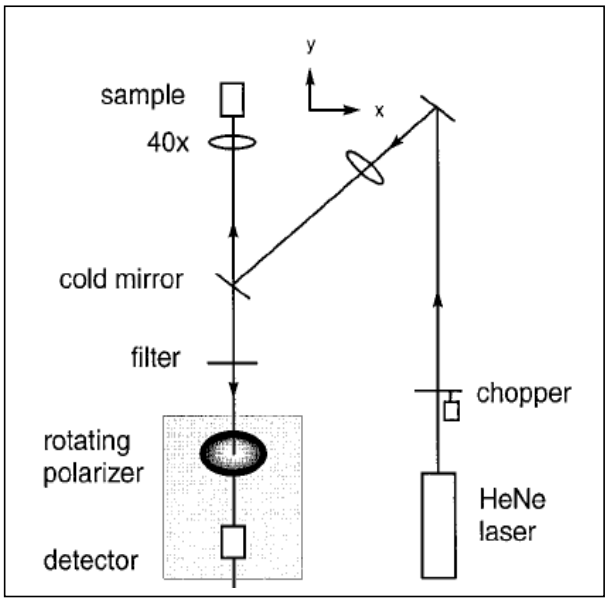

Figure 2.5: Scheme of polarized PL set up [96].

plane of the active region, *z* points into the growth direction, and *y* is normal to the surface being measured, which is a (110)-oriented front facet. This geometry allows for obtaining information on the difference of two normal components of strain (in the DOP configuration) and the shear strain (in the ROP configuration) in a coordinate system that is defined by the plane of the facet [97].

2.2. High power diode lasers investigated by spectroscopic techniques

The HPDLs in our studies include both single emitters and diode laser arrays (bars and stacks). The wavelength ranges from the red to the near infrared region (λ = 650 nm – 1000 nm). They are fabricated on GaAs substrates, and the geometry of the structures is broad-area (BA) or tapered. They are based on SQW or DQW structures and have been grown by Metalorganic Vapor-Phase Epitaxy (MOVPE) technology.

The growing process for all kinds of HPDLs involves the creation of a QW laser structure based on Large Optical Cavity with broadened waveguide layers [98]. The post-growth technology differs substantially from type to type of devices. After MOVPE, the laser wafer is processed by a chain of technology steps: creating a contact window, producing mesa structures, metallization, laser preparation and facet coating. The contact window, which defines the area of the injection current, is made by a metallization process and including implantation or deposition of insulating layers to form this window. Mesa structures are fabricated following the particular requirements of HPDLs structures (e.g. ridge waveguide or optical separating). It determines the "filling factor" (ratio between active area and total width of diode laser) for broad area lasers. A final metallization is performed after that. This process is necessary to make Ohmic contacts (for both side p and n of HPDLs) and to allow soldering on the submount (for heat transfer) and wire bonding. The next step, laser preparation, is done directly on the metallized wafer. This step includes the cleaving process of mirrors to create the laser cavity. The facet coating procedure is the last process within the chain of technology. After initial passivation, HPDLs are coated by thin dielectric

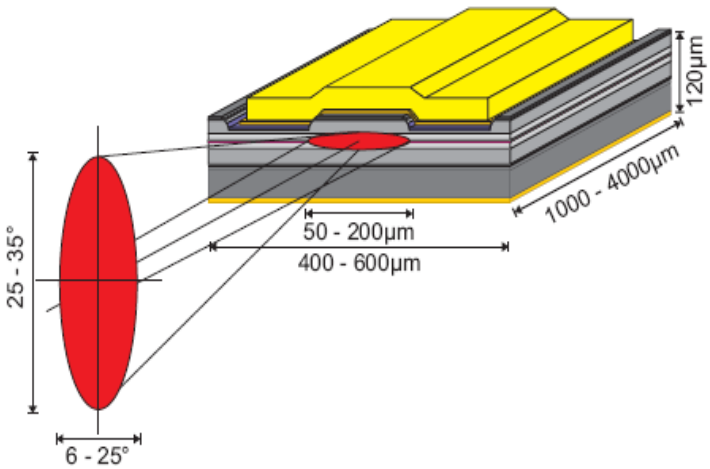

Figure 2.6: Scheme of a single-emitter HPDL [99].

films. Typically, these coated films allow reflectivities above 90% - high reflectivity for rear facet and of 3 - 20% - low reflectivity for front facet.

Figure 2.6 shows a scheme of a complete single HPDL with typical structure parameters. The above described technological processes are applied to most HPDLs. Now, we will describe more details about the particular types that were used as representative devices in the studies of this thesis.

2.2.1. Description of high power diode laser bars

The HPDL bars investigated emit at near infrared region (λ = 808 nm – 980 nm). Depending on the material used for the waveguide structures, we can classify the devices into two groups: AlGaAs-based waveguide structure for wavelengths around 800 nm and Al-free waveguide structure for wavelengths from 940 nm to 980 nm [98].

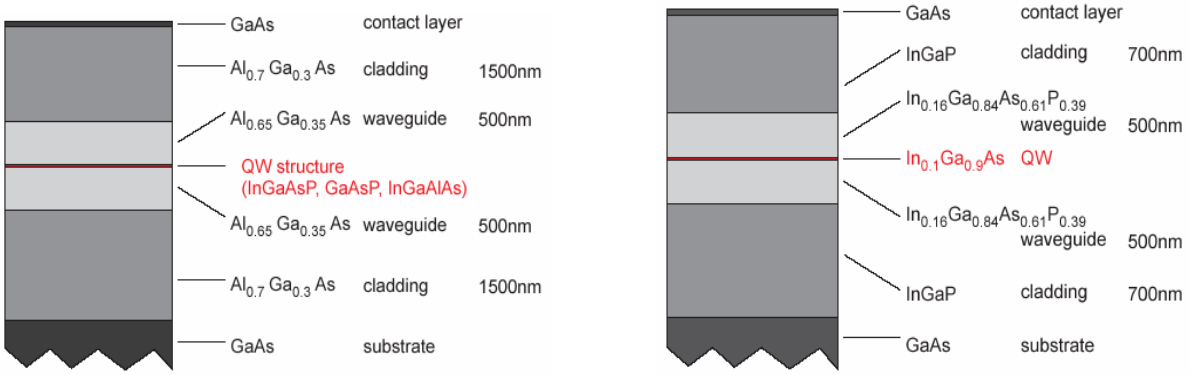

a) AlGaAs waveguide structure b) Al-free waveguide structure

Figure 2.7: Vertical layer sequence of infrared HPDL with LOC waveguide structure [98].

In Fig.2.7a, we show the vertical layer sequence of an AlGaAs-based waveguide structure. Alternative materials for the QW provide different possibilities for the growing process [100]. A double QW structure consists of 7 nm-wide wells and separated by 8 nm $Al_{0.3}Ga_{0.7}As$ barrier with QW composition of $In_{0.06}Ga_{0.86}Al_{0.08}As$ will emit at a wavelength around 808 nm [101]. A typical laser structure for 940 -980 nm wavelengths is shown in Fig. 2.7 b. Al-free epilayers on GaAs are more difficult to grow but they promise some benefits with respect to higher facet stability, reduced generation of defects and higher electrical conductivity.

A high output power from a single chip can be achieved by increasing the stripe width. But the accompanied drawback, an inhomogeneity of optical power distribution along facet will be enhanced substantially. The consequence might be a faster degradation of the diode laser. A practical way to solve the high output power problem is a laser array (bar). A laser bar involves the monolithic integration of many (typically

19 - 65) single emitters. These emitters are optically and electrically separated from each other. Optical separators can be made by etching process as done for mesa-structure as mentioned above. A metallization exclusively on top of the active region

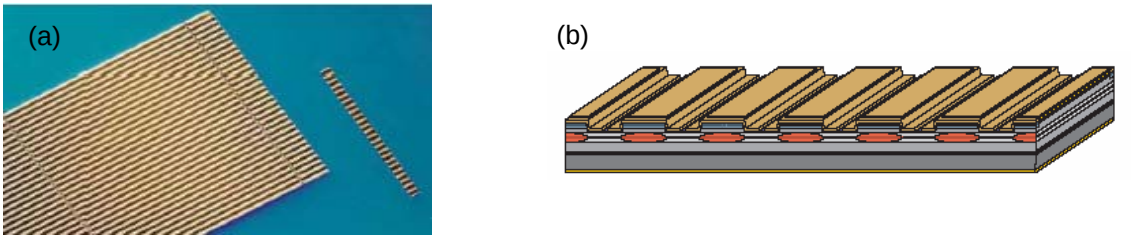

Figure 2.8: HPDL bar: (a) Cleaving of the bar; (b) Geometry of a bar

provides the electrical isolation. Figure 2.8 show the wafer-preparation for HPDL bars and geometric scheme of a part of a HPDL bar. A standard length of HPDL bars of 10 mm has been established. Therefore sometime, we can find the term "cm-bar", which is used to call HPDL bars with such width. The thickness of the bar usually is 110 µm. The emitter width in a regular laser bar is designed with 500, 400 or 150 µm and its typical resonator length is 1000-1500 µm [102]. The fill factor of the bar is in between 30 – 80 %. But a high filling factor requires very good optical isolator to avoid spurious mode [98]. Currently HPDL bars have power conversion efficiencies of more than 70% with output powers of several hundreds Watts [4,5].

2.2.2. High power red-emitting devices

Visible red wavelengths in 630 - 690 nm region are realized with GaInP QWs. Figure 2.9 show the typical structure for red-emitting HPDLs. By using GaInP QWs, a much lower tendency for oxidation than AlGaAs is expected and thus promises a higher stability of the laser facet against Catastrophic Optical Mirror Damage (COMD) [100]. Due to the presence of a lower barrier height for carriers in the QWs (waveguide is AlGaInP), the waveguide thickness must be substantially thinner compared to longer wavelength structures. This solution helps to enhance the confinement factor that reduces threshold density of laser structure [98].

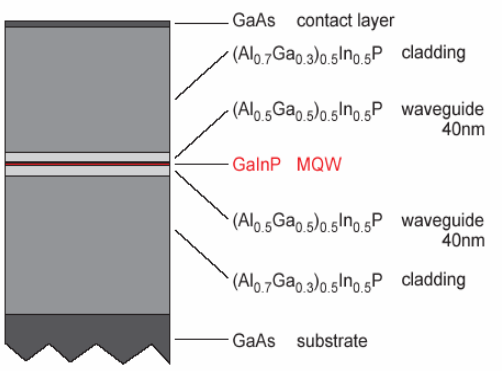

Figure 2.9: Red-emitting epitaxial structure [98].

In this thesis we investigated 650 nm single-emitting HPDL devices based on MOVPE-grown

AlGaInP-structures. One single 5 nm thick InGaP quantum-well is embedded into an AlGaInP-waveguide. The p- and n-side doping are implemented by Mg and Te, respectively. The layer sequence is finished by a 0.4 µm thick highly doped p-GaAs contact layer. From these structures BA single-emitter chips are prepared. The cavity length is 1200 µm, whereas the emitter stripe width is 100 µm. The threshold current is found to be at about 450 mA with a differential efficiency of 0.8 W/A. As a consequence 500 mW are easily reached for operation currents of about 1.1 A.

2.2.3. Novel high brightness tapered diode laser structures

Conventional broad-area HPDLs provide highest output power. However, their main drawback is the loss of a lateral mode confinement that results in rather poor beam quality due to self-focusing and filamentation process. Many different solutions have been proposed to overcome these problems and to achieve high output powers together with a rather good beam quality. Diode lasers with tapered gain sections are one of them. [103-105].

A tapered diode laser consists of a ridge waveguide section and a tapered section. The straight section play an important role in two ways: it provides a single spatial mode and filters out the radiation from the backward travelling reflected field. The tapered amplifier section allows the optical beam to expand gradually in order to lower the optical power density but still conserves the beam quality. The comparatively low and homogenous optical density limits the impact of nonlinear phenomena related to the spatial hole burning effect and reduces COMD of tapered HPDLs [103,105]. Fig. 2.10.a shows an example of a scheme of a single tapered diode laser.

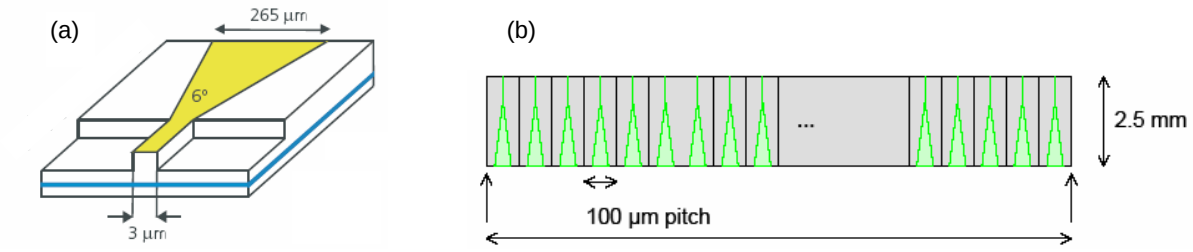

Figure 2.10: (a) Single emitter of a tapered HPDL [109]; (b) A laser bar designed from tapered HPDL wafer

In practice, the tapered structure have been fabricated with a large-gain-guide tapered section having a taper angle of 4^0 as well as narrow-index-guide tapers with small angle below 1^0 [106,107]. The large-angle gain-guide tapered lasers show indications of high astigmatism, together with a decreased beam divergence when output power increased. On the other hand, small index-guide tapered diode lasers

provide the negligible astigmatism, but have the drawback of an increase of the far-field divergence with power [106].

The fabrication technology of tapered diode lasers involves a combination of established processing tools for ridge-waveguide and broad-area diode lasers [108]. For tapered laser bar designs, as shown in Figure 2.10.b, a change of masks in the lithographic process might be sufficient in order to get the desired bar wafer. Other steps as metallization, cleaving of the mirror, facet coating, etc., are completely the same as BA laser. Therefore, the geometry structure (emitter width and number of emitter) of some tapered bars is similar to regular bars described in section 2.2.1. In the framework of our research, we have been investigated tapered laser single chips and bars with several designs with the target to achieve a better quality of high-brightness HPDLs.

2.2.4. Packaging of high power diode lasers

Packaging is the final but most cost-intensive process in the HPDL technology. It must fulfil two key requirements: perfect electrical contact and good heat transfer. For single emitter chips of HPDLs, these problems are already solved. The chip dimension is relatively small (cavity length ~ 1mm and width ~ few hundreds μm) so packaging induced strain will not be of substantial influence. Typically, HPDL single emitter chips are p-down (epitaxial layer contact directly with heatsink surface) packaged on standard heatsinks such as C-mount or SOT (Small Outline Transistor) by AuSn soldering material (Fig. 2.11). The n-contact is formed by a wire bonding technique.

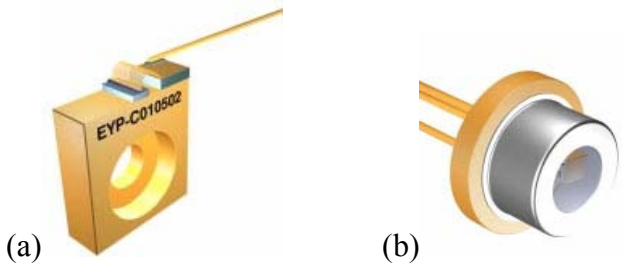

Figure 2.11: Package of single HPDLs: (a) C-mount; (b) SOT [110].

Packaging a HPDL bar is more difficult. In the high output power operating regime (typically several tens or few hundreds Watt), 30 – 50 % of the electrical power will convert into heat. A huge amount of waste heat is

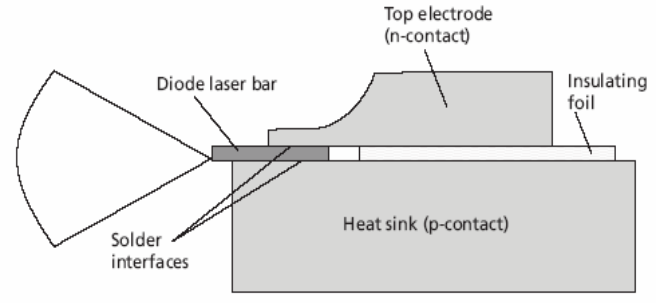

Figure 2.12: Structure of packaged diode laser bar [111].

released through a small area of the bar. Therefore, for laser bars, effective cooling is definitely required. The scheme in Figure 2.12 illustrates the mounting of a laser bar on a passively cooled heatsink. There are two kinds of standard heatsinks for HPDL bars. The first one is called "passively cooled" submount. This type is only used for laser bars with moderate output power and is usually mounted on Peltier coolers. For higher output power of HPDL bar, the second type of heatsink, namely "actively cooled" is used. This heatsink allows cooling water diffusion through micro-channels made inside body of submount. This provides efficient heat removal from the laser bar. Heatsinks usually are made of copper, copper-tungsten alloy, or diamond. Indium (soft material) and gold-tin (hard material) were chosen as soldering materials for the

(a) (b) (c)

Figure 2.13: Some typical geometries of HPDL bar package on: (a) and (b) passive cooled heatsink; (c) actively cooled heatsink.

packaging process. The discussion about disadvantages and advantages as well as choosing the suitable material for packaging leads directly to one of the main topics of this thesis, namely the creation of large amounts of packaging-induced strain.

The technical work of packaging process (i.e., bar alignment on the heatsink surface) is done under a microscope setup with the support of a vacuum gripping tool. [111]. Fig, 2.13 shows some typical geometries of laser bars after packaging process.

For a very high of output power, HPDLs are stacked one above the other [112]. With the stack technology, we have a "rectangular matrix" of emitters. The output power of such stack is expected to reach kW range. In Fig. 2.14, we can see the configuration of a stack packaged from single diode bars.

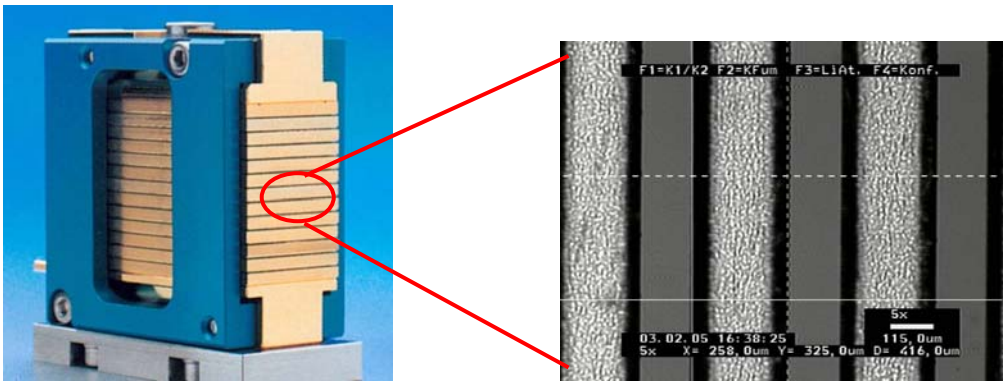

Figure 2.14: HPDL stack

2.2.5. Specifications of the samples under test

This section provides an overview of specifications of samples under investigation. The samples can be classified into four groups, namely BA bars (Bx), tapered bars (TBx), BA single emitters (Sx), and red-emitting devices (Rx). The details about the geometric structure were described in the preceding sections, as indicated in the last column of Table 2.1.

Table 2.1: Specifications of HPDLs under test

Batch	Wave-length	Lateral width	Structure/Material	Number of emitters	Package (heatsink/solder)	Ref. section
BA-1…9	808 nm	10 mm	SQW - InGaAlAs/AlGaAs	25	Cu /In	2.2.1
BB-1…3		10 mm		25	CuW /AuSn	
BC-1…3		9.5 mm		19	Cu /In	
BD-1		10 mm	DQW - InGaAlAs/AlGaAs	25	CuW /AuSn	
TB1-1…3	980 nm	10 mm	SQW - InGaAs/InGaAsP	20	Cu/In	2.2.1 & 2.2.3
TB2-11		6.4 mm		64	CuW/AuSn	
TB2-21,22						
SA1-1,2	980 nm	0.2 mm	SQW - InGaAs/InGaAsP	Single emitter	C-mount/AuSn	
SA2-1,2						
SB1-1	808 nm	0.2 mm	SQW - InGaAlAs/AlGaAs		CuW/AuSn	
SB1-2,3					Unpackaged	
SC1-1,2	915 nm	0.1 mm	SQW - InGaAs/InGaP		CuW/AuSn	
SC2-1,2			SQW - InGaAs/InGaAsP			
SC3-1,2			DQW - InGaAs/InGaAsP			
RA-1,2	650 nm	0.2 mm	SQW – InGaP/AlGaInP		C-mount/AuSn	2.2.2
RB-1,2						
RC-1,2						
RD-1,2						

Chapter 3.

Strain in high power diode laser arrays

External strains are one major source of degradation processes occurring in HPDL arrays. Therefore, the understanding of strain behaviors of HPDL arrays (nature, mechanisms and interactions with other parameters) is urgently needed. With the knowledge about strain-related effects in quantum structures described in chapter one, we now discuss strain-related effects in HPDL arrays.

3.1. Mechanical strain and methodology of strain investigation in semiconductor structures and devices

3.1.1. Packaging-induced stress

After the packaging process, the HPDLs experience a total strain including the following strain contributions [113,114]:

- The *misfit strain* contribution created during the growing process of the laser structures because the lattice constants of epitaxial layers are mostly different compared to the substrates. Furthermore, different thermal expansion coefficients of epitaxial layers and substrates cause strain, when the structure cools down from growing to ambient temperature.
- The *processing-induced strain* contribution that is consequence of post-growing processes before packaging, e.g., during metallization, polishing.
- The *packaging-induced strain* caused by the packaging process of the HPDL chips, which are cleaved from wafer, onto the heatsink.
- The *strain due to the creation of defects* that might be generated in HPDL structures, e.g. during operation.

While the first strain contribution belongs to the intrinsic strains, the others are considered external strains.

During the packaging of HPDL arrays (e.g. laser bars), the bar usually is soldered "p-side down" onto the heat sinks with a soldering material like Indium or Gold-Tin. Therefore, the soldered area must be heated up to a certain temperature T_s that is sufficient for melting of the soldering materials (e.g., $T_s \sim 157\ ^0$C in case of indium). At that time, both the semiconductor structure contacted to heatsink and the heatsink itself experience thermal expansion with different thermal expansion coefficients (see Table 3.1). When the system is cooled down to ambient temperature T_a, the semiconductor structure suffers an additional stress caused by non-equal thermal contractions of heatsink and QW semiconductor structure. We call this stress "packaging-induced stress". The consequence of this stress in the semiconductor structure is known as "packaging induced strain". Figure 3.1 depicts as an example of the possible deformation of a HPDL "cm-bar" under compressive packaging-induced stress. The maximum amount of packaging-induced strain is given by [Tomm-JAP99]:

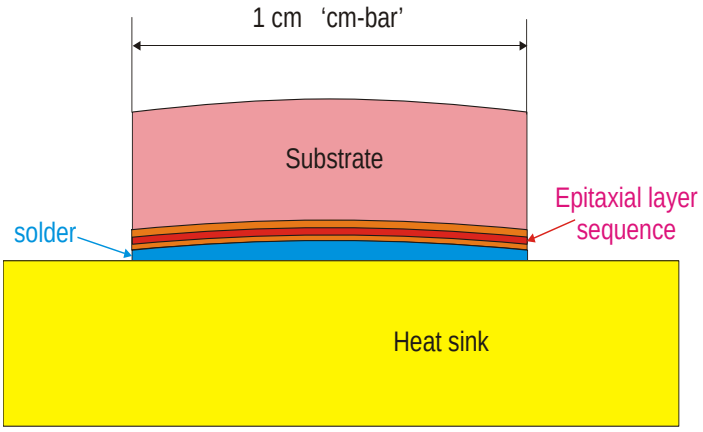

Figure 3.1: Deformation of HPDL "cm-bar" by packaging-induced stress

$$\varepsilon_p = (\alpha_{sem} - \alpha_h) \times (T_s - T_a) \quad , \qquad (3.1)$$

where α_{sem} and α_h are expansion coefficients of semiconductor and heatsink materials, respectively. $\varepsilon_p < 0$ means that the considered layer is compressed during cooling; whereas $\varepsilon_p > 0$ corresponded to tensile strain (e.g., $\varepsilon_p \approx$ -0.15% with GaAs-based devices packaged on copper heatsink by indium solder). Table 3.1 provides values of α_{sem} and α_h for some relevant semiconductors and heatsink materials that are used for HPDL fabrication.

There are two important results that we expect to get from studies of packaging induced strains in HPDL. The first one is which configuration of the strain influences the HPDLs during packaging process, i.e. the symmetry of packaging induced strain. The second one is the amount of external strain that the HPDL structure experiences. Basically, the packaging-induced stress will not transfer completely to the semiconductor structure, because it is buffered some extent by the soldering material, especially, when a "soft" soldering material is used, e.g. Indium. Therefore, we must

do the strain measurement in order to quantify: To what extent is the strain transferred through the solder material towards the optical active layer of the semiconductor devices?

Table 3.1: Thermal expansion coefficients of some relevant semiconductor materials and heatsinks ($\times 10^{-6}\,K^{-1}$) [115-117]

Semiconductor materials				Heatsink materials	
GaAs	5.7	$Al_{0.3}Ga_{0.7}As$	6.2	Cu	17
InAs	4.5	$Al_{0.45}Ga_{0.55}As$	5.9	CuW	6.0
InP	4.6	$In_{0.47}Ga_{0.54}As$	5.9	Diamond	1.5
GaP	6.9				

3.1.2. Extraction of information on strain from photocurrent spectra

In chapter one, we introduced the PC spectrum that can be analyzed like an absorption spectrum. In this section, we present how we analyse the PC spectra to get information on strain in HPDLs. The spectral position of the optical transitions within a QW depends on the mechanical strain that the QWs experiences. Therefore, if we can extract the spectral positions of optical transitions from PC spectra, we are able to get information on the strain.

The PC spectra of QW structures show a staircase-like shape (Fig. 1.2), which includes broadening effects as represented in Fig. 1.3. In the PC spectra, the absorption edges are caused by the onset of the optical transitions. With the assumption of symmetric broadening as Fig. 1.3, taking the first derivation of PC spectra, we will see peaks on first derivative curves that show the onset of the steps (or absorption edges) related directly to certain transitions within the QW structures. Based on the first derivative curves of the PC spectra, the analysis of the shifts of the peaks provides information about the strain in QW structures of HPDLs.

In Fig. 3.2 (a), we present PC spectra measured on 808 nm HPDL double QW structure. The non-polarized PC spectrum (solid line) is differentiated to obtain the first derivative spectrum shown in Fig. 3.2 (b). Two pronounced peaks corresponding to the transition energies of 1.539 eV 1.577 eV represent the two lowest quantum-confined transitions in this QW. These transitions are the hh1-e1 and lh1-e1. The energetic distance between two transitions shows the split of hh1 and lh1 subbbands, in this case about 40 meV for this AlGaAs-waveguide-based HPDL structures [48]. To confirm the assignment, we perform linear polarization resolved PC measurements for the same device. The two polarization-resolved PC spectra were added to Fig. 3.2 (a) with dotted line for TE and dashed line for TM. The description of TE- and TM-

polarization is given in section 1.1.2 and Fig. 1.5. These measurements clearly show two different absorption edges for TE and TM polarized radiations. Based on the selection rules for optical spectra (section 1.1.2), we can now distinguish between the hh1-e1 and lh1-e1 transitions by comparing relative intensities of the absorption peaks in the first derivative polarized PC spectra TE and TM displayed in Fig. 3.2 (b). An additional peak appears at 1.557 eV. This is typical for double QW structures and the origin and nature of this peak is not fully clear. This peak may be related to the peculiarities of hh-lh mixing in QW [114,118]. It also could be the hh2-e1 transition that violates the in-plane selection rules [119]. Therefore, it must be distinguished from the lh1-e1 transition and we do not use it for strain analysis.

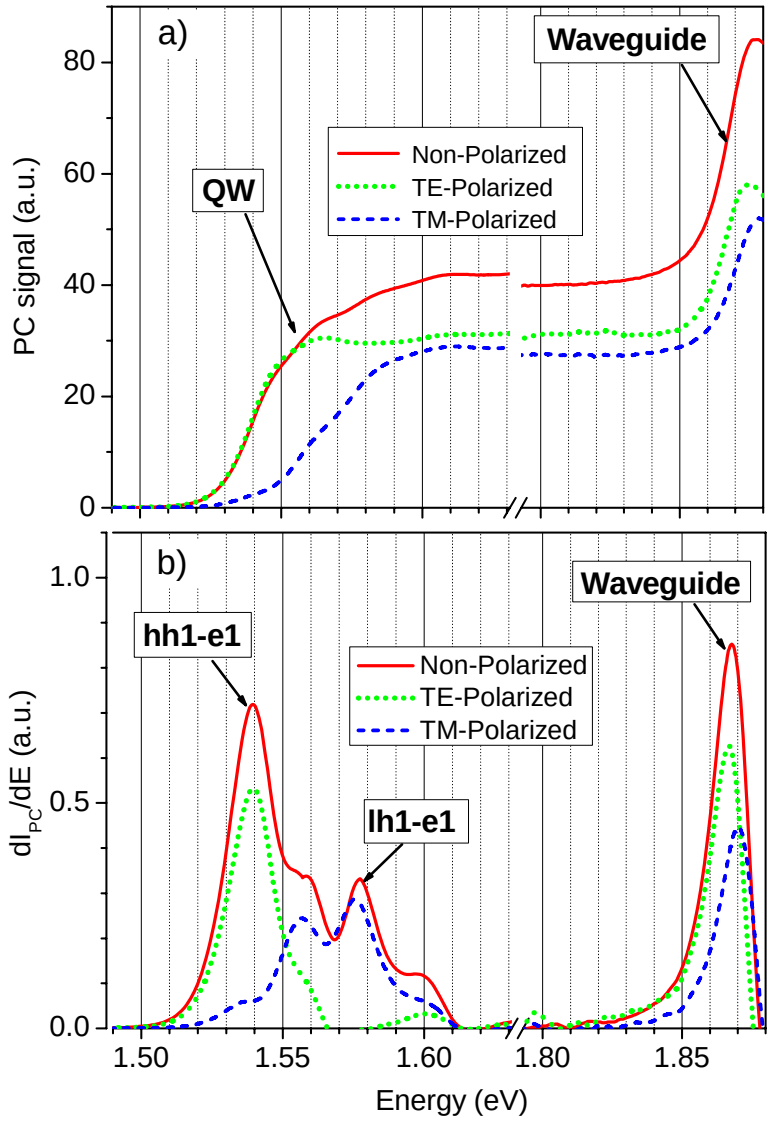

Figure 3.2:
a) Normalized PC spectra measured at a 808 nm HPDL double QW structure (non-polarized: solid line, TE-polarized: dotted line and TM-polarized: dash line);

b) First derivatives of the corresponding PC spectra in Fig. 3.2 (a) show the onsets of the absorption edges of the optical transitions in QW and waveguide.

As one can see in Fig. 3.2, a second edge at about 1.865 eV indicates the onset of the absorption of the waveguide. The peaks in the first derivative curves are also shifted when strain is applied. Thus the information of strain in the waveguide can be extracted by an analysis procedure similar to the way done for QWs. By using

polarization-resolved measurements, we also observe the split of hh1-e1 and lh1-e1 transitions in the waveguide, where because of the absence of strain, hh1 and lh1 are degenerated.

One should note that the information on packaging-induced strain achieved from QW and waveguide transitions shifts is expected to be the same, since the QW is physically embedded in the waveguide. The QW transitions are usually considered for strain analysis, because they are expected more sensitive to strain. However, in some particular cases, doing analysis both QW and waveguide results is necessary to exclude the influence of interfering parameters. The waveguide absorption edge is independent on QW parameters such as QW width or composition. Thus one can say that both of the analyses complement each other.

The above procedure provides a tool to determine spectral positions of hh1-e1, lh1-e1 and waveguide transitions in HPDLs. If there are reference levels for comparison of the spectral positions, we can easily realize the shifts that are proportional to the strain. With the coefficients of strain sensitivities in Table 1.3, we are able to measure the amount of strain in the HPDL structure compared to a reference level. The procedure of strain analysis involves a high reproducibility. The deviation of the measured peak position is estimated to be better than 0.3 meV [120]. This allows measurements of strain-induced spectral shifts with an accuracy of better than 0.3 meV. Therefore, we can use the method to extract, e.g. aging-induced shifts of optical transitions on a scale of below meV by measuring the HPDLs before and after operation including the motion of the devices from one setup to another one.

3.2. Investigation of strain in regular high power diode laser bars and high power diode laser stacks

3.2.1. Packaging-induced strain in In-packaged high power diode laser bars

Based on the methodology presented in the preceding sections, we are able to do a strain analysis for one specific type of HPDL arrays, namely In-packaged HPDL “cm-bars”. The device that is used as test sample is the standard 808 nm cm-bar BA-1. The structure and geometry were described in section 2.2 (see Table 2.1). The QW layer of this cm-bar ($In_{0.06}Ga_{0.86}Al_{0.08}As$) is compressively strained due to a lattice mismatch of -0.45 % (intrinsic strain), whereas the $Ga_{0.7}Al_{0.3}As$-waveguide is compressed by almost an order of magnitude less. When the ‘cm-bar’ is soldered onto a regular Cu heatsink using indium (melting temperature $T_s \sim 157$ °C), it experiences a compression during cooling to ambient temperature. Thus, after the packaging process, a uniform, compressive, maximum packaging-induced strain of $\varepsilon_p \approx -0.15\%$ (calculated by Eq. 3.1 with data from Table 3.1) could potentially be introduced into

the laser structure.

PC spectra are obtained from the cm-bar by using the setup presented in section 2.1.2. This measurement is performed by scanning the excitation beam to each emitter of the bar. After that, the PC spectra are analyzed to obtain the spectral position of the optical transitions, namely hh1-e1, lh1-e1 and waveguide. The spectral position for each optical transition is plotted versus local position of the emitters on the cm-bar in Fig. 3.3. The results from Fig. 3.3 allow analysis of strain in the In-packaged bar.

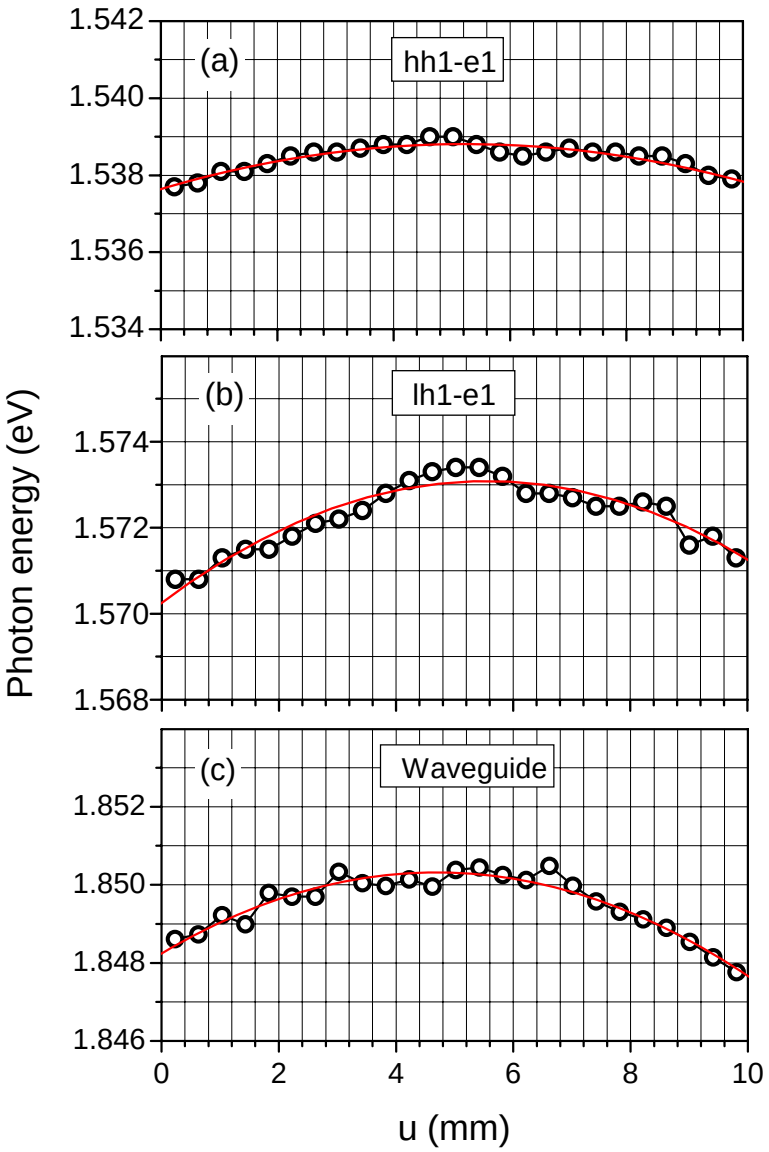

Figure 3.3:

Spectral positions of the optical transitions versus lateral local position of the In-packaged HPDL cm-bar on a copper heatsink, emitting at 808 nm (device BA-1). The photon energy shifts are due to packaging-induced strain. The data are extracted from PC spectra measured along u axis (lateral axis) of the bar:

(a) hh1-e1 transitions;
(b) lh1-e1 transitions;
(c) waveguide transitions.

The solid curves represent polynomial fits of the data sets.

Before starting a detailed discussion, we should address two important issues. Firstly, from result of thermo-mechanical finite element modeling (FEM), the 'cm-bar' experiences strain primarily along the <110> direction (i.e., uniaxial strain), with a nearly continuous strain distribution from the device edge toward the center where the strain maximum is expected. Fig. 3.4 show this result obtained by thermo-mechanical FEM describing the strain distribution along an In-packaged HPDL bar on a copper

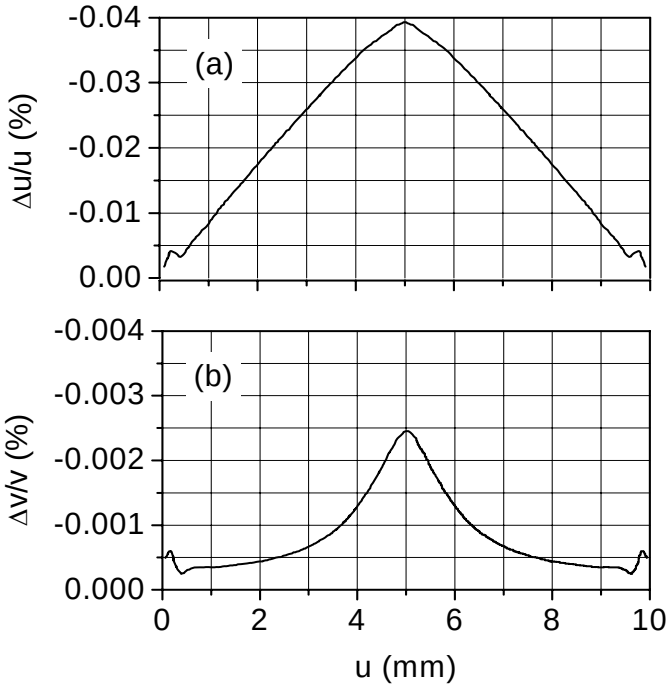

Figure 3.4:

The distribution of packaging-induced strain in the active region obtained by themo-mechanical FEM [58]:
(a) along the cm-bar (u-axis);
(b) along cm-bar's emitter cavity (v-axis).
The ordinate scale in (a) is one order larger to display substantial higher of strain magnitude along u-axis.

heatsink. Secondly, packaging-induced strain is assumed causing, in addition to all intrinsic strains, the additional deformation by the same amount in the QW and the waveguide in which the QW is embedded [58].

Our results from Fig. 3.3 agree with the above prediction, the maximum shifts of spectral positions are located at center emitters, i.e. maximum strain, building the strain distribution along cm-bar in the shape of a "bow" (solid lines in Fig. 3.3). We assume that the edges of the bar are nearly unaffected by packaging-induced strain, cf. Ref. [121]. Therefore, we obtain the maximum shifts of spectral positions between center emitters and edge emitters ΔE ("bow" amplitudes) are approximately 1.2 meV for hh1-e1 transition, Fig. 3.3 (a), and 3.0 meV for lh1-e1 transitions, Fig. 3.3 (b), and 2.4 meV for waveguide transitions, Fig. 3.3 (c). From these results, we discuss the strain in "cm-bar" by addressing the two following points:

- Firstly, we address strain configuration applied to the waveguide structure of the cm-bar. In section 1.2.3, the discussion about strain configuration (in case of compressive intrinsic strain and compressive packaging-induced strain) was done based on the ratios between the shift of hh1-e1 transitions and the shift of lh1-e1 transitions. In this case, we keep the assumption of strain-free cm-bar edge and thus using the edge spectral position as reference, i.e. zero level for the spectral shift. Taking the ratios between the spectral shifts of the relevant hh1-e1 and lh1-e1 transitions for each local position in Fig. 3.3 (a) and (b), we obtain the results plotted in Fig. 3.5. The ratios are almost inside the range between 0.16 - 0.37 (marked area in

Fig. 3.5), which is a signature for uniaxial strain [52]. Therefore, the strain induced to the cm-bar structure is rather of uniaxial geometry.

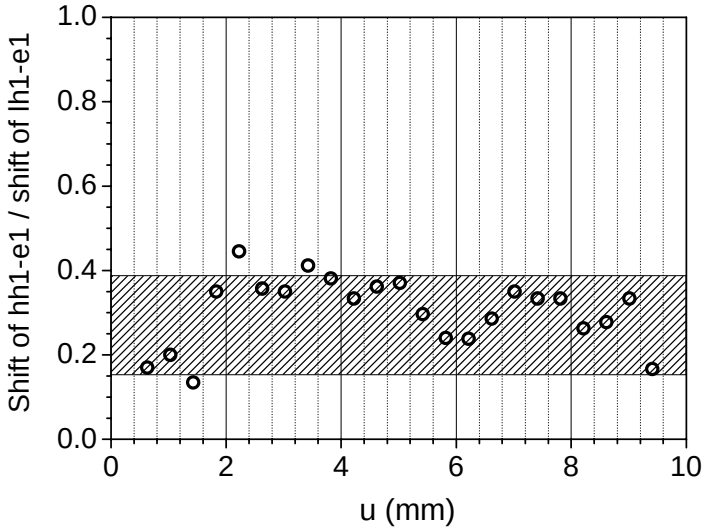

Figure 3.5:

The ratios between the shifts of hh1-e1 transitions and shifts of corresponding lh1-e1 transitions along the cm-bar BA-1: the result is obtained from the data shown in Fig.3.3 (a) and (b). The marked area is the range specific for uniaxial strain.

- The second topic is the absolute value of the packaging-induced strain transferred to the epitaxial layer sequence of the cm-bar. First of all, we denote the energy shifts of hh, lh, and waveguide transitions with ΔE_{hh}, ΔE_{lh} and ΔE_{wg}, respectively. Taking the appropriate energy shift per strain coefficients $(\Delta E/\Delta\varepsilon)$ from the Table 1.3 for the respective optical transitions (hh1-e1, lh1-e1 and waveguide) for the extrinsic uniaxial strain configuration along <110> direction, as pointed out above, we obtain strain values from the shifts of the transitions as following:

$$\begin{aligned}
&\text{hh1-e1} &&: \varepsilon_{hh} = \Delta E_{hh}/(\Delta E_{hh}/\Delta\varepsilon) = 10^{-1} \times 1.2/(-2.12)\ (\%) \approx -0.056\ \%\\
&\text{lh1-e1} &&: \varepsilon_{lh} = \Delta E_{lh}/(\Delta E_{lh}/\Delta\varepsilon) = 10^{-1} \times 3.0/(-5.69)\ (\%) \approx -0.053\ \%\\
&\text{waveguide} &&: \varepsilon_{wg} = \Delta E_{wg}/(\Delta E_{wg}/\Delta\varepsilon) = 10^{-1} \times 2.4/(-4.24)\ (\%) \approx -0.057\ \%
\end{aligned}$$

Here, the strain coefficient for waveguide transition was taken as the average value of the coefficient for hh-waveguide transitions and the coefficient for lh-waveguide transitions from the Table 1.3 (cf., Ref. [122]).

These results give us an average strain value in QW structure of cm-bar of $\varepsilon \sim$ (-0.055 %). This value indicates that in this particular case about one third of the maximum packaging-induced strain ($\varepsilon_p \approx$ -0.15 %) is transferred into the waveguide of the "cm-bar" through the indium layer. The residual strain is released in the In-soldering layer, relaxed by defect creation and other mechanisms, which will be discussed later.

The results shown here are a typical example for the strain behavior of the cm-bar packaged on copper heatsinks by indium. The key point, which we would like to emphasize, is the methodology based on PCS for strain investigation of HPDL bar in general. The approach presented above allows a determination of packaging-induced

strain in HPDL bar with both absolute strain value and strain symmetry configuration that are a valuable information required, e.g. for the optimization of packaging techniques.

3.2.2. Strain measurement of high power diode laser arrays by Degree of Polarization of Photoluminescence and cross calibration to Photocurrent Spectroscopy

Polarized PL provides another possibility to measure strain in HPDL. In this section, we will present the results of strain analysis in HPDL bar obtained by DOP-PL. After that, the results from the same bar achieved by PCS provide the cross calibration between the two methods.

Strain can destroy the crystal symmetry of semiconductor materials, resulting, e.g., in splits of the heavy hole and light hole bands, and causing a enhanced probability of emission of light polarized in the direction of a compressive strain (in the case of tensile strain this probability is reduced) [123]. The DOP of luminescence for III-V single crystal material is known to be a function of the strain in the material. The DOP of luminescence for light propagating in the *v* direction of the bar is defined as:

$$\mathrm{DOP}_v = (L_{uu} - L_{ww})/(L_{uu} + L_{ww}) \quad , \qquad (3.2)$$

where *u*, *v*, and *w* are orthogonal directions of the bar (see Fig. 1.11), and L_{ii} is the intensity of luminescence that is integrated over all energies, is propagating in the *v* direction, and is polarized along the *i* direction [124]. Under the assumption of an isotropic material, it has been shown that:

$$\mathrm{DOP}_v = - C_\varepsilon \times (\varepsilon_{uu} - \varepsilon_{ww}) \quad , \qquad (3.3)$$

where C_ε is a positive calibration constant, ε_{uu} and ε_{ww} are strain along *u* and *w* direction [95,97]. Equation (3.3) defines a relationship between the DOP and the difference of the normal components of strain.

Another option of polarized photoluminescence, namely ROP, is an independent measurement of the DOP by rotating the measurement axis 45^0 about the *v* axis (i.e., sample is rotated 45^0 in *uw* plane). The rotated DOP in the *v* direction (i.e., ROP_v) related to shear strain (or stress) component and is given by [97]:

$$\mathrm{ROP}_v = 2C_\varepsilon \times \varepsilon_{uv} \quad , \qquad (3.4)$$

where ε_{uv} is the shear strain obtained by rotating the tensor components by 45^0 clockwise about the *v* axis. These two polarized photoluminescence measurement approaches presented here provide means for determining normal and shear

components of the strain in a HPDL bar.

The device under test is the nineteen-emitter-HPDL bar BC-1 that operates at 808 nm. Because of In-packaging process on a copper heatsink, the device experiences also a predominantly uniaxial packaging-induced strain along <110> direction [58]. Additional strain contributions within the semiconductor arise (even before packaging) from processing such as the deposition of contacts at the p- and n-side. These contributions are expected to have the same symmetry as the built-in strain of the QW,

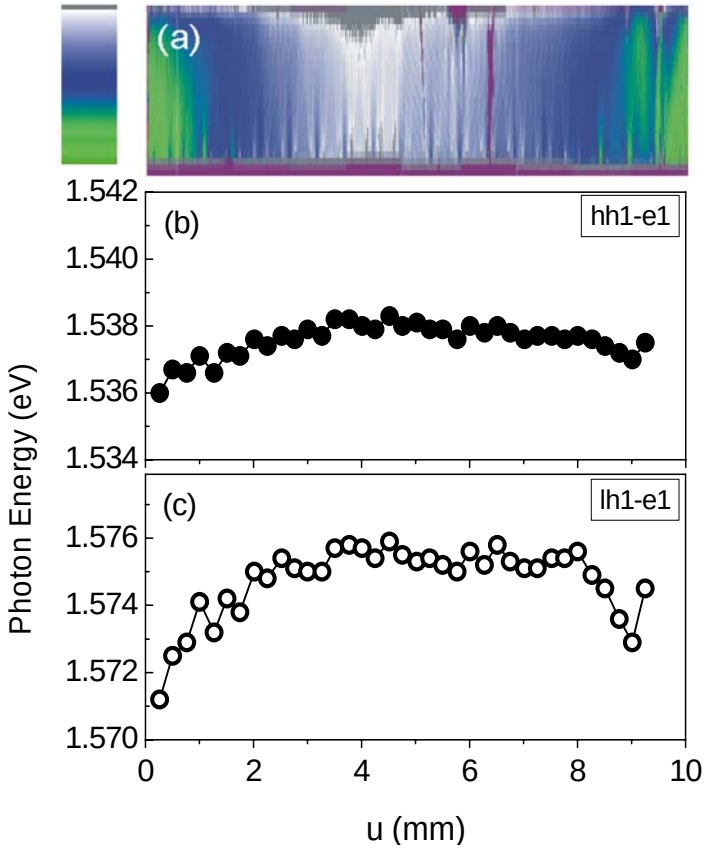

Figure 3.6:

(a) DOP-PL map from the front facet of the laser array BC-1. The bar code shows the relative scale used to display the data within the range (0-5.8) %.

(b) Photon energy of the hh1-e1 transition in the QW along the array as determined by PCS.

(c) Photon energy of the lh1-e1 transition in the QW along the array as determined by PCS.

The u-axis scale applies for all three data sets.

namely biaxial within a (001) plane [97].

The DOP-PL measurement for the HPDL bar is measured with the setup described in section 2.1.5. In Fig. 3.6 (a), we show DOP-PL map achieved from front facet of the laser bar. The data were recorded by scanning the front facet with 4 µm steps in the horizontal direction and 1 µm steps in the vertical direction.

The strain in the bar is extracted from the DOP-PL data of Fig. 3.6 (a). From this data of DOP-PL map, we performed an averaging of DOP-PL intensity over a region that is 10 µm above the active region and is 40 µm wide and 3 µm high. The strain value is then obtained by dividing this data by the calibration constant $C_\varepsilon = (50 \pm 10)$ for GaAs [97]. After that, these values are plotted in Fig. 3.7 a. The maximum of strain value in vicinity of center of the bar shown in Fig. 3.7 (a) is approximately - 0.1 %.

The PCS measurements on the laser bar were done at stabilized ambient temperature of $T = (25.00 \pm 0.05)$ °C and were performed at each emitter of the bar. In

Fig. 3.6 (b) and (c), we plotted the spectral positions of two optical transitions (hh1-e1 and lh1-e1) that were extracted in the same way as presented in preceding sections. Assuming the left array edge to be unstrained (zero reference) and strain to be uniaxial along <110> direction, we divide the observed spectral shifts by the strain sensitivities of -2.12 and -5.69 eV per unit strain for the hh1-e1 and lh1-e1 transitions, respectively [Table 1.3]. The strain profile as determined by PCS is shown in Fig 3.7 (b). In fact, the hh1-e1 related data are systematically larger by a factor of (1.2 ± 0.05) than the lh1-e1 related ones. This indicates a small strain contribution of higher symmetry, e.g., a biaxial one.

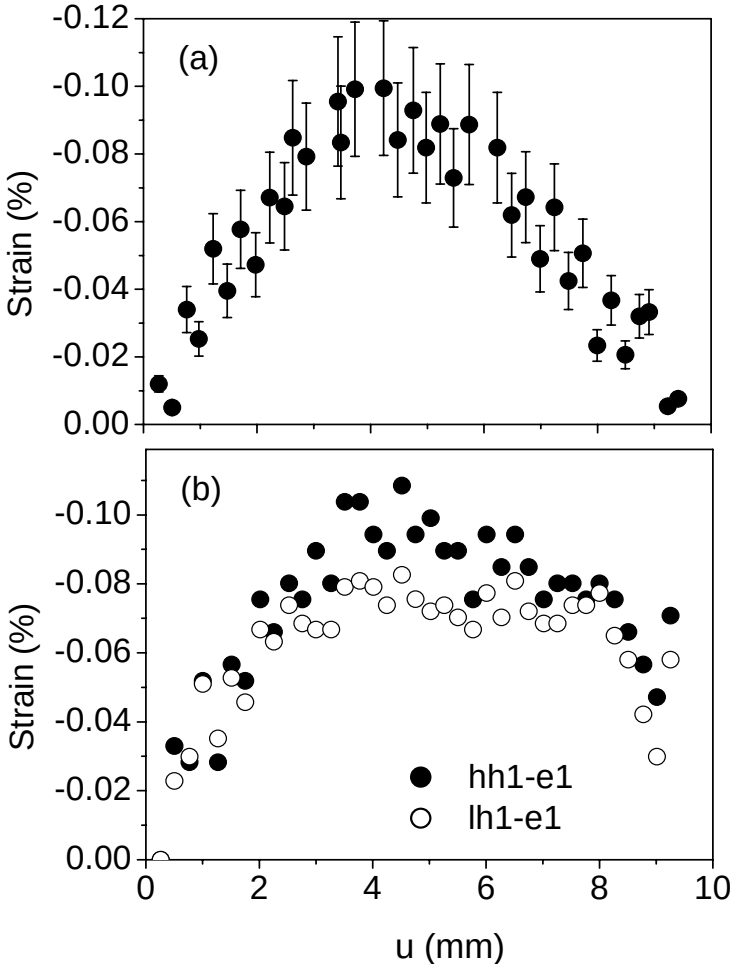

Figure 3.7:

(a) Strain distribution along the bar BC-1 extracted from DOP-PL data in the region 10 µm above active region. Each data point is average of intensity of an area with 40 µm wide and 3 µm high. After that, division by the calibration constant of C_ε = (50 ± 10) was done.

(b) Strain profile as determined by PCS along the HPDL array obtained from analyzing both hh1-e1 (solid circles) and lh1-e1 (open circles) transitions with the assumption of the left array edge to be unstrained (used as zero reference level).

From the DOP and ROP measurement, we also can obtain some information about processing-induced strains. Fig. 3.8 shows high resolution maps of DOP and ROP measurement at one of the emitters in center of the bar (region 5.0 - 5.5 mm). In Fig. 3.8 (a), the DOP map shows the impact of the n-contact metallization on the emitter. The enhancement of DOP intensity at the upper region of the substrate (displayed in blue) clearly reveals the top region of the GaAs substrate to be compressed. We do not see a similar signature in the ROP data presented in Fig. 3.8 (b). This indicates the absence of shear components. This situation is exactly what one

expects for a biaxial strain. The behavior is very likely caused by the metal deposition on the (001) plane when forming the top contact. Thus the data shown here clearly confirm the assumed symmetry of this processing-induced strain component. Although the impact is weaker, also the p-contact, at the bottom of Fig. 3.8 (a) illustrates some compression caused by metallization. In both of DOP and ROP maps, we see the strain fields, which are a result of the small grooves (marked by arrows) separating the emitter from each other.

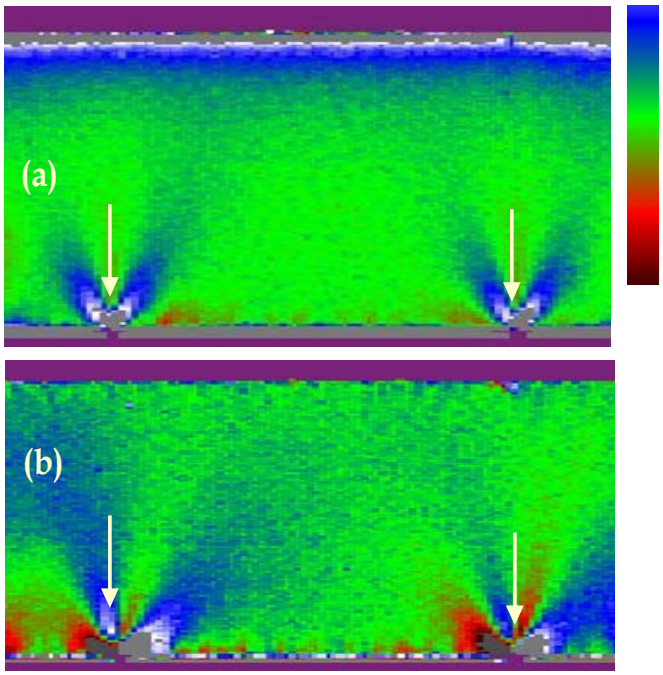

Figure 3.8:

High-resolution DOP- (a) and ROP-PL maps (b) of the region between 5 mm and 5.5 mm [in Fig. 3.6 (a)] with one emitter stripe of the bar BC-1(in center) and passive sections on the left and the right recorded with steps sizes of 1 µm in the vertical direction and 4 µm in the horizontal direction. The arrows show the positions of grooves. The bar code represents the relative scale used to display the data within the ranges (3.65-6.55) % and (-1.07-0.87) % for DOP and ROP, respectively.

Now we address the implications of our experimental results. First, we point to the 'cross-calibration' of the two methods. Obviously, the strain distributions shown in Fig. 3.7 (a) and (b) look very similar and even the quantities agree within the experimental uncertainty. As we know, the probe-volumes, i.e., those parts of the device from which the signal is extracted and is averaged over, of both methods differ. The PCS measurements were made at the QW material while the DOP measurements are performed at the substrate material 10 µm above the QWs. Nevertheless, the finding of agreement within experimental uncertainty is not surprising, since the gradients, at least of the packaging-induced uniaxial strain, which is used as the exclusive gauge here, are rather weak on this scale. The same fact has been discovered, when comparing PCS with micro-PL, which has the same probe-volume as DOP-PL [122]. We consider the quantitative agreement also a justification of the key assumptions involved into the two approaches, such as the theory on the strain sensitivities [52,58] for PCS and the determination of the DOP calibration constant C_ε.

In this section, we presented results obtained by another methodological approach for the estimation of strain in III-V semiconductor devices, namely DOP-PL.

After that, the two methods, DOP-PL and PCS, are compared by analyzing an HPDL bar that is spatially inhomogeneously strained due to packaging-induced stress. Cross-calibration becomes possible because of the known symmetry of this strain contribution. The comparison shows the compatibility of the two different approaches. The DOP-PL method has the higher spatial resolution than PCS and is potentially quicker, but provide less information from a single data point [97]. Both methods, DOP-PL and PCS, demonstrate the ability to obtain even details on strain symmetry, in particular, if applied in a concerted way as demonstrated here.

3.2.3. Investigation of strain in high power diode laser stack

In this section, we discuss about results on strain investigations in HPDL arrays based on stack technology [112,125] that, to the best of our knowledge, have not been studied regarding their photoelectric properties so far.

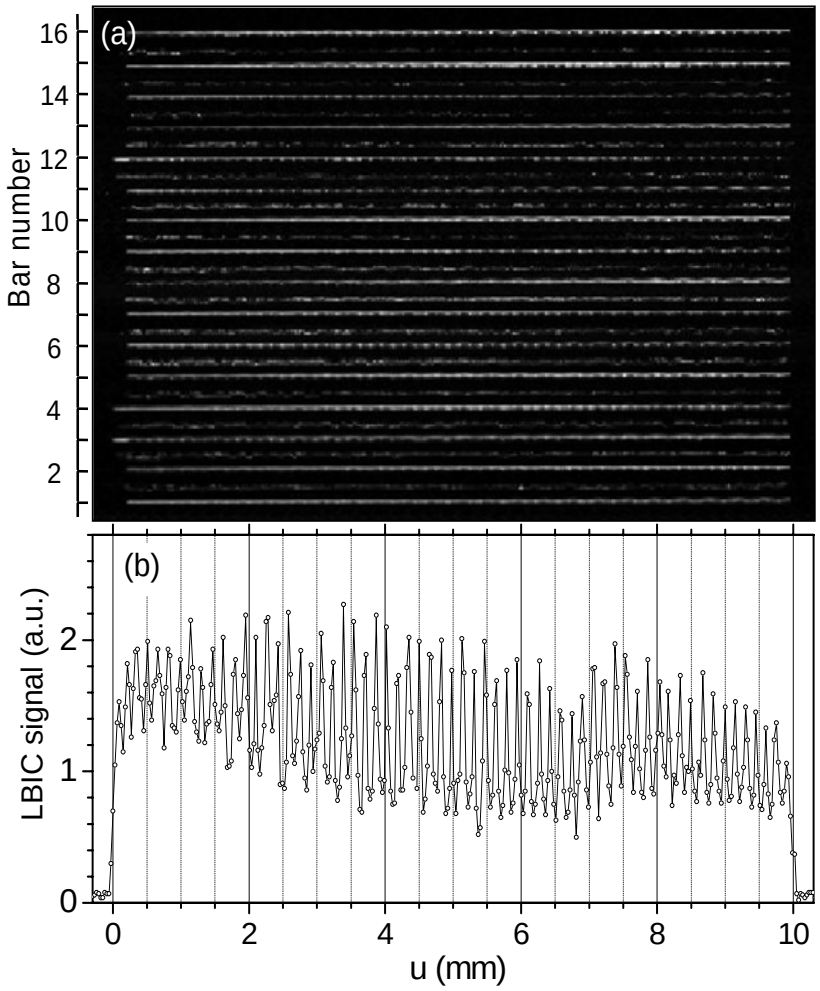

Figure 3.9:

(a) Map of the LBIC intensity scanned over all surface of a stack with a width of 1.1 cm and height of 0.7 cm. The spatial resolution is about 30 μm for both vertical and horizontal direction. A higher brightness indicates a higher LBIC intensity.
(b) LBIC scan along the active region along one bar shows the lateral structure of the bar. The data is taken from bar number 3; map of Fig (a).
The abscissa scale of (b) applies also to (a).

The stack under test can generate an optical output power up to 1.6 kW. It includes 16 cm-bars. Each bar is sandwiched between expansion-matched heatsinks and packaged by Au-Sn solder. The bar inside the stack consists of 65 individual

single emitters with a center-to-center-distance between the emitters of 150 µm. In Fig. 3.9, we show an LBIC scan across all the surface of the stack with 633 nm excitation wavelength. The spatial resolution of the scan is 30 µm for both horizontal and vertical directions. Fig 3.9 (a) is gray-scale map of the LBIC signal intensity with 1.1 cm width and 0.7 cm height. The active regions of the bars are located at the brighter lines in the map as indicated in left-side scale of Fig 3.9 (a). Beside that, we found the LBIC signal to be present also between two bars. It seems to be generated in the GaAs substrate region in vicinity of the n-contact. Fig. 3.9 (b) shows plot of LBIC signal profile at active region along one bar revealing its lateral structurization. Analysis of all these profiles shows the emitters at the left and right edge of many bars inside the stack to be systematically damaged by processing.

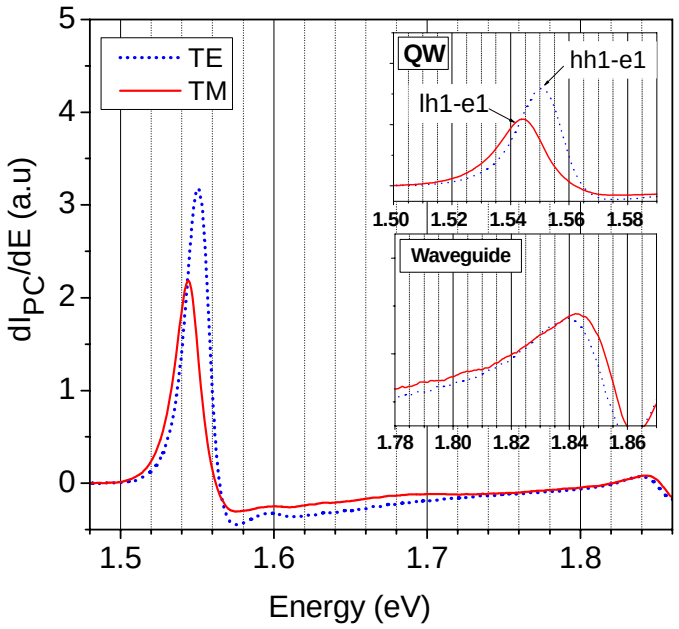

Figure 3.10:

First derivative of polarized PC spectra from the HPDL structure of the stack: the dotted curves represent results from TE polarized spectra and solid curves TM ones. The inset for the QW region shows the spectral position of hh1-e1 and lh1-e1 transitions (TM polarized curve is red-shifted) while the inset of waveguide shows a blue shift of waveguide transitions in TM polarization.

In polarized PC overview measurements, with TE and TM polarizations, we observed the lh1-e1 transition that corresponds to TM curve shifts about 7 meV to lower photon energy compare to the hh1-e1 transition that is represented by the TE curve (see inset QW in Fig. 3.10). Nevertheless, the behavior does not occur in the waveguide, i.e. absorption photon energy is higher for the lh1-e1 transition as expected for (almost) unstrained bulk material. Since the QW is embedded in the waveguide, this opposite behavior shows a tensile intrinsic strain present in the QW layer of the stack-emitters that is confirmed by the red shift behavior of lh1-e1 transition in QW as discussed in section 1.2.2 and Refs. [48,126]. For this structure, the intrinsic tensile strain of the QW is about 0.4 %.

For the strain investigation, we perform PC measurements that scan over all emitters inside the stack. At each emitter, a PC spectrum was collected with a signal to

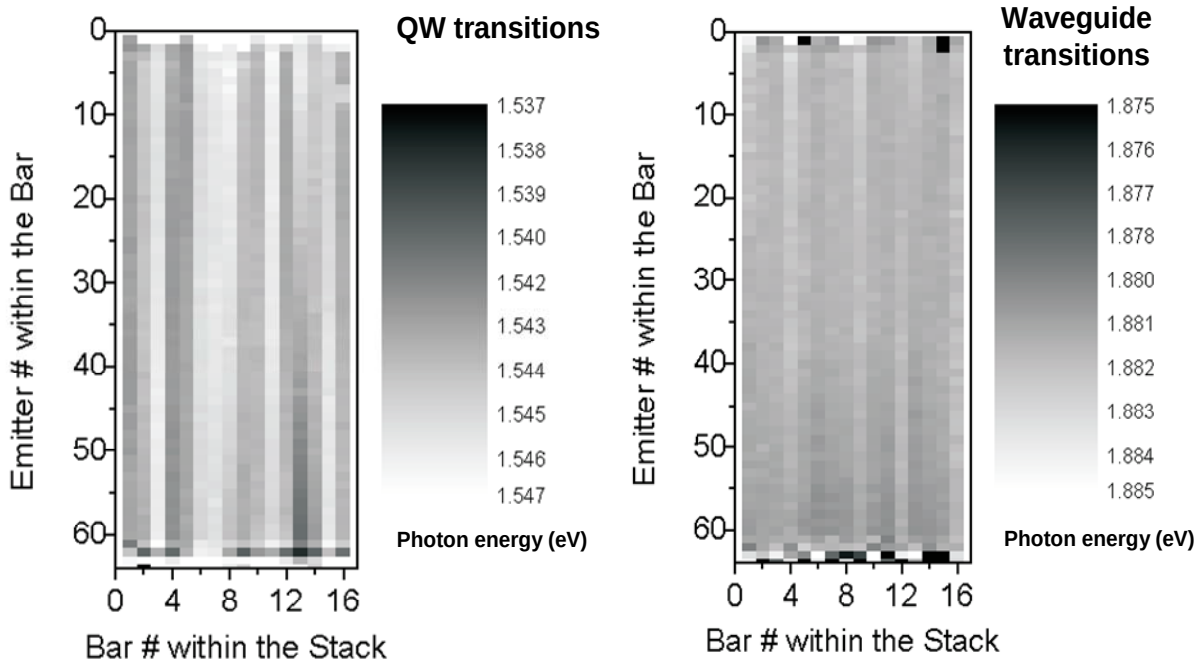

Figure 3.11: Mapping of spectral position of the QW transition and waveguide transition in a high power diode laser stack. The results were extracted from photocurrent spectra that are measured at each emitter inside the stack.

noise ratio of better 10^4. From the PC spectra, we took the first derivative to obtain the spectral positions for QW and waveguide transitions. These values are plotted as map ordered by the bar number within the stack and the emitter number inside each bar. Fig. 3.11 represents the results of QW and waveguide obtained from this analysis of the PC spectra measured on the stack. The gray-scale of the maps shows a visual comparison of the shifts of spectral position for both QW and waveguide. From the results obtained here, we now discuss the strain status of the device. Firstly, we should exclude the unusual behaviors of the emitters at the left and right edge of the bars in the stack in discussions, because these emitters were obviously damaged by the stacking-technology as shown in the LBIC measurements. A clear difference between waveguide and QW transition behaviors, which we can see in two maps, is homogeneity. The spectral positions of the QW transitions show a more inhomogeneous distribution inside the stack as the waveguide. The fluctuation of the QW spectral position inside a bar of the stack is from 0.5 meV to 5.5 meV and across the stack 7 meV. For the waveguide, the respective values are smaller with 0.5 meV to 2.5 meV and 3 meV, respectively. Thus the waveguide map appears more homogeneous. This behavior is quite clear because reproducibility of our measurements is better than 0.3 meV.

The analysis of strain in the stack, which may explain the observed behaviors of the two spectral position maps, needs strain sensitivities for both QW and waveguide transitions. With the conditions of 0.4 % intrinsic tensile strain for QW and zero intrinsic strain for waveguide, from data of Table 1.3, the strain sensitivities can be extracted with values of about -7.3 eV and -4.2 eV for QW and waveguide transition, respectively. Thus theory predicts a factor of almost two stronger for the shift of the QW transitions compared to the waveguide ones caused by the same amount of strain. If one now assumes that the inhomogeneity of the maps is exclusively caused by strain, the different observed homogeneities could be already explained. This assumption, however, would lead us to the prediction of a strong correlation between QW and waveguide data within each single bar of the stack.

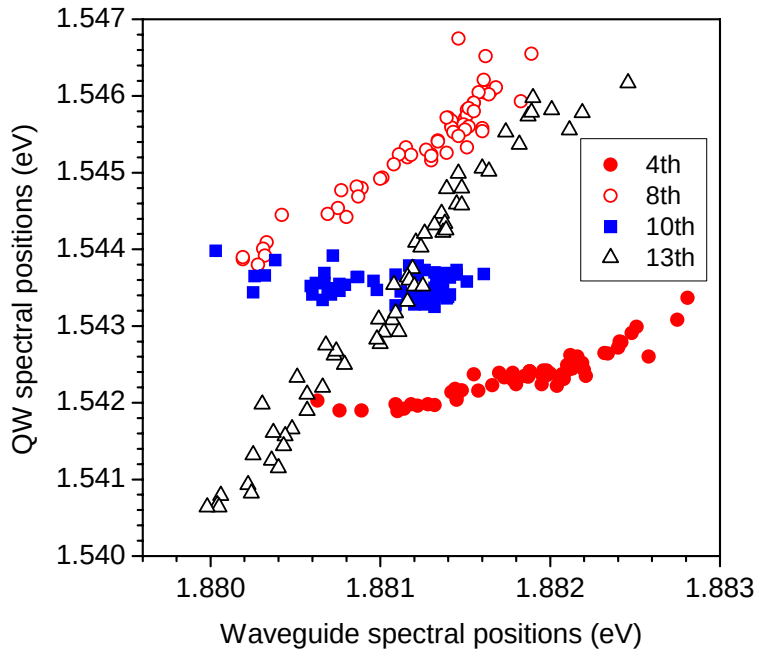

Figure 3.12:

Correlation between QW- and waveguide spectral positions along single HPDL bars inside the stack: The data sets are taken from bars number 4, 8, 10, and 13, which represent all observed behaviors of the evolution of QW data versus the evolution of waveguide data.

We now check this correlation. First, we plot the QW spectral positions versus waveguide spectral positions in Fig 3.12. In this figure, four data sets of the bar number 4, 8, 10 and 13 represent all observed behaviors of evolution of spectral positions (for both QW and waveguide transition) along one bar. When we compare QW and waveguide transitions along a bar, we find two different behaviors: some bars show the same evolution tendency and some others not. For example, in Fig. 3.12, we consider two representative bars, namely number 8 and number 13. In these bars, both QW and waveguide behave the same effect. The QW and waveguide transitions are increased by 3 meV and 1.7 meV for bar number 8 and 5.5 meV and 2.7 meV for bar number 13. These shifts correspond to maximum amounts of strain in bar number 8 and 13 to be about -0.04 % and -0.07 %, respectively (strain sensitivities here are -7.3 eV and -4.2 eV as were addressed above). We learn also from these bars: the QW

shifts always exceed the waveguide ones (with factors of about 1.8 and 2). This is consistent with the strain sensitivities and their ratio. Thus the behavior of these bars is consistent with the hypothesis of a inhomogeneity caused by packaging-induced strain. Another behavior was found for some other bars. For example, the bar number 4 shows a weak increase of the QW spectral positions (1.2 meV) as compared to waveguide one (2.4 meV) and the bar number 10 gives a slight decrease of the QW transitions (0.5 meV) while the waveguide transition are even increased by about 1.5 meV. These results are inconsistent with the strain sensitivities of QW and waveguide, i.e., the QW transition shifts is weaker than the waveguide one, and both QW and waveguide transition shifts show the same tendency. This finding points to an additional source of inhomogeneity, namely grown-in wafer-inhomogeneity. Therefore, the strain and structure inhomogeneity effect may contribute independently or coherently to these particular bars showing very different behaviors. However, because the observed behavior is very complicated, the complete explanation should be only carried out after further careful investigation performed to confirm this hypothesis.

3.3. Evolution of mechanical strain in high power diode laser arrays

Mechanical strain can potentially modify standard laser parameters, e.g. the emission wavelength. In this section, we will discuss the evolution of this strain in the QW of HPDL arrays by use of the PCS technique.

The particular devices used in this study are standard cm-bars described in section 2.2 with an emission wavelength of 808 nm, consisting of 25 single emitters. Thus, again, a uniaxial compressive packaging-induced strain along the u-axis is considered to be present in the waveguide of the bars. These devices experience operation in standard temperature-stabilized (T = 20°C) industrial aging stages with constant current aging at 80 A. Typical output powers for this type of devices are 75 W, and the average power degradation rate amounts to -(11 ± 6) mW/h. For the best devices, with these rates, we find extrapolated lifetimes of more than 6000 h, if a criterion of 80% output power remaining after operation is used. We denote the six individual devices under test as BA-2…7 (see description in Table 2.1).

The PCS measurements were done for all six pristine devices at room temperature (T = (25.00 ± 0.05) °C) with scanning steps of 400 μm along the bar (PC spectrum collected at each emitter). By the analogous procedure for analyzing of PC spectra as previous sections, we obtain the results of optical transition energies in QW at each emitter versus emitter local position for hh1-e1 and lh1-e1 transitions. After 500 h of aging at the above conditions, we reproduce exactly the PC measurements and the analyzing procedures for aged devices (BA-2…7). The results for the device

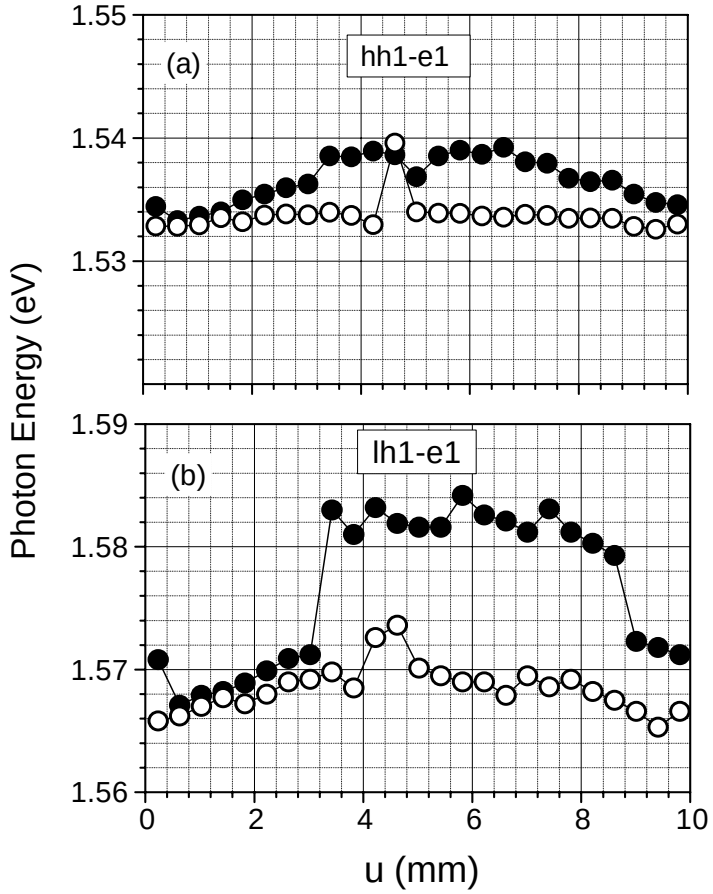

Figure 3.13:

Spectral positions of:
(a) hh1-e1 optical transitions
(b) lh1-e1 optical transitions
versus lateral local positions along the cm-bar denoted BA-6.
Solid circles represent data obtained from the pristine device measured before the aging process, and open circles show the results after 500 h of operation at I = 80 A cw. The measurement was done at 25^0C.

which show the most pronounced changes of all sample, namely device 6, is plotted in Fig. 3.13. Full circles mark data obtained from the pristine device. There is a remarkable shift of the transition energies between the device edge and center before aging. For device BA-6, the photon energy shifts are 3.5 meV and 11 meV for the hh1-e1 and lh1-e1 transitions, respectively. Beside that, we have also observed the corresponding average values for six devices (BA-2…7) amount to (3.2 ± 1.0) meV (hh1-e1) and (10.0 ± 4.0) meV (lh1-e1). Open circles mark data obtained after operation. Clearly, the spectral positions are shifted significantly for both hh1-e1 and lh1-e1 transition. However, there is a peculiarity in the single emitter located at 4.6 mm (emitter number 12). It behaves unusual compared to the neighboring ones. After 500 h of operation, the spectral position for hh1-e1 of this emitter does not change. A careful check of this emitter by EL measurement shows the reduction of emission and existence of dark line defects that are detected by an infrared microscope.

In Fig. 3.14, we show the aging induced energy shift of the hh1-e1 transitions versus local position for devices (BA-2…7). The data points were obtained by subtracting the spectral positions obtained from the fresh devices for corresponding values of the 500 h aging devices. The “bowing” line is a parabolic fit of all data from the six devices. The data from lh1-e1 transitions have been processed in the same way. For the analyzed devices, we find almost no aging-induced energy shift at the device

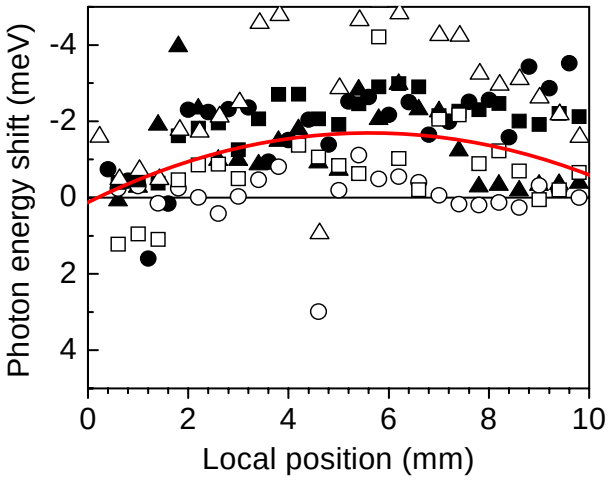

Figure 3.14:

Aging-induced shift of the laser transition vs. local position for all cm-bars investigated after the first 500 h of operation. Full circles, triangles and squares mark data from devices BA-2, BA-3, and BA-4, respectively, whereas the corresponding open symbols indicate the results from bars BA-5, BA-6 and BA-7, respectively. The full line represents a parabolic fit including all data.

edges (0 and 10 mm), whereas at the center, there is a red shift of about -1.5 meV, as we see in Fig. 3.14. The data set from the lh1-e1 shift provides a value of about -5 meV.

The data shown in Fig. 3.15 displays the aging-induced red shift of the hh1-e1 transition versus initial transition energy (before aging) for device BA-3. The almost linear behavior indicates proportionality between the initial packaging induced strain, associated with the spectral position of the optical transition itself, see abscissa, and the amount of aging-induced strain relaxation, associated with the aging-induced red shift, see ordinate of the graph. The slope for device BA-3 obtained by a linear fit on the data, shown in Fig. 3.15, is 0.65, whereas the average slope of linear fits of six devices BA-2…7 is (0.45 ± 0.20).

From the six sets of measurement data described above, we are able to derive explanations for evolution of the behaviors in laser bars during the operation. First, we should address again the physical nature of the observed energetic shifts from edge to center in the pristine devices. As discussions in the preceding section, the bow-like shape of the data, see Figs. 3.13 (a) and (b), is caused by compressive packaging-induced strain (typical behavior of In-packaged bars on copper

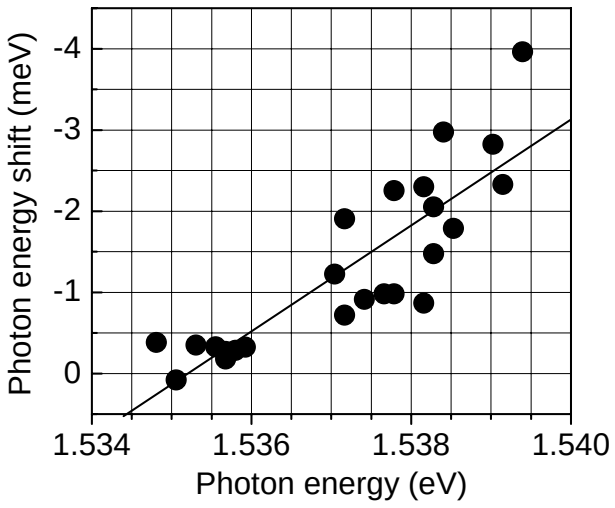

Figure 3.15: Aging-induced red shift of the hh1-e1 lasing transition versus initial transition energy for device BA-3. The solid line represents a linear fit to the data.

heatsinks) and the fact that the edge to center energy shift in the hh-related transition is one third of the lh-related energy shift is again indicative of the uniaxial packaging-induced strain along the <110> direction (value between 0.16 - 0.37); see section 1.2.3.

Now, we consider the operation-induced evolution of the data. Almost all of the available data of hh1-e1 transitions after aging (see Fig. 3.14) indicate red shifts of the photon energies. These shifts are again about one third of the corresponding lh1-e1 related ones. Therefore, one can say that a reduction of the initial packaging-induced strain does not influence its symmetry. In this case the uniaxial strain symmetry along <110> direction was conserved. This conclusion is confirmed by the fact that, we observed proportionality between the initial photon shift, which is packaging-induced, and the aging-induced red shift. This proportionality is visible in Fig. 3.14. However, we should note that e.g. band gap renormalization (related to modified carrier concentration) could have interfered. Therefore, an alternative explanation for aging-induced infrared shifts is band-gap renormalization due to defect creation, as has been observed earlier for comparable laser structures which were exposed to a heavy mechanical load [127]. The defect-induced and band-gap renormalization-related effect, discussed in this earlier study, however, is expected to shift the hh1-e1 and lh1-e1 transitions almost equally. This is obviously not the case here.

Based on the energy shift results, we therefore consider the observed red shifts a clear signature of the reduction of compressive packaging-induced strain. By using the strain sensitivities (coefficients), in the Table 1.3, we find the maximum packaging-induced strain at the center of the pristine devices. Using of the average edge-to-center energy shifts of (3.2 ± 1.0) meV and (10 ± 4) meV for the hh- and lh-related transitions, respectively, and corresponding coefficients from Table 1.3, i.e., (-2.12) for hh1-e1 and (-5.69) for lh1-e1, we find compressive strain values at the device center of -0.151% and -0.176% from the hh- and lh-related energy shifts, respectively. These results are remarkably consistent. The initial energy shifts of hh- and lh-related transitions are reduced, after operation, by 1.5 meV and 5 meV, respectively. Based on the conclusion that the strain symmetries do not change during operation, we use the same coefficient as used for the pristine devices and find strain reductions of -0.071% and -0.088% from the hh- and lh-related transitions, respectively. Given that hh- and lh-related data should provide the same strain value, the pristine devices are, on average, compressed at the center by about -0.16%. Due to device operation this initial strain value is reduced by -0.08 %. Thus the average of the operation-induced strain reduction amounts to about 50% of the initial value. Coincidentally, the observed averaged slopes of (0.45 ± 0.20) on the photon energy shift versus photon energy graph, see Fig. 3.15 indicate a strain reduction of about 50%.

A specific feature of device BA-6 is the peak at 4.6 mm on the device (emitter number 12), appearing after aging process, as seen in Fig. 3.13 (a) and (b). For both hh1-e1 and lh1-e1 related transitions the peak is about + 4 meV above the background given by the neighbor emitters. This localized blue shift is uniform for both transitions, and thus most likely indicates a hydrostatic compression at this particular emitter. Based on the results in section 1.2.3, a sensitivity ratio lh/hh ≈ 1 is expected for hydrostatic compression. The hydrostatic compression is expected as a result of the generation of randomly oriented point defects. By using the appropriate strain sensitivity from Table 1.4, for hydrostatic strain (-23.84 eV for hh1-1e or -23.69 eV for lh1-e1), we find a local hydrostatic lattice compression of about -0.017%. This particular emitter shows after-operation dark line defects. This finding is consistent with the results on strain.

Summarizing, we have studied strain relaxation in six HPDL cm-bars, during high-power device operation. We show that these devices are initially compressively strained, primarily along the <110> direction, with the strain maximum at the center of the device. The maximum compression is about -0.16% (i.e, is almost of maximum packaging induced strain for In-packaged cm-bars on copper heatsink calculated from Eq. 3.1), whereas at the device edges almost no packaging-induced strain is detectable. After 500 h of cw operation at I = 80A the strain maximum is reduced by about 50% without any modification of strain symmetry, whereas essentially no change is observed at the device edges. In terms of actual device parameters, these results mean that for a pristine cm-bar about 30% of the typical total emission linewidth of (2.7 ± 0.4) nm is caused by packaging induced strain. Device operation substantially reduces this fraction. The observed operation-induced red shift of the hh1-e1 transition of about -1.5 meV (-0.8 nm) agrees well with the observed -(0.52 ± 0.15) nm emission wavelength shift for the entire cm-bar. Furthermore, we have observed the creation of a localized compressive strain field in a single emitter. A hydrostatic compression of about -0.017% was observed, despite the relaxation of the uniaxial compression in the particular single emitter's neighbors. We are confident that this particular example of strain analysis illustrates a significant methodology. By carrying out an analysis of more than one optical transition in a QW sample, one is able to gather information about absolute strain values and to obtain at least a partial description of the overall strain symmetry.

3.4. Strain fields in quantum well in vicinity of grooves in semiconductor structures

Semiconductor structures and devices often make use of grooves that are created by etching, micromachining or laser ablation [128-130]. In HPDL arrays, for

example, these grooves serve to decouple optically and electrically the individual laser stripes and to suppress side modes [98]. The behavior of strain in HPDL bars involving grooves, especially in the vicinity of these grooves, has not been analyzed in detail before. In this section, we will present a survey on the strain fields in these regions of HPDL bars.

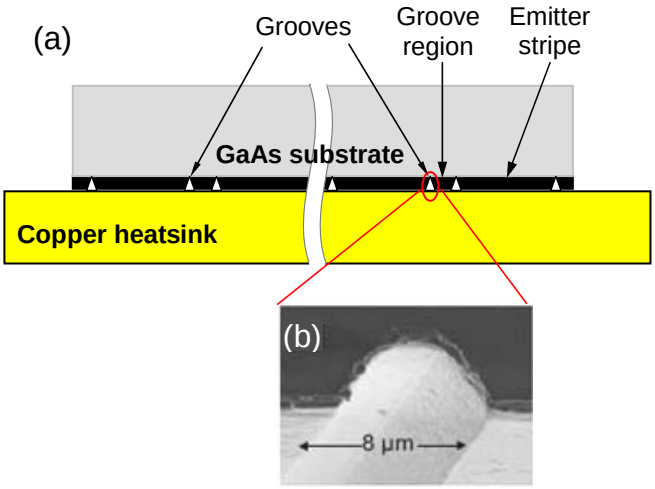

Figure 3.16: (a) Schematic diagram of front facet of a HPDL cm-bar; (b) shows a scanning electron microscope image of one single groove.

Fig. 3.16 (a) shows front facet schematic diagram of the investigated HPDL cm-bar, namely device BA-8. The device is a regular In-package cm-bar as described in section 2.2. The grooves which separate the emitter are situated on both sides of the emitter stripe and are etched through most of the 4.5 µm thick epitaxial layer sequence. Thus, in the cm-bar that consists of 25 emitters, 50 grooves are situated parallel to the <110> direction along the laser axis. Grooves at neighboring single emitters are separated by about 90 µm. For convenience in discussion, this area between two grooves is called "groove region". Fig. 3.16 (b) shows a scanning electron microscope image of one single groove.

Basically, the externally-induced strain distribution in the active region, which is shaded black in Fig. 3.16 (a), along the <110> direction (u-axis) of the device is described in Fig. 3.4 (section 3.2) with an assumption of uniaxial strain (Ref. [58]). However, this strain distribution that is determined by thermo-mechanical FEM was calculated without regard to the influence of the grooves. In practice, the presence of the grooves modifies the strain distribution described in Fig. 3.4. To observe the modification of strain distribution, we employ two spectroscopic techniques, namely µPC and µPL. PC measurements were done in the high resolution scan FT PC setup. The high resolution PC spectra were collected at each scan point with a spatial step width of ~ 26 µm. Totally about 400 points along cm-bar were measured. The µPL employs the setup described in section 2.1.4. It achieves a much higher spatial resolution of about 1 µm. All measurements were done at stabilized ambient temperature $T = (25.00 \pm 0.05)$ °C.

The µPC data of the spectral positions of the hh1-e1 and lh1-e1 transitions along a cm-bar are shown in Fig. 3.17 (a) and (b), respectively. We use grid lines that mark the centers of the groove region, which separates the 25 emitters inside the bar.

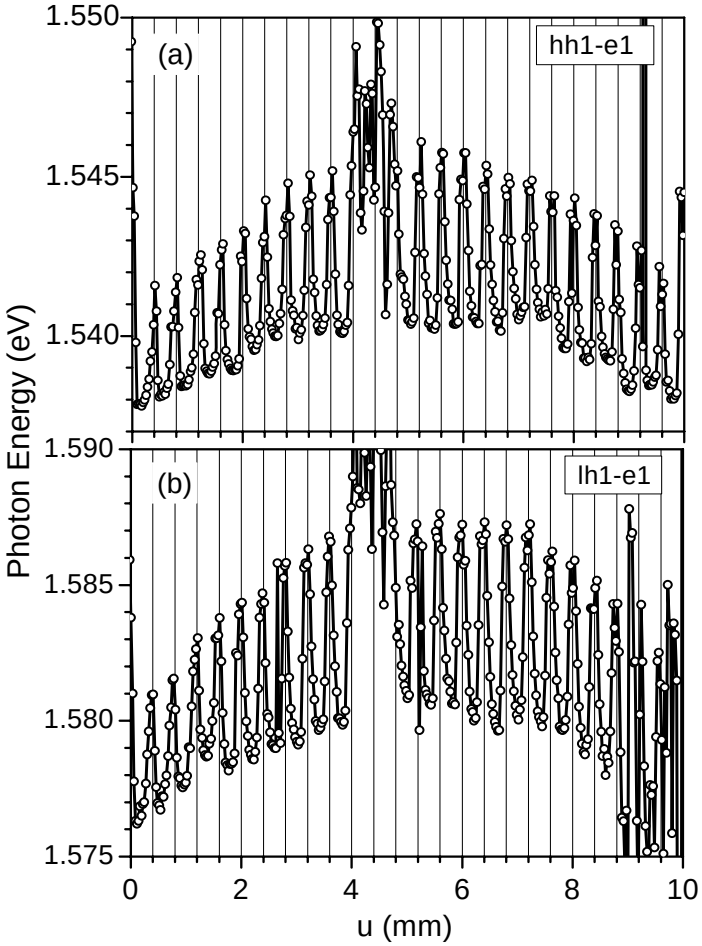

Figure 3.17:

Spectral positions of:

(a) hh1-e1 transitions

(b) lh1-e1transitions

along the u-axis of the 808 nm HPDL cm-bar BA-8. The grid is chosen based on the splitting of the cm-bar into single-emitters. The results extracted from 400 µPC spectra measured along the bar with spatial step of 26 µm in the FT PC setup.

There are three effects that are pronounced in Figs. 3.17 (a) and (b). First there is the moderate blue shift of the spectral positions at the centers of emitter towards the bar center for both hh1-e1 and lh1-e1 transitions. This corresponds to the regular behavior of packaging-induced strain effect occurring in In-packaged HPDL bar on copper heatsinks. The second is a substantially stronger blue shift of the spectral position for both hh1-e1 and lh1-e1 transitions at the groove region. This blue shift reaches a local maximum at the grid lines (midpoints of groove region). This phenomenon is only observed in µPCS measurements. The third significant effect, we consider the stronger shift of lh1-e1 transition compared to hh1-e1 one. The unusual behaviors at emitters number 11 (u = 4.0 - 4.4 mm), number 24 and 25 (u = 9.2 - 10 mm) are caused by the following reasons independently or coherently: contamination of emitters or grooves; defective emitters or grooves.

In order to understand the phenomena observed at the groove area in our µPCS results, we compare them with µPL data. The experiment uses the excitation wavelength of 514 nm and was restricted to two ‘single-emitters’ of the cm-bar. Three measurements were done. First we collect the µPL signal by scanning the excitation beam along the active region of the selected emitters. The PL-peak-positions extracted from these µPL-scans were plotted in Fig. 3.18 (b). After that, a second scan was

performed at a height of 5 µm above the active region. The result of this measurement is presented in Fig. 3.18 (c). Finally, a measurement performed at center of substrate (50 µm above the active region) has been done. In this scan, the PL peak position across the GaAs substrate is a flat line only. Therefore, we do not show this result here. Fig. 3.18 (a) gives the corresponding µPCS data, which are extracted from the QW. In the QW µPL-scan, Fig. 3.18 (b), we can actually see the localized spikes caused by the grooves, which are marked by the arrows. These spikes have not been

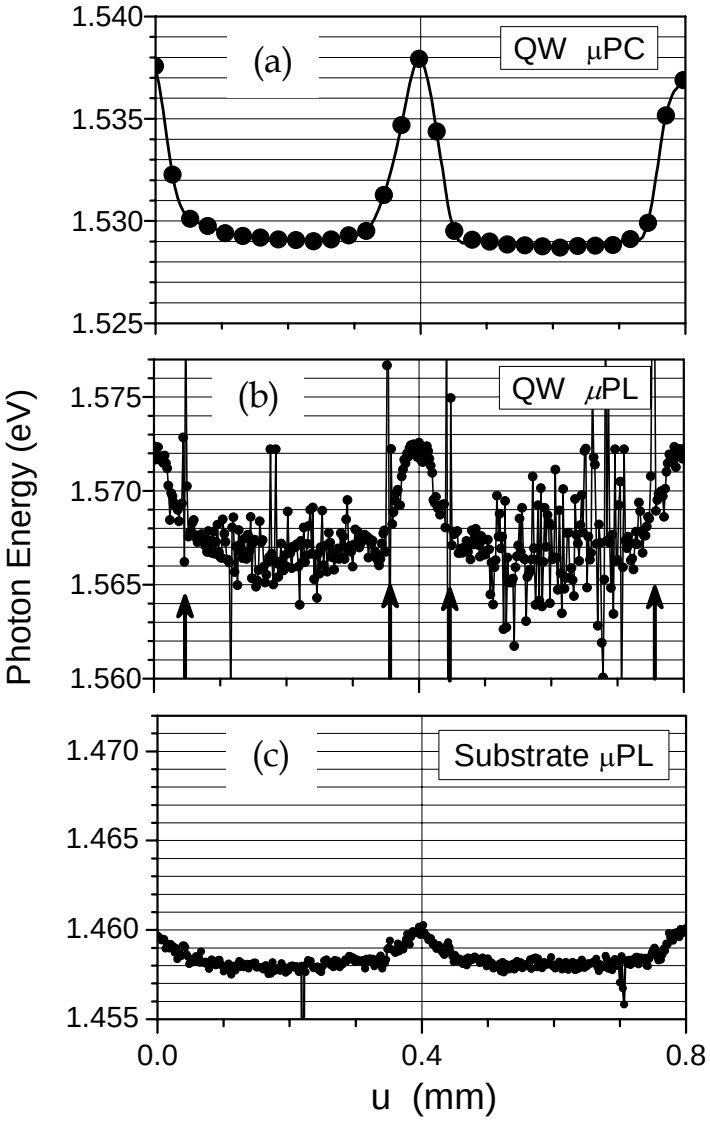

Figure 3.18:

µPCS (a) and µPL, (b) and (c) data versus local position across two 'single-emitters' of the HPDL array BA-8: Figs. (a) and (b) show data, obtained from the QW, which is in the central part of the active region. The arrows in (b) mark the positions of the grooves that are responsible for the creation of the strain field between them. Scan (c) shows the spectral PL peak position within the GaAs substrate at about w = 5 µm above the optically active region.

observed in QW µPCS data of Fig. 3.18 (a). We would like to address that the absence of the spikes in the µPCS result is caused by the lower spatial resolution of the µPCS technique. The dimensions of the grooves are 8 µm-wide and 4.5 µm-deep. Thus an excitation spot size of 30 µm in µPC setup provides not enough spatial resolution to detect these small grooves. The spikes observed in µPL, which are caused by the grooves disappear when the scan is taken deeper in the substrate; see Fig. 3.18 (c). However, in this substrate µPL scan, we can clearly see a remaining blue shift at the

groove region. This blue shift vanishes when the µPL scan is performed at the center of substrate, i.e., 50 µm above active region. All results provided by µPCS and µPL

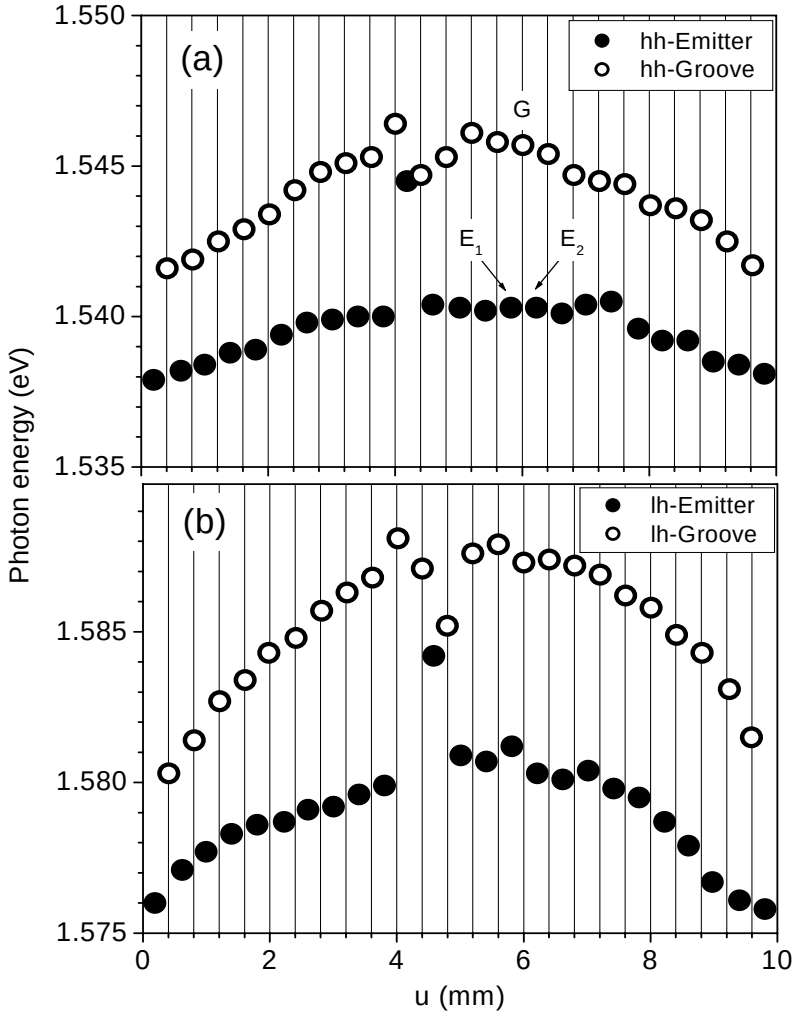

Figure 3.19:

Spectral position of hh1-e1 transitions (a) and lh1-e1 transitions (b) represent for centers of emitters (solid circles) and centers of the groove regions (open circles).

The data are extracted from µPC results that are plotted in Fig. 3.17 at the corresponding local positions.

confirm the existence of local strain fields in the "groove region" (or unmetallized area between two emitter stripe). Qualitatively, this strain field is enhanced in vicinity of grooves and reaches a maximum at the center of the groove regions but it relaxes to zero toward center of the substrate.

Now, we discuss details on the strain field in the groove regions based on measured data. First we start with the quantification of the packaging-induced strain generated in the HPDL bar. Figure 3.19 re-plots the spectral positions versus local positions of hh1-e1 transition, Fig. 3.19 (a), and lh1-e1 transitions, Fig. 3.19 (b), for both emitter centers (solid circles) and midpoints of groove regions (open circles). In Figs. 3.19 (a) and (b), we found the maximum blue shifts are about 2.1 meV and 5.6 meV for hh1-e1 and lh1-e1 transition of center emitter, respectively (see solid circles data) that are caused by uniaxial compressive packaging-induced strain as discussed in the preceding sections for this type of laser bar. The uniaxial symmetry of the strain is confirmed by the ratios between the shift of hh1-e1 transition and lh1-e1 transition of

about (0.37 ± 0.02) [see section 1.2.3]. Therefore, in condition of external uniaxial strain with a known intrinsic strain of -0.45% (for this QW structure in the bar), we can take strain sensitivities for hh1-e1 and lh1-e1 transitions, namely -2.12 eV and -5.69, respectively [Table 1.3]. Thus, we find this cm-bar to show a deformation difference between the edges and center of about -0.1 %, i.e. 2.1 meV/(-2.12 eV) ≈ -0.1% and 5.6 meV/(-5.69) eV ≈ -0.1%.

Obviously, the packaging-induced strain with a maximum of -0.1% also influences the strain field in the groove region. Alternatively, we can state that the groove region suffers both packaging-induced strain and a "groove" local strain field that acts independently of the packaging-induced strain. At present, we have no information about the strain configuration of the local strain field at the grooves. Analyzing the data in Fig. 3.19 could provide suggestions on strain symmetry of this strain field. First, we define the modulation M of the groove region as the difference between the spectral positions at the midpoint of the groove region (e.g. G in Fig.3.19.a) and the extrapolation value between the spectral positions of two neighboring emitter centers (e.g. E_1 and E_2 in Fig. 3.19.a). From these extrapolation values the spectral position of edge emitter providing bowing values are subtracted. The modulation is assigned as representative for the "groove" local strain field at the grooves, while the bowing values quantify the uniaxial packaging-induced strain along the bar. Fig. 3.20 plots the modulations versus bowing for both hh1-e1 (solid circles) and lh1-e1 (open circles) transitions (data calculated from Fig. 3.19). The modulation is stronger for lh1-e1 than for hh1-e1 transitions. The slope of two fitting lines of the data are (0.58 ± 0.05) and (0.62 ± 0.05) and the intercepts are (3.50 ± 0.10) meV and (3.65 ± 0.20) meV for hh1-e1 and lh1-e1, respectively. The intercepts for hh1-e1 and lh1-e1 show the values at the edge, where no uniaxial packaging strain is expected to exist. There the ratio is approximately 1. This fact suggests assuming the existence of hydrostatic strain at grooves at the edge of the emitters. If this assumption is confirmed, the observed strain field at groove region will likely be compressive hydrostatic with compressive strain above -0.015%,

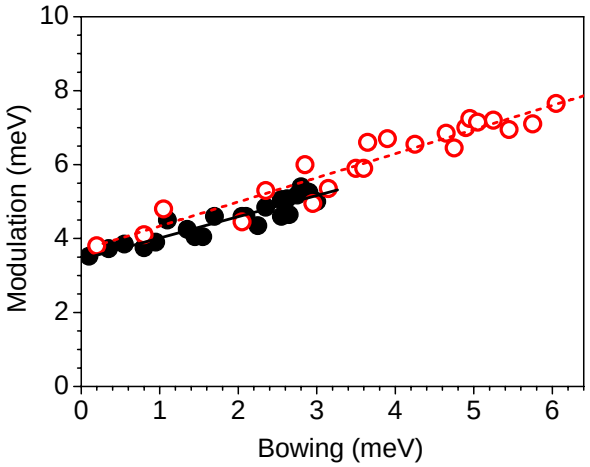

Figure 3.20: The modulation versus bowing. The solid and open circles are hh1-e1 data and lh1-e1 data respectively. The solid and the dashed lines are fits of hh-related data and lh-related data.

i.e., 3.5 meV/(-23.84 eV) ≈ -0.015% and 3.65 meV/(-23.69) eV ≈ -0.015% [strain sensitivities are taken from Table 1.3 for hydrostatic compressive strain]. We should note that this statement is only true with the assumption of independently acting of packaging-induced strain and local strain field of groove region.

We now analyze another aspect of the local strain field in groove region, namely the "overall strain". In Fig. 3.21, we plot the ratios of the spectral position shifts between hh1-e1 and lh1-e1 transitions at each groove as function of groove position along the cm-bar (the reference is the spectral position of edge emitter). The data for the calculation are also provided by Fig. 3.19. While the change in transition energies increases along the bar in moving along the u-axis toward the center of the bar, the ratio of the two transitions at the groove region is essentially constant, with a value of (0.69 ± 0.08). This ratio (if we compare it to the strain sensitivities) is consistent with a strain configuration that is biaxially symmetric in the plane of the QW [52]. Therefore, the "overall strain" at the grooves is rather a biaxial configuration. However, based on this "overall strain" behavior, we can not claim with absolute certainty that whether the strain field at groove is also biaxially symmetric in the plane of the QW. Although it is not possible to state about the strain configuration of the local strain fields at the groove regions, one can conclude that this strain contribution is likely to have a higher symmetry than the uniaxial strain arising due to packaging induced stress applied along the <110> direction.

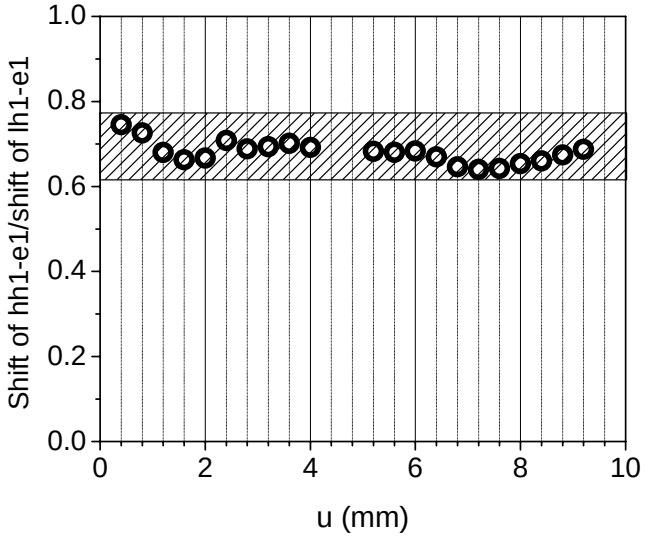

Figure 3.21: Ratio of the hh1-e1 to lh1-e1 transition energy shifts at grooves, as a function of position along the cm-bar BA-8.

In the section, we studied a local strain field in QWs in the vicinity of grooves in semiconductor structures. Two spectroscopic techniques, μPCS and μPL, are combined to detect the strong spatial modulation of the QW-band structure in the "regions between the grooves". These two experimental approaches provide consistent and complementary results. The strain has constant strain symmetry along the length of the device. Analysis of the strain sensitivities of the two lowest interband transition energies, namely hh1-e1 and lh1-e1, implies that this strain contribution has a symmetry that is higher than arises due to packaging-induced stress. While this

additional strain is seen to exist in the absence of an externally-applied stress, such as arises due to packaging, the presence of an external stress significantly impacts this additional strain contribution, influencing its symmetry. The observation of this additional strain contribution is of substantial interest for device physics. If device designs involve grooves, which create or modify (even both) intrinsic and externally-induced strain fields, one has to take care that additional processing, handling or packaging do result in strain contributions that eventually lead to device damage.

3.5. Comparison of packaging-induced stress in the substrate and the active layer of high brightness diode lasers

In the preceding sections, we discussed about the strain behavior in HPDL arrays based on broad-area laser cm-bars. However, strain analysis also is needed for novel high brightness tapered HPDL structures. In this section, we will discuss some results obtained from a strain analysis of high brightness tapered HPDL bars.

The tapered HPDL bars, hereafter called “tapered bars”, as described in section 2.2., consist of 20 identical 500 μm width-emitters. The tapered bars are 10 mm wide and 2.5 mm in resonator length and were packaged on a copper heatsink with indium. The structure is based on 7 nm wide single QWs of InGaAs emitting at 980 nm with an optical output power of 40 W. Three devices under test are denoted TB1-1, TB1-2, and TB1-3. PCS, μPL and μPCS techniques have been used for strain measurements.

Theoretical calculation of strain sensitivities was not available for the InGaAs QW structures. Therefore, to achieve strain values in tapered bars from the shifts of spectral positions, we have to estimate firstly the strain sensitivities from the experimental results obtained from these bars. For this purpose, we use the samples under test (TB1-1…3) themselves as gauge.

The PCS measurements performed at emitter centers of the devices TB1-1…3 and μPL scans were done at 10 μm above active area (inside substrate) along these devices. Analysis of PCS spectra and μPL data provide spectral positions of QW and waveguide transitions (in PCS) and emission spectral position (in μPL) versus local positions. These results display typical “bow-like” shapes as for compressively packaged devices. From this result, we now experimentally determine strain sensitivities. The assumption of vanishing strain at the edge is again applied for this case. We plot the spectral shifts of QW (hh1-e1) and waveguide transitions in PCS versus spectral shifts of μPL for each emitter in three tapered bars. In Fig. 3.22, we show the results obtained from device TB1-1 with both hh1-e1 and waveguide data (solid circles and triangles, respectively). After that, linear fits were made for the two sets of data. The slopes of these fitting lines show coefficients that link μPL data and PCS data (hh1-e1 and waveguide). These coefficients allow a cross-calculation

between the µPL data and PCS data. The procedure has been repeated to find similar coefficients for device TB1-2 and TB1-3. Results are shown in Table 3.2 with average values for the three devices (TB1-1…3) in the last row.

Now, the coefficients are compared to data obtained for 808 nm-emitting devices, which have been investigated before [131]. For these devices the coefficient of the hh1-e1 transition versus the µPL-transition amounts to 2.1, i.e., a factor of 4 higher than the average of 0.51 that is obtained from Table 3.2. With the 808 nm emitting devices, the strain sensitivities have been also theoretically determined [60,132]. Taking into account the theoretical value of -2.12 eV for the hh1-e1 transition in the 808nm emitting devices with compressive built-in and packaging-induced strain, we find a value of about -1 eV for the µPL strain sensitivity. This allows estimating strain sensitivities for the relevant PCS-transitions of these 980 nm emitting devices, -0.51 eV for hh1-e1 and -1.17 eV for the waveguide. Fig. 3.23 shows a comparison of the distributions of the packaging-induced strain along the <110> direction measured at QW, waveguide and substrate of the tapered bar TB1-1. These data were converted by using the estimated strain

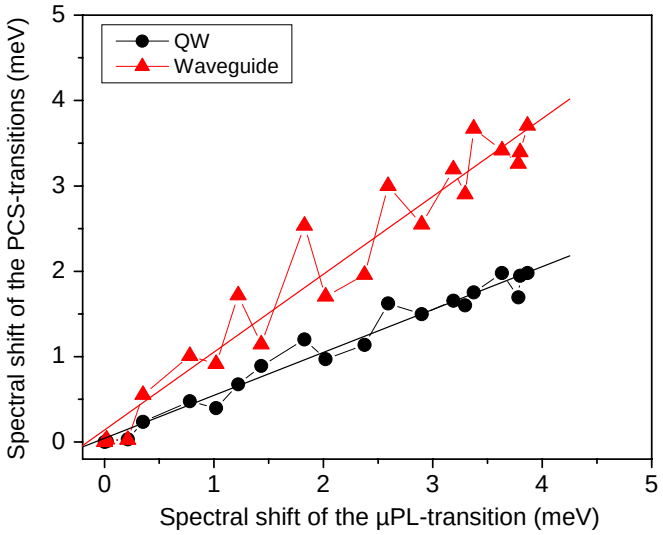

Figure 3.22: Spectral shifts of QW and waveguide transitions versus corresponding µPL data. Solid circles and triangles represent QW and waveguide data from PC, respectively. The lines are linear fits to the data.

Table 3.2: Coefficients of PC spectral shifts versus µPL spectral shifts

Bar name	***hh1-e1***	***waveguide***
TB1-1	0.52	0.92
TB1-2	0.38	1.28
TB1-3	0.63	1.31
average	***0.51***	***1.17***

sensitivities. The absolute strain values should not be compared here, because the strain sensitivities given in the Table 3.2 have been derived with assuming that there is no vertical strain gradient. For devices TB1-2 and TB1-3, we found analogous behaviors. Based on all these results, we can state:

- The shapes of the 'bulk-data', namely µPL and waveguide information from PCS agree remarkably.
- The shape of the strain distribution derived from the QW shows a systematic deviation (see Fig 3.23). One should remember that the QW is embedded into the waveguide and thus definitely experiences the same amount of packaging-induced strain.

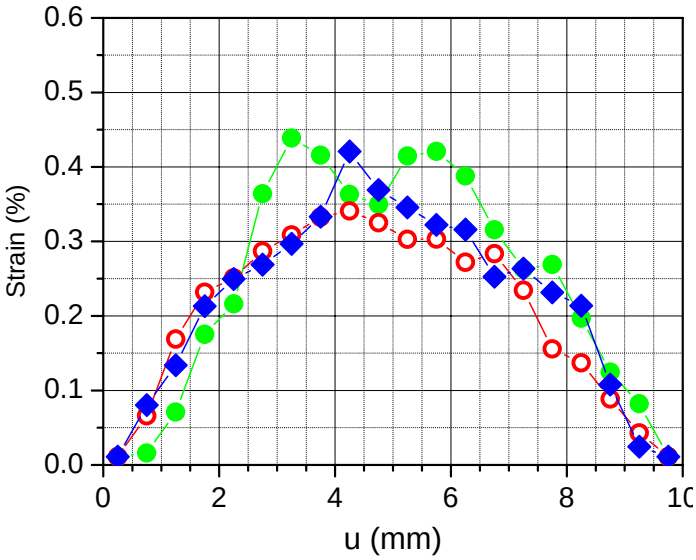

Figure 3.23:

Strain profiles of the tapered laser TB1-1: the data is extracted from PCS, micro-PL measurements by combining them with strain sensitivities as determined from the slopes in Table 3.2.
The solid circles represent QW results from PCS; the diamonds are PCS waveguide data; and open circles show micro PL results.

Fig. 3.24 represents a combination of µPL data of device TB1-2 measured at 10 µm and 50 µm above active region for emitters 8-11 (from the position of 3.5 mm to position of 5.5 mm), i.e. at a local position where the bar is mostly affected by packaging-induced strain. Obviously there is absolutely no shift of the overall µPL peak position at 50 µm above active region against 10 µm one. In both cases, the average is at about 1.463 - 1.464 eV. This indicates that there is no vertical relaxation of packaging-induced strain across the substrate. This result and the agreement between strain in active region and waveguide shown before (similar to result in Fig. 3.23) provide us with the information that there is no change of the strain from the active region to the center of substrate. Beside this statement, which is essential in our line of arguments, we should address the spikes observed in this Figure. The smaller blue-shifted peaks at the grid lines, which are seen in the solid-circle data, are signatures of the grooves that we already discussed in the previous section. The two pronounced narrow peaks at u= 4.3 mm and 5.1 mm are caused by defects. These

defects are indicative of "V-shape" defects as presented in Ref. [93]. They are associated to crystalline imperfection of the substrate. The blue shift observed at these defects in the µPL data in Fig 3.24, is a consequence of local stress fields generated in the substrate. Thus the signature of these defects was not observed in the µPCS results. Thus, we assume that they remain in the substrate but yet do not penetrate into the active region of the tapered bar, at this stage.

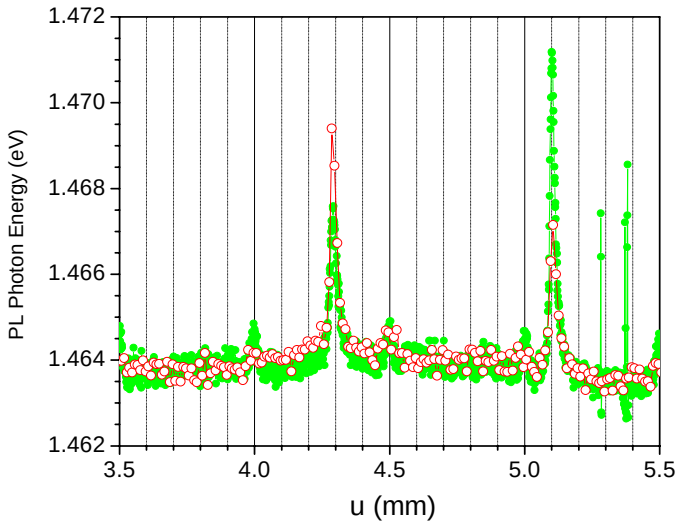

Figure 3.24: Micro-PL measured along u-axis at 10 µm (solid circles) and 50 µm (open circles) above active region of laser for device TB1-2.

Finally, we compare the µPL-data from emitter number 8 to 11 with µPCS-data. An overview is shown in Fig. 3.25. The grid lines mark the borders of the emitters, where grooves are etched. Obviously, these grooves introduce a substantial strain into the whole structure. Thus, their impact is clearly seen even 10 µm away from the active region (see µPL data as solid circles at the grid lines). The impact to the transitions in the active region is even clearer as one can see from the µPCS data with the peaks at the grid lines in both QW and waveguide data. Again 'bulk-like' waveguide and QW show a different behavior. We should mention that a discussion of these differences (see also our discussion on Fig. 3.23) requires knowledge about the strain symmetry, which is not completely clear at the grooves of the bars. In addition, the waveguide µPCS-data indicates the position of the emitter-metallization (see areas marked with dotted rectangular in Fig. 3.25). This metallization introduces additional strain into the active region, which is already relaxed 10 µm away from it. Therefore, we do not see their impact in µPL lines performed at 10 µm and 50 µm above active region of the tapered bar.

Now, we summarize the primary results of the strain measurement on tapered bars. First, we presented a comparison of packaging-induced stress in substrate and active layer of high-brightness bars made by the application of several optical techniques such as µPL, PCS and µPCS. Second, we find for the bar center no strain relaxation from the active region towards center of the substrate. Third, we made a cross-calibration of PL and PCS-data. Using this we experimentally estimate the strain sensitivities for the 980 nm emitting tapered laser structure to 0.51 eV for the hh1-e1

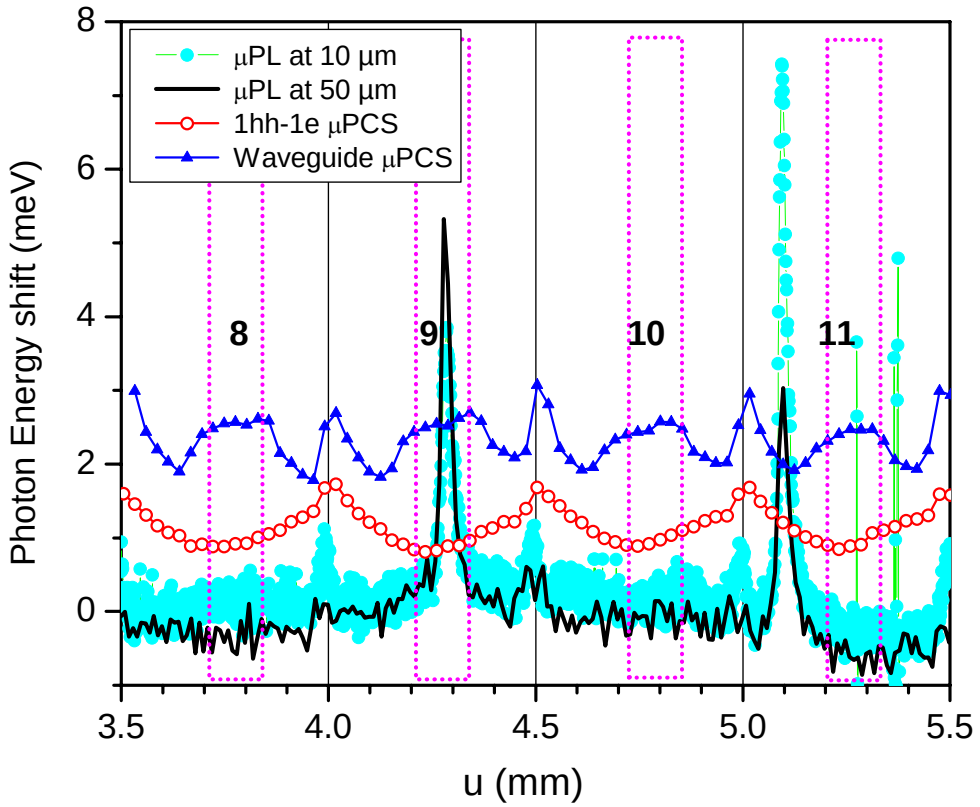

Figure 3.25: Comparison of μPL and μPCS results at central emitters (number 8 and 11) of the high brightness bar (device TB1-2): μPL-data are measured at 10 μm (solid circles) and 50 μm (solid line) above active region; μPCS-data from the hh1-e1-QW-transition (open circles) and from the ´´bulk-like´´ waveguide (triangle) are added. The absolute values of the photon energies are shifted in order to achieve a clear presentation.

transition and 1.17 eV for the waveguide. Finally, the defects in the substrate of the tapered bar were found to be likely of the "V-shape" type. However, some peculiarities of QW strain behavior is still not well understood because of a lack of knowledge about strain symmetry in these complex devices. Therefore, some further work such as calculation theoretically of strain sensitivities, measurement of aged tapered laser bars must be done in order to achieve complete clarification.

Chapter 4.

Thermal tuning properties of high power diode lasers

The thermal tuning properties are important parameters of diode lasers. For HPDLs, the thermal emission wavelength tuning effect represents a key issue because device operation is accompanied by device heating. While some applications do not call for an accurate wavelength homogeneity and stability of the HPDL arrays, some others, in particular, those involving resonant pumping [133,134], require detailed knowledge and control of these parameters. The thermal tuning of the laser transitions is known for a given epitaxial design of laser structure and is usually provided by the manufacturers. The next step towards a device, namely device packaging, might subsequently modify these rates [135-137]. Therefore it is important to quantify this additional tuning rate contribution and to take it into account when relevant for a particular application. The thermal tuning rates for each single emitter of a bar can be determined, e.g., by analysis of thermal shifts of the laser emission with an imaging spectrometer [135]. However, effects related to the lasing effect itself may substantially influence the measurements. Therefore, an alternative method, namely PCS that is free of any thermal load and negligible influence from the electron concentration in the QW is used. In this chapter, we discuss the thermal tuning properties in HPDL arrays packaged on different types of heatsinks, namely standard heatsink (e.g., copper) and expansion matched heatsink (e.g., CuW).

4.1. Thermal tuning rate of single emitters in high power diode laser bars

We start the investigation of thermal tuning properties with determining the thermal tuning rates in HPDL arrays. The devices under test are standard 808 nm

emitting HPDL cm-bars with output power of 50 W. These bars consist of nineteen 500 µm wide (device BC-2) or twenty-five 400 µm wide (device BA-9) identical emitters. In this study, we select three representative bars from two packaging technologies. First, devices BC-2 and BA-9 were packaged 'epi-side-down' on passively cooled standard copper heatsinks by using indium solder. Second, device BB-1 was soldered with gold-tin solder on an expansion-matched Cu-W heatsink. The details of the packaging technology are presented in Ref. [138]. For In-packaged devices (BC-2 and BA-9), the effects due to packaging-induced strain are known from the previous discussions, whereas device BB-1 is expected to be almost free of packaging-induced strain, because the thermal expansion coefficient of the Cu-W heatsink is well matched to the GaAs one (see Table 3.1).

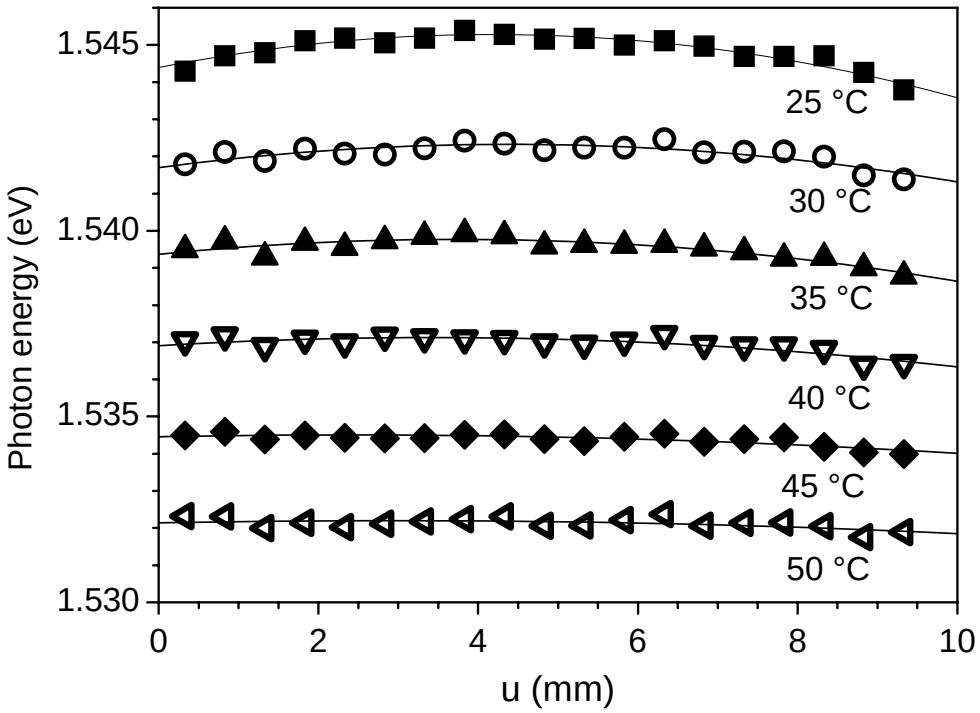

Figure 4.1: Spectral position of the hh1-e1 transitions versus local position along device BC-2 within the 25 - 50°C heatsink-temperature range. The solid curves are parabolic fits of the data sets.

PCS measurements were used to determine the thermal tuning rates of three devices (BC2, BA-9 and BB-1). We performed PCS measurement at the center of each individual emitter within the 25-50 °C heatsink-temperature range. The heatsink temperature was increased with a step of 5 K and stabilized by a Peltier cooler. The PC spectra obtained from the bar were analyzed providing the spectral positions of the energetically lowest optical transitions within the QW, namely the hh1-e1 transitions that correspond to the lasing transitions in this type of structures, along the bar at

different temperatures. The results for device BC-2 are shown in Fig 4.1. The well-known thermal photon energy shift is clearly visible for all three devices. From these raw data, we determined tuning rates for individual emitters of the cm-bars. The thermal tuning rates were obtained by dividing the energy shifts by the temperature difference. These data are plotted in Fig. 4.2 for three devices (BC2, BA-9 and BB-1).

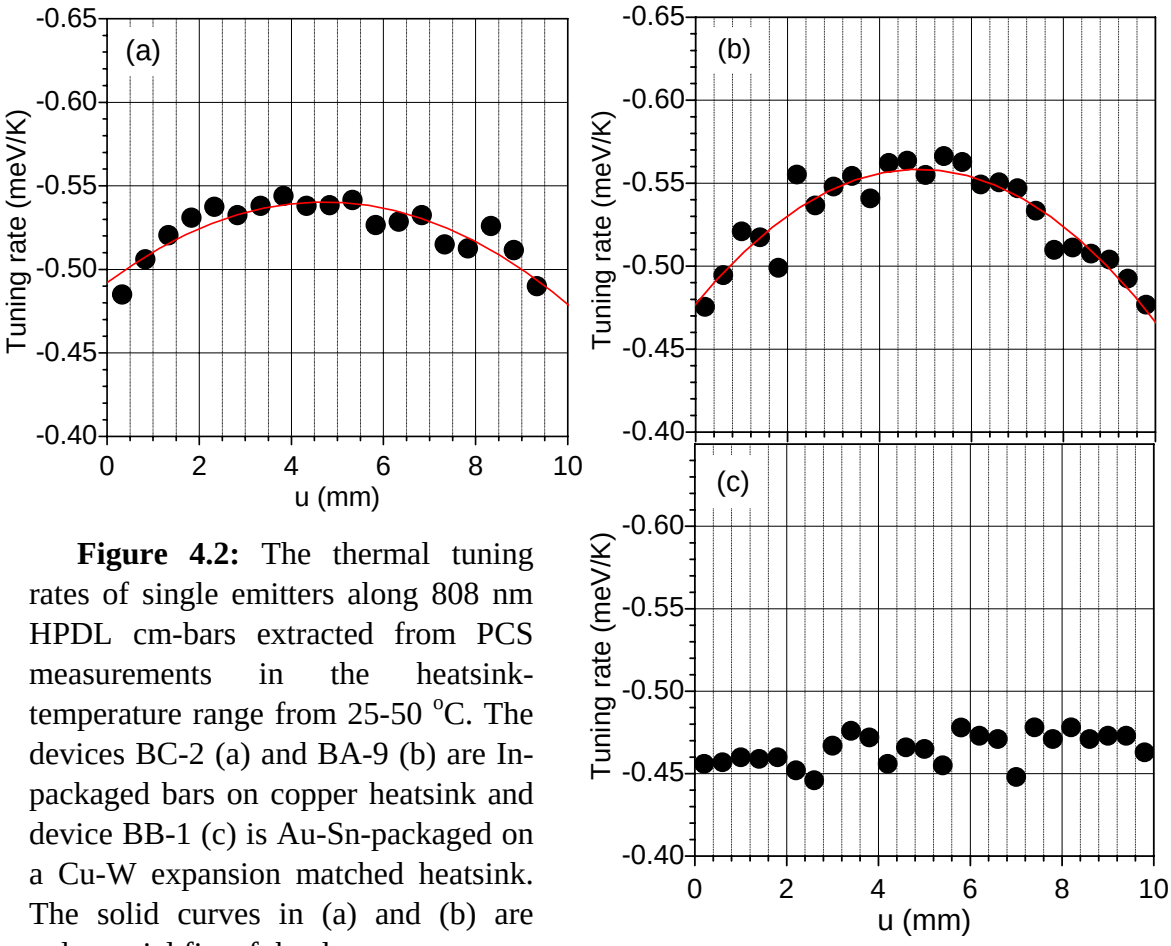

Figure 4.2: The thermal tuning rates of single emitters along 808 nm HPDL cm-bars extracted from PCS measurements in the heatsink-temperature range from 25-50 ^{o}C. The devices BC-2 (a) and BA-9 (b) are In-packaged bars on copper heatsink and device BB-1 (c) is Au-Sn-packaged on a Cu-W expansion matched heatsink. The solid curves in (a) and (b) are polynomial fits of the data sets.

Now, we discuss the comparison of two methods for determination of thermal tuning rate in cm-bars, namely PCS and electroluminescence (EL). The EL data are measured in a setup with a grating spectrometer and a CCD camera [135]. Here the cm-bar is operated at an extremely low current of typically I = 10 mA in order to reduce the contributions due to thermal effects to a minimum. EL spectra from subsequent emitters are measured for two heatsink temperatures (25 and 45 °C). The position of the EL peak is determined by Gaussian fitting (two-peak) around the central part (10 nm) of the spectrum. Fig. 4.3 shows two sets of the thermal tuning rates extracted from PCS and EL data, where full circles represent for PCS – rates and open circle stand for EL – rates. In case of QWs, the spectral position of the spontaneous emission (EL) is determined by three main factors: value of the material bandgap, bandgap renormalization and carrier band filling, whereas the position of

absorption derived from photocurrent measurements is determined by the first two only. Therefore, the observed difference is entirely attributable to carrier band filling effects. Assuming direct momentum-conserving spontaneous optical transitions in a bulk semiconductor, the shift, which is theoretically expected between rates derived from absorption and spontaneous emission, is calculated to be $\frac{1}{2} \times k = 0.0431$ meVK^{-1} where k denotes Boltzmann's constant [see bar in Fig. 4.3]. The expected shift is larger in the case of QWs and increases towards smaller well thicknesses [137]. The higher data spread of the emission data in Fig. 4.3 clearly illustrates the advantage of the use of the photocurrent technique for the determination of thermal tuning rate. PCS potentially provides more accurate values of thermal tuning rates. In turn, the remarkable agreement between the two data sets again justifies the use of PCS for our study of thermal tuning properties of HPDL devices.

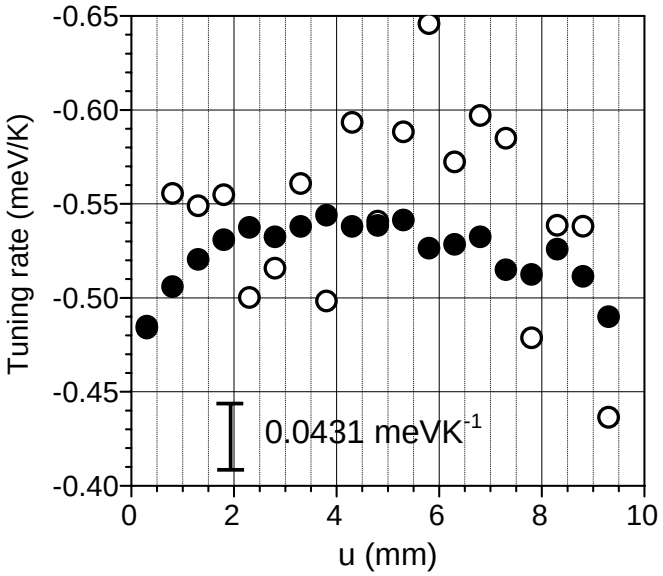

Figure 4.3:

Thermal tuning rates along the cm-bar (device BC-2) are determined by PCS measurement (full circles). Open circles give the rates obtained from emission data, measured at an operation current of I = 10 mA. The bar marks the value of $k/2 = 0.0431$ meVK^{-1} .

4.2. Thermal tuning properties of high power diode laser arrays packaged on standard and expansion matched heatsinks

The preceding section presented results of thermal tuning rates of HPDL cm-bars packaged on standard copper heatsink by In-solder and expansion matched Cu-W heatsink by Au-Sn determined by PCS measurements. Based on these results, in this section, we continue the detailed discussions on thermal tuning properties of both types of the HPDL cm-bars.

By using the PCS technique, the influences of unexpected effects, namely thermal and structural inhomogeneities, to the measurements are excluded because the HPDLs is non-operating and PCS technique involve a "self-focusing" capability. In Fig. 4.1, for device BC-2, we find the shape of the curves to exhibit a thermal

evolution from bowing with high amplitude, cf. Fig. 4.1 top 25 °C, to a flatter curvature (low amplitude), cf. Fig. 4.1 bottom 50 °C. This behavior is also observed for device BA-9 and is typical for In-packaged devices that suffer packaging-induced strain. In Fig. 4.4 (a), we show the quantification of this effect for device BC-2, which shows the bowing, namely the energetic difference between device center and edge as described in previous sections, versus temperature. Between 25 °C and 50°C, we observed a decreasing of the bowing amplitude by a factor of 3. The final result extracted from Fig. 4.1, namely temperature dependent thermal tuning rate, is shown in Fig. 4.4 (b). It decreases towards increasing temperatures, see Fig 4.4. This behavior is related to a relaxation of the compressive packaging-induced strain with increasing temperature.

For device BB-1 packaged on expansion matched Cu-W heatsinks by Au-Sn solder, the data obtained from analysis of PCS measurements do not show any peculiarities. We found that, in the 25 – 50 °C heatsink-temperature range:

- There is no notable temperature dependence of the tuning rate.
- Almost no change of the curvature with increasing of temperature take place in this range.
- The thermal tuning rate shows almost no spatial dependence along the device as clearly demonstrated in Fig. 4.2 (c).

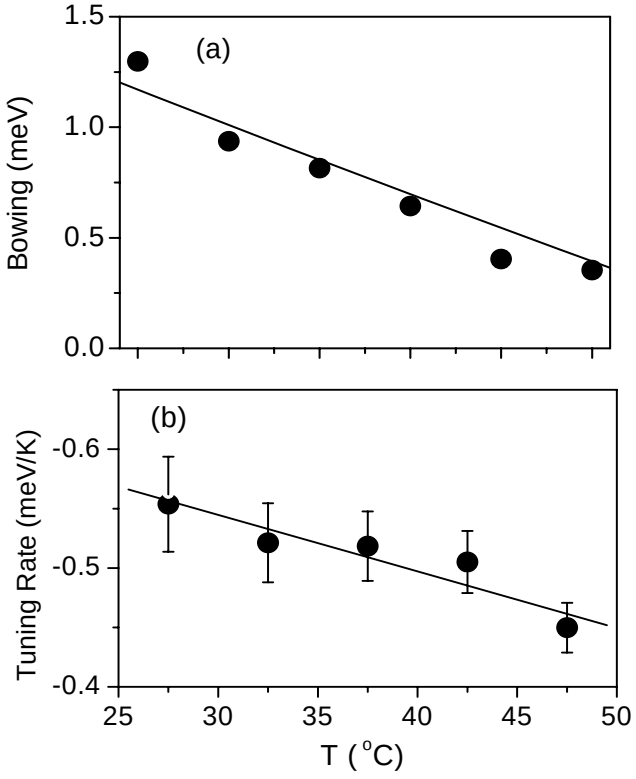

Figure 4.4:

(a) Bowing of the curves shown in Fig. 4.1 (a) for device BC-2 versus temperature. The value of the bowing is determined on the basis of a parabolic fit of the data. The data points are obtained from the fit by subtracting the averaged photon energy at the device edges from the one in center.

(b) Temperature dependence of the thermal tuning rate of device BC-2.

Now, we continue our discussion by quantifying the mechanical deformation of the In-packaged cm-bars, namely device BC-2 and BA-9, that suffer different amounts of packaging-induced strain, during thermal tuning, based on the by-emitter analysis of the individual tuning rate for each single emitter. This approach allows us to separate between purely thermal tuning and mechanical pressure tuning contributions to the observed overall thermal tuning. To quantify the strain amounts in devices BC-2 and BA-9, we should recall again the result found in Ref. [121] that the packaging induced strain in In-packaged cm-bars vanishes towards the bar edges. The bowings for 25 and 50 °C obtained from device BC-2 are about 1.26 and 0.38 meV, respectively. The analogous values for device BA-9 are 3.15 and 1.6 meV. Using the strain sensitivity of -2.12 eV from Table 1.3 (here the uniaxial strain configuration is predominant for both devices), we get absolute strain amounts of the device BC-2 about -0.059 % for 25 °C and -0.018 % for 45 °C along <110> direction. The corresponding values of the device BA-9 are about -0.148 % and -0.075%. Thus, in these examples, about 70 % (device A) and 50 % (device B) of the packaging-induced stress vanishes when the devices are heated up by 25 centigrade only. In other cases, however, one might be faced by excessive local strain gradients created in this way [135].

The observed shape of the curves in Fig 4.2 (a) and (b) is caused by the relaxation of packaging-induced strain along <110> direction as discussed above. With the condition of unstrained edges, the thermal tuning rates at edge emitters, -0.48 $meVK^{-1}$ (device BC-2) and -0.47 $meVK^{-1}$ (device BA-9), are contributions of pure thermal tuning rates. The overall thermal tuning rates (-0.54 $meVK^{-1}$ and 0.56 $meVK^{-1}$) of center emitters of devices BC-2 and BA-9 contain both pure thermal tuning and mechanical pressure tuning (which is caused by relaxation of the packaging-induced strain) contributions. The pressure tuning contributions, therefore, are [-0.54 $meVK^{-1}$ - (-0.48 $meVK^{-1}$)] = -0.06 $meVK^{-1}$ for device BC-2 and -0.09 $meVK^{-1}$ for device BA-9. These pressure tuning rates cause the inhomogeneous wavelength red-shift observed in emission patterns of the cm-bars. Thus, we can state that about 11 % and 16 % of the thermal tuning rates of the central emitters in cm-bars BC-2 and BA-9, respectively, are actually caused by pressure tuning. These pressure tuning rates correspond to a thermal deformation rates of 2.8×10^{-3} % K^{-1} and 4.2×10^{-3} % K^{-1} at center emitters of the cm-bars BC-2 and BA-9.

The results on the pressure contribution to the thermal tuning rates suggest analyzing the mechanical load that cm-bars suffer. In Ref. [135], we show that in typical operation regimes of cm-bars, the temperature in the bar reaches the cw-value within about hundred milliseconds. Therefore, if the cm-bars operate in low-frequency pulse regimes (scale of 0.1 - 10 Hz, cf. Ref. [135]) the center emitter will suffer “pulses” mechanical load (periodically expanding-compressing) of 2.8×10^{-3} % K^{-1} and 4.2×10^{-3} % K^{-1} for the bars BC-2 and BA-9, respectively. Consequently a

temperature rise by 10 K within a pulse, which is a representative number for low-frequency pulsed operation, causes deformations of about 0.028 % and 0.042 % along the bars BC-2 and BA-9 in the <110> direction. In turn, the weaker deformation of the bar at the edges indicates that here the In-solder absorbs the mechanical load. This means that at the edges the Indium gets deformed within each cycle. If this deformation includes plastic contributions, the reliability of the solder joints, particularly at the device edges, might eventually be reduced.

These additional stresses, as well as the accompanied gradients, might promote dislocation motion and eventually affect the device structure and eventually reduce the device reliability. A similar behavior is almost absent in case of Au-Sn packaging technology. Evidence is given by the homogenous spatial thermal tuning rate of device BB-1 as shown in Fig. 4.2 (c). This fact confirms the advantage of Au-Sn packaging technology on Cu-W compared to In-based one on Cu.

We now consider the pure thermal tuning rates of three devices (BC2, BA-9 and BB-1). The total thermal tuning rate of the device BB-1 soldered with Au - Sn on expansion matched Cu-W heatsinks amounts to $-(0.46 \pm 0.01)$ meVK^{-1}, see Fig. 4.2 (c), whereas the rates of device BC-2 and BA-9, which is soldered with In on a Cu heatsink, are about $-(0.48 \pm 0.01)$ meVK^{-1}, see Fig. 4.2 (a) and $-(0.47 \pm 0.01)$ meVK^{-1}, see Fig. 4.2 (b). The quite good agreement between the thermal tuning rates of the three devices allows the conclusion that the genuine thermal tuning rate of the 808 nm emitting AlGaAs HPDL structure is about $-(0.46 \pm 0.01)$ meVK^{-1}.

Now we come to a qualitative discussion of the strain creation scenario for an In-packaged bar by using data in Fig. 4.5. In Fig. 4.5, the full circles represent the mechanical deformation in the center emitter of the bar, assuming that there is no deformation at the edges. This data is obtained from Fig. 4.4 (a) by using the strain sensitivity value of -2.12 from Table 1.3. The solid line is calculated according to equation (3-1), whereas the dashed line represents a model that attempts to include the plastic properties of the In-solder. This result was obtained by Lorenzen in Ref. [136]. We now concentrate on the data (full circles) and the solid line, which is calculated according to equation (3-1), representing the elastic limit. The estimate, which attempts to include the plastic properties of the In-solder (dashed line in Fig. 4.5), is a first step connecting the experimental data and the elastic limit. The plastic deformation behaviour of a material becomes clearer in stress-strain hysteresis loops during mechanical cycling [137]. In the present case, mechanical cycling of the indium solder is initiated by re-heating the package before the measurements. In combination with possible solder hardening, the observed reduction of the compressive strain in the active region in center of the laser bar with increasing temperature is thus justified; see arrow in Fig. 4.5. An important question is how multiple thermal cycles or annealing influence the result. Even the rather long measuring time in our experiment [data sets

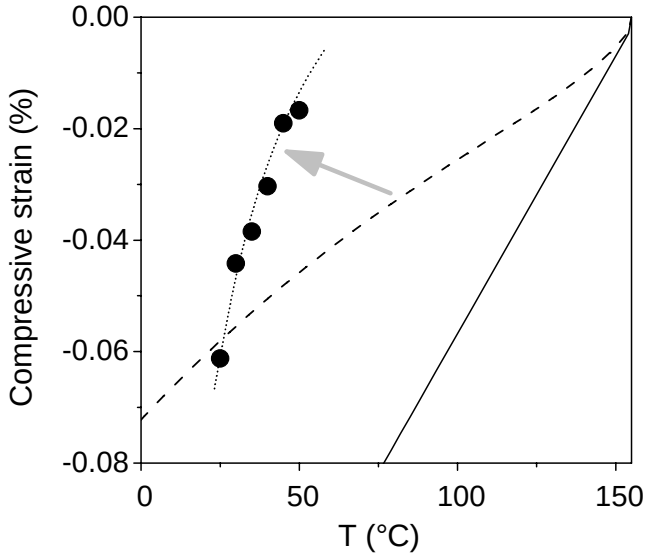

Fig. 4.5:
Strain in center of the bar with respect to the one present at the edges of device BC-2 (full circles). The full line is calculated according to equation (3-1), whereas the calculation represented by the dashed line involves to the plastic properties of the In-solder according to Ref. [136]. The arrow indicates processes such as plastic creep and strain-hardening, which are assumed to be responsible for the experimental finding.

in Fig. 4.1 measured about 10 h at each temperature] could potentially impact the result. In order to exclude at least this error source, we decided to measure another cm-bar, namely device BC-3, which is nominally similar to device BC-2, before and after 100 h of annealing at $T = 70°C$. From the PCS data, the observed modification of the transition energy of the lasing transition by + (0.07 ± 0.14) meV is insignificant. It rather represents the random error of the technique. Thus an impact of the measuring time to our result is excluded.

In this chapter, we have reported on thermal tuning properties of packaged passively cooled 808 nm emitting 50 W cm-bar high-power diode laser arrays at typical operation temperatures. Two device architectures are compared, namely devices packaged on Cu-heatsinks and identical devices mounted on expansion-matched Cu-W-heatsinks. For a device packaged on Cu-heatsink, we quantified the contribution to the overall thermal tuning rate, namely pressure tuning driven by the relaxation of compressive packaging-induced stress for increasing temperatures. For devices packaged on expansion-matched Cu-W-heatsinks such a contribution is not found, and the observed rate represents almost the genuine thermal tuning rate of the device structure. These findings are strong arguments in favour of the hard soldering technology. If the technical details involved into this technology are once completely controlled, this technology potentially leads to improved device reliability figures.

Chapter 5.

Defects and degradation of high power diode lasers

Defects play an important role in degradation and aging processes of HPDLs. The presence of defects in epitaxial layers, especially in the active layer of diode lasers, generate region of nonradiative recombination that degrade the characteristics of the devices. The origin and nature of defects are usually different. In addition, the interaction of them with other phenomena occurring in degradation process is complicated [10-12]. Therefore, knowledge about defects in specific device structures as well as in particular operation regimes is always required in order to eliminate defects at least in device fabrication process. To fulfil this purpose, our studies presented in this chapter provide results on defects in HPDL structures. These defects were investigated by optical techniques, namely PCS, LBIC, NOBIC and CL. Based on the application of these techniques, defects are localized and characteristic parameters are determined.

5.1. Defect creation in quantum structure of high power diode lasers and recognition of defects by photocurrent spectroscopy

The creation of defects in quantum structures of HPDLs usually occurs according to diverse scenarios, e.g. during fabrication of the semiconductor chip (epitaxy and processing) [10-12], during operation [76,139], due to the packaging induced stress [140,141]. First the imperfections of growing and processing generate defects in HPDL epitaxial layers, substrates, or in the whole structure. These defects evolve during operation and thus degrade device characteristics. Second, it is also

known that the operation (or aging process) of HPDLs possibly creates defects because the crystal structure might be damaged under high optical power density and thermal load. The third reason of defect creation scenario is the packaging-induced strain that deforms crystal lattice thus potentially generates additional defects in HPDL structure.

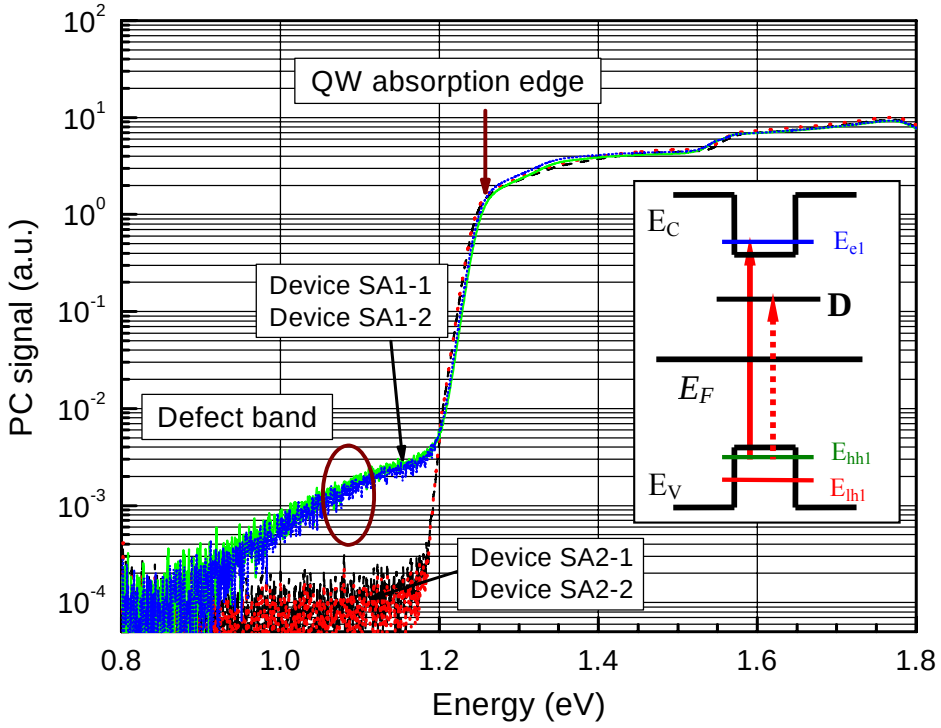

Figure 5.1: PC spectra of four 980 nm HPDLs from two specific batches, namely SA1 (including SA1-1 and SA1-2) and SA2 (including SA2-1 and SA2-2) show pronounced defect bands for devices from batch SA-2. The inset shows a simplified level scheme including valence (E_v) and conduction (E_c) bands, the Fermi-level (E_F) and a defect level (D). The arrows illustrate the QW-transitions (full arrow) and one single deep-level-related transition (dotted arrow).

As discussed in the example presented in section 1.1.3, the PCS technique also can provide information about absorption properties of defects in HPDL structures. A defect band always appears energetically below the QWs absorption edge as described in the inset of Fig. 5.1. Therefore, we can easily distinguish them from fundamental optical transitions (of QW and waveguide) in the active region of HPDLs. Fig. 5.1 shows PC spectra of four fresh (before aging) 980 nm HPDLs from two specific epitaxial batches (SA1 and SA2) having the same nominal architecture. First we can state that devices from the same batch SA1 (SA1-1 and SA1-2) or SA2 (SA2-1 and SA2-2) show very similar PC spectra. With the high SNR of PC spectra (~ 10^5 as seen in Fig. 5.1) measured in FT spectrometer, it is possible to recognize a pronounced

wide-band of defects below the QW absorption edge of devices from batch SA2 that is absent in the devices from batch SA1.

There are several ways to collect defect information by PC spectra. One option predominantly used for screening purposes involves PC measurements without spatial resolution. This is done by enlarging the excitation light spot size of the light source of the FT spectrometer to, e.g., larger than 1 cm (lateral width of cm-bars). Thus the whole front facet of a HPDL cm-bar is illuminated. The PC spectrum, which is obtained after a few minutes, cf. section 2.1.2, is a result of an averaging procedure across the whole bar and is called PC "overview" spectrum. This approach does not require any effort for alignment purposes and thus reduces the total measuring time. Another option involves the use of the µPC setup with high spatial resolution as described in section 2.1.2 and to perform a scan measurement of PC spectra along device surface. Thus, we may get information about the spatial distribution of defects in the devices, e.g. along the lateral direction of a HPDL cm-bar, with the spatial resolution of our µPC setup of about 30 µm. The alignment to get maximum signal for µPC measurements is more difficult, and the total measuring time is much longer. Because of using microscope objective and lens for collimation, we have to carefully check whether the optics used for this purpose blocks the excitation photons in the energy region where we expect to see defects. This might possibly happen, e.g., if we use the fused silica microscope objective and lens, whereas detection of defects is attempted in the mid-infrared range.

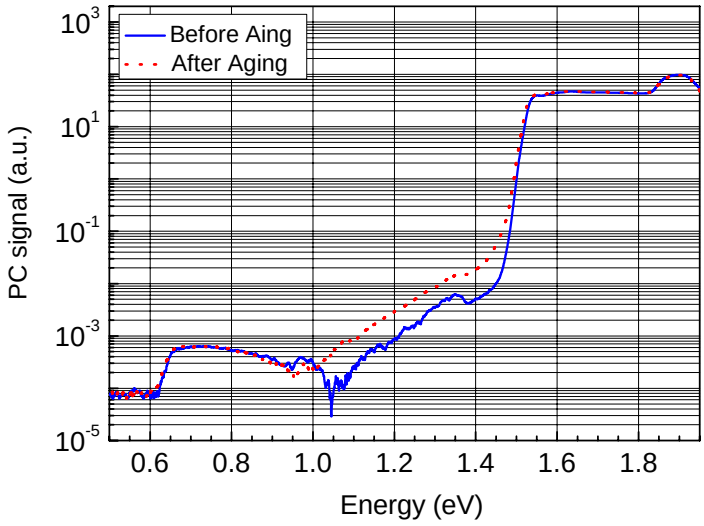

Figure 5.2:

PC spectra of the 808 nm HPDL single chip SB1-1 before (solid line) and after 1000 h (dotted line) of operation show the creation of defects at the wide band starting at 1.05 eV.

In the Fig. 5.2, we present an example of defect creation during the operation of a representative 808 nm HPDL (device SB1-1). The fresh chip (solid line) already shows the existence of defect-level related shoulders at absorption photon energy of 0.65 eV, 0.95 eV and broadband starting at about 1.05 eV. They are most likely generated during growing and processing steps. After 1000 h of operation, the aged

chip was measured again by applying the same procedure and the same apparatus parameters. The result is shown in Fig. 5.2 (dotted line). The comparison of fresh and aged devices points to additional defect creation in the defect band starting at 1.05 eV with an average factor of 4 higher for the aged device, whereas the concentration of the other defects (0.65 eV and 0.95 eV) seems to be not substantially affected.

5.2. Defect enhancement in high power diode laser during operation

The previous section has already introduced an example for the creation of defects during operation. Now, in this section we will discuss more details obtained when monitoring the defect enhancement that was observed during aging processes of HPDLs.

To monitor the evolution of defects, we performed PC measurements on an 808 nm HPDL cm-bar. The sample is named BD-1 and described in section 2.2.5. Before operation, both the PC overview spectrum and the µPC spectra were measured. The µPC spectrum from the center of one emitter of the fresh cm-bar is shown in Fig. 5.3 (a); see solid line. After that, constant power aging (P_{cw} = 30 W) of the bar was done at the standard temperature (T = 25°C) in industrial aging stages for 1500 h. The aged bar was measured again under the same condition as before aging. The dotted line in Fig. 5.3 (a) represents a µPC-spectrum after aging at the same position where the unaged µPC spectrum (solid line) was measured. There is a pronounced lifting up of the defect band below hh1-e1 absorption edge (1.543 eV) by factor of more than 10. We should note that such a spectrum, at least in part (below ~ 1.6 eV), resembles the absorption properties of the waveguide including the QW. This particular emitter is selected as subject of our study because of the initial presence of several deep-level defect transitions (observed in PC overview spectrum) that manifest themselves as shoulders at photon energies below the onset of the QW absorption edge at 1.543 eV (one shoulder is indicated by an arrow in the inset of Fig. 5.3.a). Despite this clear evidence for the initial presence of defects in the emitter, it did not contain any detectable dark line defects, as verified by inspection of the spontaneous emission measurement (EL) [142]. At this stage of the investigation, also the lasing of the emitter did not differ from the behavior of other emitters of the cm-bar, especially not from the neighboring ones. Each of the maps in Fig. 5.3 (b) and (c) displays 42 µPC spectra along the considered emitter in center before and after aging. A clear increase of the defect bands at photon energies below 1.543 eV with aging is seen for the emitter in the center. Additionally, a significant generation of “background” defects is also observed (as indicated by a contrast of the maps 5.3 (b) and (c) below the 1.543 eV edge). Thus there is an enhancement of all defect bands in the HPDL bar during the operation.

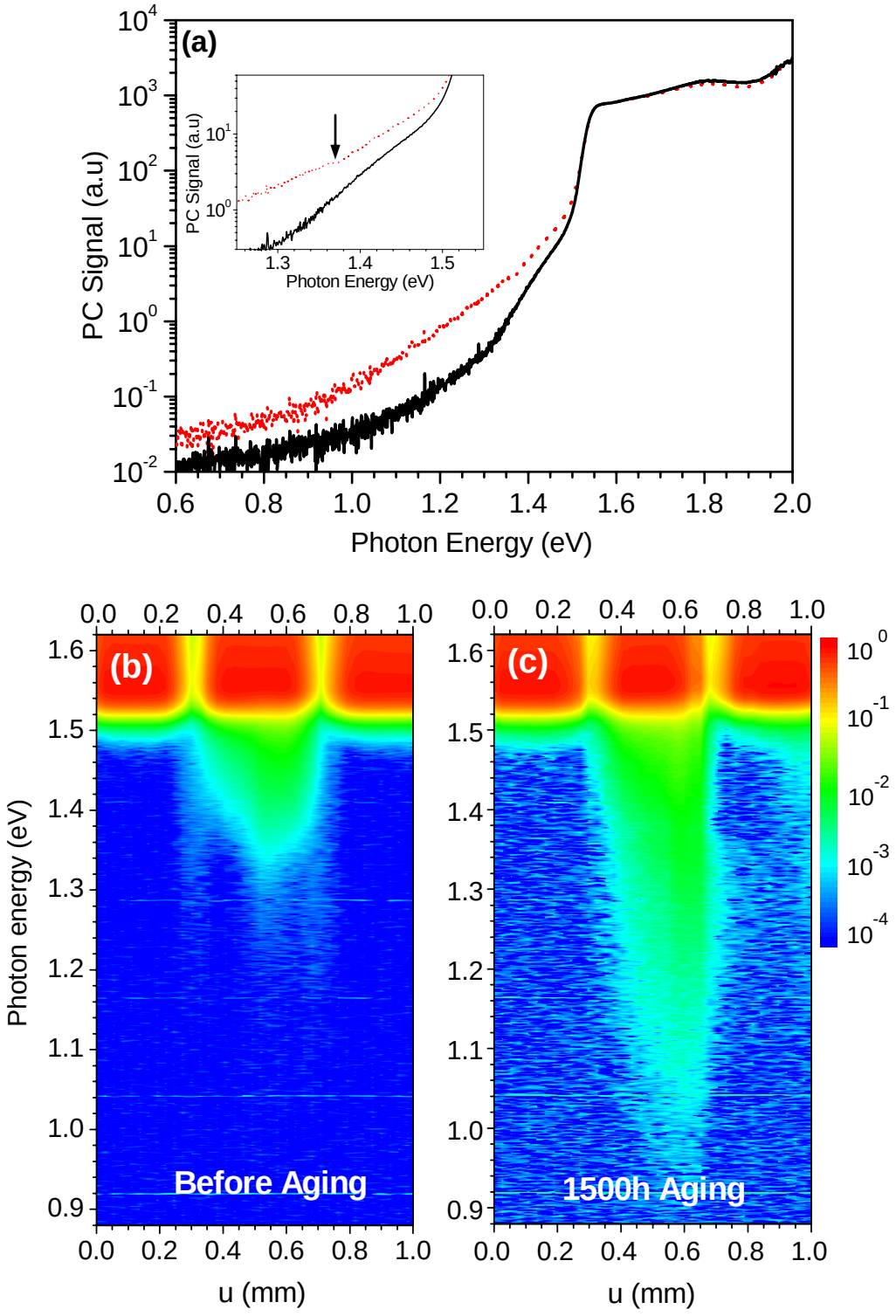

Figure 5.3: µPC spectra from single emitters of the 808 nm HPLD bar BD-1.
(a) Normalized µPC-spectra from the center of one single emitter of the HPLD bar before (solid line) and after 1500 h aging (dotted line). There are shoulders (for both fresh and aged curve) at about 1.35 eV within the defect band (indicated by the arrow in the inset) caused by the onset of different defect - to - (sub)band transitions. (b) and (c) display maps of 42 normalized µPC-spectra scanned along the emitter and parts of the neighbouring ones before and after 1500h aging. The bar code shows scale of PC signal for each point of the maps.

Beside that, after 1500 h of operation, the particular emitter was examined with respect to the output parameters. The result did not indicate any failure of the emitter although it contains initial defects before operation. Thus we can state that these observed defects become generated in a “gradual degradation” processes in the HPDL bar.

The second result that we will discuss here is the evolution of defects in red-emitting HPDL (RD-1) with emission wavelength at 650 nm. The device was described in section 2.2.2. PC spectra were subsequently monitored after various operation times during burn-in for operation at 0.9 A cw at room temperature (25 °C). The PC spectra from the pristine device and subsequent spectra after 9-, 30-, and 55-hour operation are shown in Fig. 5.4. From the result, we clearly see a substantial increase of the defect bands that have the onsets starting at 1.45 and 1.685 eV for the device operation times of up to 55 h. After 55 h of aging, the enhancement factor reach, at lest, a value of three for these defect bands. In addition, the optical output power was also checked during this time. We found that the emission power dropped by 11% after 55 h of aging. This establishes a correlation between deep level defect concentration enhancement and device degradation.

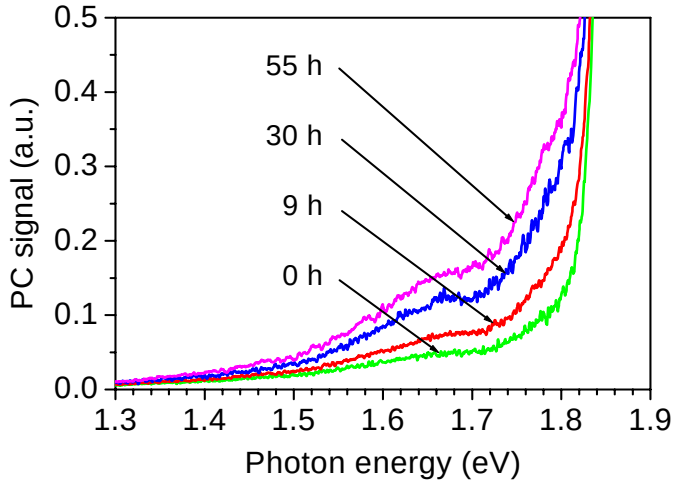

Figure 5.4:
PC spectra from a pristine red-emitting HPDL and subsequent spectra monitored after 9, 30, and 55 h of regular operation at 0.9 A cw (device RD-1).
The shoulders are related to defect bands start at about 1.45 and 1.685 eV.

5.3. Distribution of defects in high power diode laser structures

The generation of defects is obviously related to the degradation of HPDLs. Of course, the question arises whether we can we determine the location of such defects or not. By using optical techniques, namely PC spectra, LBIC, NOBIC, we are able to show the distribution of defects in HPDL bars and determine the localization of defects within the waveguide of red-emitting HPDLs. Thus the defect centers can directly interact with carries, which radiative recombination rather should contribute to the lasing effect, i.e. device functionality.

5.3.1. Defect distributions in high power diode laser bars

There are several spectroscopic means to detect the "macroscopic" distribution of defects in HPDLs, e.g. LBIC [33,82], PCS [82,142], thermography [84,143], μPL [141], EL [76]. The word "macroscopic" implies the spatial resolution of the measurements is on the micrometer scale. In this section, we employ two methods, namely LBIC and PCS, for the investigation of defect distributions in HPDL bars.

First, we perform LBIC scan measurement along 980 nm HPDL tapered bars. We denote the test devices as TB2-11, TB2-21 and TB2-22. The description of these bars has been done in section 2.2. By using the LBIC technique, we are able to choose a special excitation wavelength that allows for selective excitation, e.g. in order to visualize defects. Because of a emission wavelength in the 980 nm region, i.e., the absorption of QW starts near 980 nm, we can usefully employ two excitation laser wavelengths, namely 633 nm and 1064 nm, for LBIC scanning measurements. The excitation at 1064 nm allows for the generation of quasi-free carriers exclusively by optical transitions involving defect centers, cf. e.g. Ref. [34], whereas the excitation wavelength of 633 nm provides the generation of free carriers by defect-related as well as by direct interband transitions within the QW and the waveguide. The 633 nm LBIC scans usually highlight the lateral structurization of laser bars while the 1064 nm LBIC signals delivers information about relative defect concentration at different local positions along the device.

The 1064 nm LBIC signals are typically very weak for defect-free devices. But in Fig. 5.5 (a) we can see a remarkable 1064 nm LBIC signal for device TB2-11 at some particular positions, namely emitter regions. The observed peaks strongly correlate with the degradation behaviors of these particular emitters that we found after 500 h aging of the device.

In Fig. 5.5 (b) and (c), we present the results for devices TB2-21 and TB2-22 obtained in the same way as done for device TB2-11. For the device TB2-21, see Fig. 5.5 (b), the defect signatures are clearly seen on the left-side of the bar and cover the whole region of particular emitters. The right-side seems to be less affected, but the defect concentration is still considerable. Fig. 5.5 (c) of device TB2-22 displays an increasing defect concentration from the left-side to right-side of the bar. Both of the bars TB2-21 and TB2-22 show a degraded behavior after operation that obviously is related to the appearance of defects in the "fresh" devices. An additional effect is visible in Fig 5.5 (b) and (c). This is the dropping of the signal (see 633 nm LBIC scans) at some areas in between emitters and is related to the electrical contact of this region, which is sometimes more, sometimes less developed. We assign this to the degree, how much the solder connects this region to the sub-mount or not. However, there is a coincidence that there are more defects, where the contact is worse.

Therefore, we assume the metallized edges of the emitter stripes could be the starting point of degradation processes for these particular devices.

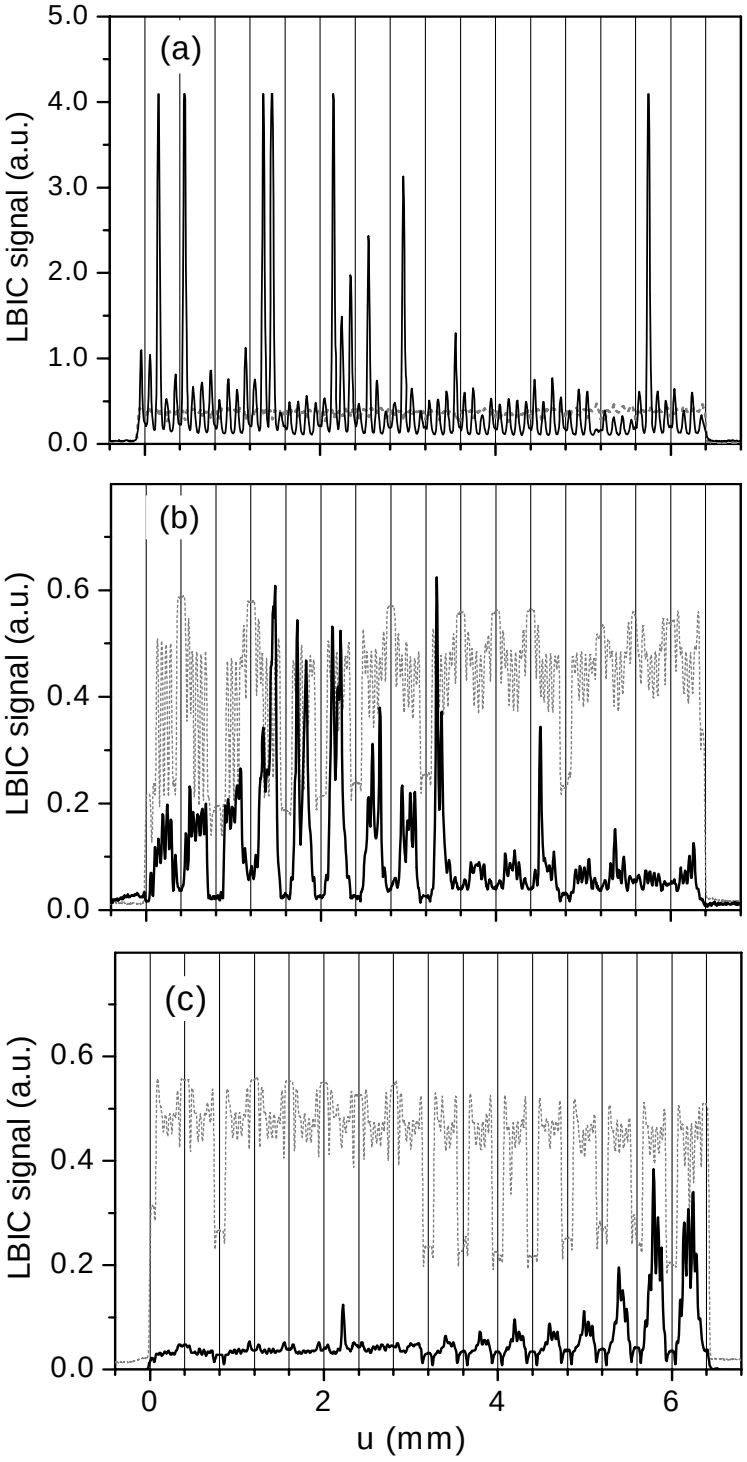

Figure 5.5:

LBIC measurements performed for 980 nm HPDL tapered bars: 633 nm LBIC-scan (dotted line) highlights the lateral structurization of the bars and 1064 nm LBIC-scan (solid line) is used for defect localization.

(a) Results from device TB2-11 show defects at particular emitters along lateral axis of the bar

(b) Result for device TB2-21: the defects are concentrated on the left side of tapered diode laser bar and cover the whole emitter regions.

(c) Result from device TB2-22 with a low defect concentration at the left-hand side, and defects grow significantly on the right side of the tapered laser bar.

The above results illustrate a possibility of the LBIC technique to recognize defect distributions along HPDL bars. Now, we provide another mean that can be used for this purpose, namely PCS. Fig. 5.6 shows a map of PC spectra scanned. This map contains 75 μPC spectra measured along a segment of 5 emitters from an 808 nm HPDL cm-bar (device BB-2). The defect bands and band tail state are more

pronounced in the emitter number 1 and 3 (marked with solid arrows). At the grooves (marked with dashed arrows) an increased concentration of defects in wide spectral band is clearly visible. The PC technique can provide both spectral and spatial distribution of defects. This is an advantage of the method. However, we should note that this approach requires a rather long measuring time compared to the LBIC technique. Therefore, the choice of the defect recognition technique must be considered in relation to information requirements regarding defects.

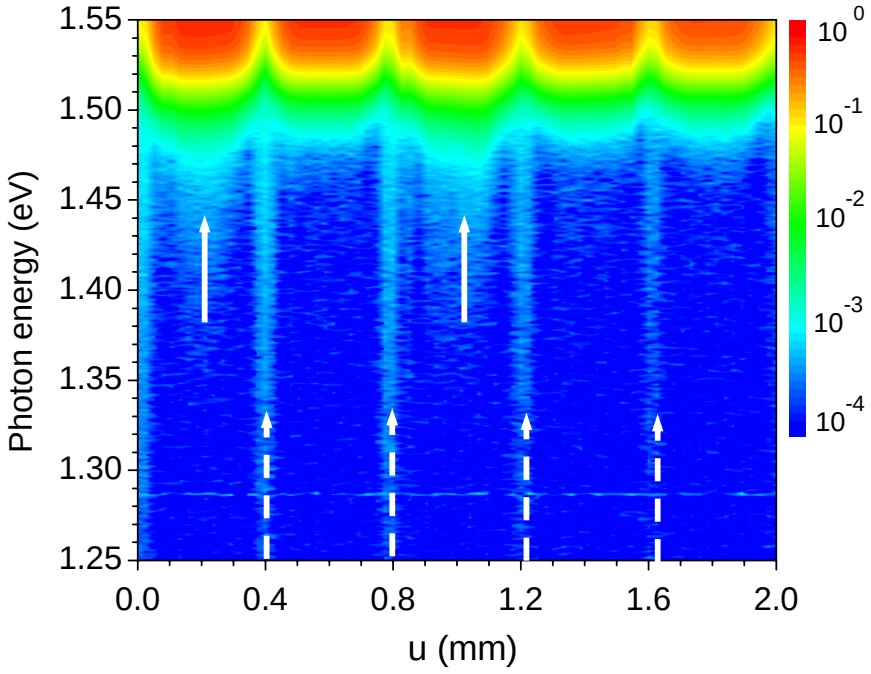

Figure 5.6: Map of 75 µPC spectra measured along a segment of 5 emitter of an 808 nm HPLD bar (device BB-2). The defect distribution along the HPLD bar is shown with both spectral and spatial resolution. The solid arrows mark the emitters where defects are pronounced. The dotted arrows show the groove positions with high concentration of defects in a wide spectral band.

5.3.2. Observation of deep level defects within the waveguide of red-emitting high power diode lasers

So far, we have discussed the macroscopic distribution of defects in HPDL structures. However, in practice, the determination of "microscopic" distributions of defects in HPDLs, e.g. in epitaxial layers, is needed in many cases because this result is valuable for improving the performance of HPDL devices. In this section, we introduce the investigation of defects in red-emitting HPDLs that shows the existence

of deep level defects within the waveguide of the devices. Beside PC and LBIC techniques, we use a complementary technique, namely NOBIC that provides a sub-micrometer spatial resolution, to localize the deep level defects in the red-emitting devices. The goal of this study is to get insight into the impact mechanism of deep level defects to the degradation of red-emitting HPDLs. To the best of our knowledge, such studies for red-emitting devices are introduced here for the first time.

The 650 nm emitting HPDLs that serve as test devices have been described in detail in section 2.2.2. The schematic diagrams of the layer sequence and the front view geometry of these red-emitting lasers are shown in Fig. 5.7. When analyzing these devices in aging tests, no significant performance degradation occurs during the first 1000 h of operation. Here we present data from devices originating from 4 different epitaxial test batches, namely RA, RB, RC and RD (listed in section 2.2.5).

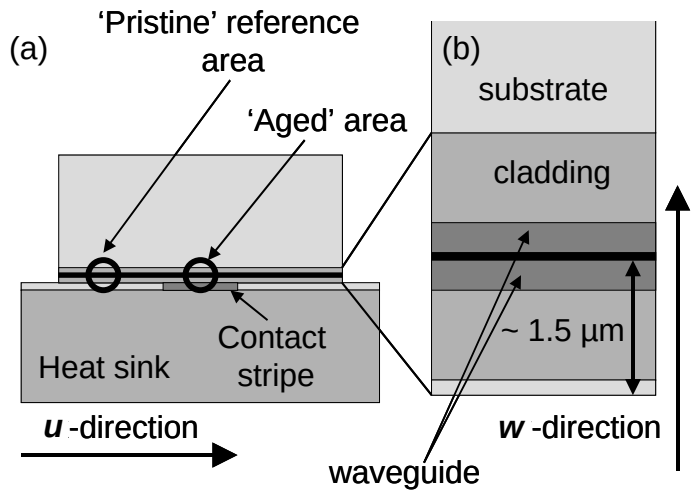

Figure 5.7:
Schematic diagram of the front view of a red-emitting HPLD (a) and the epitaxial layer sequence of the laser structure (b): the u-direction is along lateral axis of laser and w-direction is growth direction; the "pristine" reference area is outside of the metallized contact stripe and the "aged" area is inside this stripe.

First we describe the observation and analysis of deep levels in these devices. The PC technique allows for monitoring absorption spectra of the laser waveguide. The achievement of a SNR of the PC spectrum of better than 10^6, see Fig. 5.8 (a), provides a means for analyzing even the weak absorption shoulders caused by ionization or de-ionization of deep level defects, i.e., defect-to-(sub)band transitions. The spatial resolution of the PCS technique, however, is rather poor in this case (the excitation spot size Ø = 400 µm in the present experiments). The LBIC technique provides scans of the photocurrent versus position, e.g., along devices. The setup used in this study has a spatial resolution of about 10 µm when scanning in one dimension, e.g. along the u-axis perpendicular to the growth direction; see Fig. 5.7 (a). The NOBIC (the setup was introduced in section 2.1.3) is considered an extension of LBIC with increased spatial resolution of about 150 nm. In this case, during scanning, we use the excitation lasers emitting at 730 nm or 633 nm (marked with arrows in abscissa of Fig. 5.8.c) Our NOBIC experiments can perform measurements of photocurrent (signal and phase) that provide maps of signal intensity over an area of 2.15×2.15 µm^2.

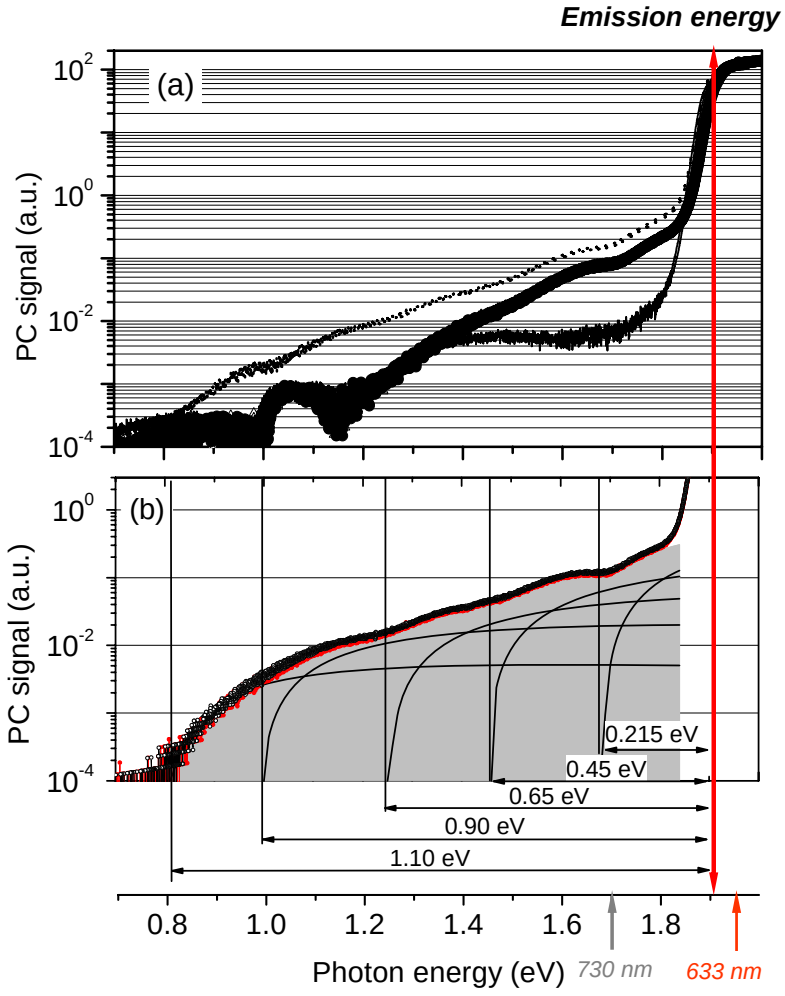

Figure 5.8:
(a) PC spectra from 6 red-emitting HPLD being prepared from 3 epitaxial test batches (RA, RB, RC). The spectra from the individual devices (in each batch denoted as 1 and 2) are almost identical, and therefore hardly distinguished in this display.
(b) Fits of the spectra from devices RB-1 and RB-2 by 5 defect level-to-band transitions. The 'level depth' corresponding to the particular optical transition is indicated. The gray area marks the sum of the 5 contributions matching the experimental data.
In abscissa, the arrows mark the wavelengths (633 nm and 730 nm) that are employed for the LBIC and NOBIC measurements.

In the following discussion, we use NOBIC scans across the laser facet along the growth direction, here called the w-direction; see Fig. 5.7 (b).

Starting the spectroscopic analysis by using PC spectra, Fig. 5.8 (a) shows typical spectra from 6 pristine red-emitting devices belonging to 3 different epitaxial batches (RA, RB, RC). At about 1.9 eV (~ 650 nm, see arrow across all parts of Fig. 5.8) a pronounced absorption edge due to the ground-state transition in the QW is observed. At lower energies, the shoulders caused by deep level defects are visible. Since the spectra from devices of the same batch (epitaxial run), e.g. RA-1 and RA-2, show almost identical spectra, we consider these low-energy shoulders as being 'batch-specific'. In Fig. 5.8 (b), we present a fit of the shoulders found in the PCS spectra of devices RB-1 and RB-2 to 5 transitions via deep levels with depths of 1.10, 0.90, 0.65, 0.45, and 0.215 eV. The gray area illustrates the sum of all these contributions, which are calculated according to the model introduced by Lucovsky [26].

Batch RD, in general, shows an inferior long-term reliability (with degradation rate ~ 10^{-3} h^{-1}) compared to previously discussed charges RA-RC. It shows more pronounced deep level contributions but with the same energetic depths as observed for the regular charges. This makes batch RD a promising candidate for aging-experiments. PC spectra from device RD-1 monitored at various operation times during burn-in were introduced in Fig. 5.4. Two pronounced defect bands (starting at 1.45 eV and 1.685 eV in Fig. 5.4 that were observed for device operation time of up to 55 h correspond to deep defect levels of 0.45 eV and 0.215 eV in Fig 5.8 (b), respectively. In addition, we found the degradation behavior of the device with an

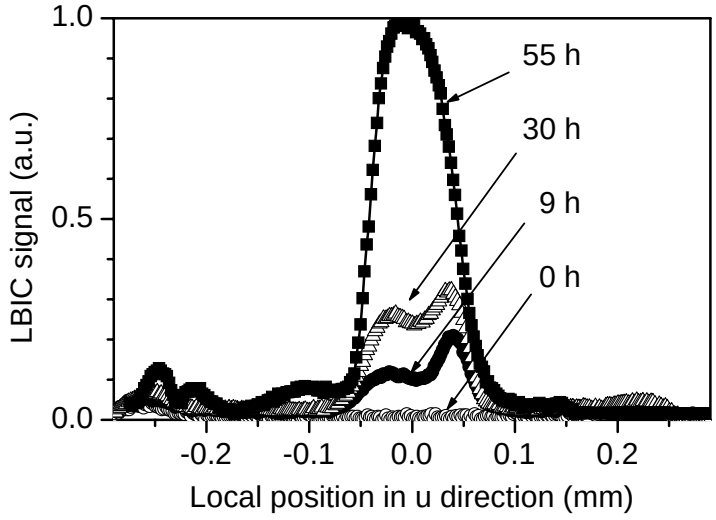

Figure 5.9:

LBIC scans taken at 730 nm excitation wavelength (for defect recognition) along the front facet of device D1 monitored after 9, 30, and 55 h of regular cw operation at 0.9 A. The LBIC signal confirms the defect enhancement in the active region underneath the metallized emitter stripe during the burn-in time.

evidence of emission output power decreased by 11 % after operation.

We now discuss in detail the spatial localization of the deep level defects observed in device RD-1 based on the results obtained by LBIC and NOBIC (Figs. 5.9 and 5.10). In Fig 5.9, LBIC data, obtained for resonant defect level excitation, are reported. Obviously, in the active region, i.e. underneath the metallized emitter stripe, a substantial operation-induced increase of the deep-level related photocurrent is observed. Thus, there is a clear correlation between the location of stripe region, which experienced the load during operation, and the creation of operation-induced deep level defects. This LBIC measurement with a limitation of the spatial resolution is not able to show any localization of defects within the epitaxial layer sequence, i.e. along the w-direction. Therefore, the NOBIC experiment was employed as the solution for this problem. The results of Figs. 5.10 (b) and (c) provide the vertical localization of the defects by NOBIC on a nanometer scale as done in Refs. [91,145]. This is essential for our line of arguments, because, e.g., also the 0.4 μm thick highly doped p-GaAs contact layer is another likely candidate for generation or accumulation of deep level defects during high-power operation. Since this contact layer is separated from the QW by only 1.1 μm, see Fig. 5.7 (b), the LBIC data would not allow for an

unambiguous assignment. For this particular NOBIC experiment, we use device RD-1 after 55 h of operation, in order to avoid measurements (and alignment) before and after device aging. As 'pristine' reference area serves a region outside the emitter stripe, which has not been affected by the high current density during the 55 h of operation; see circles in Fig. 5.7 (a). NOBIC-scans are taken at an excitation wavelength of 633 nm and 730 nm, which are marked by arrows in abscissa of Fig. 5.8 (c). The first one (633 nm) provides interband excitation of the QW, whereas 730 nm matches the maximum of the absorption band of the defect band, which starts at 0.215 eV below the QW band edge. Comparing the normalized Figs. 5.10 (b) and (c), the most striking feature is a 2.3 fold increase in the deep level defect contribution to the photocurrent in the "aged" area below the emitter stripes with respect to that in the "pristine" reference area. The experiment had been done four times at different locations within and outside the contact stripe. In all cases the "aged" area reproducibly exhibited a 2-3 times increase of the defect-related photocurrent (730 nm) compared to the interband one (633 nm), which serves here as the reference.

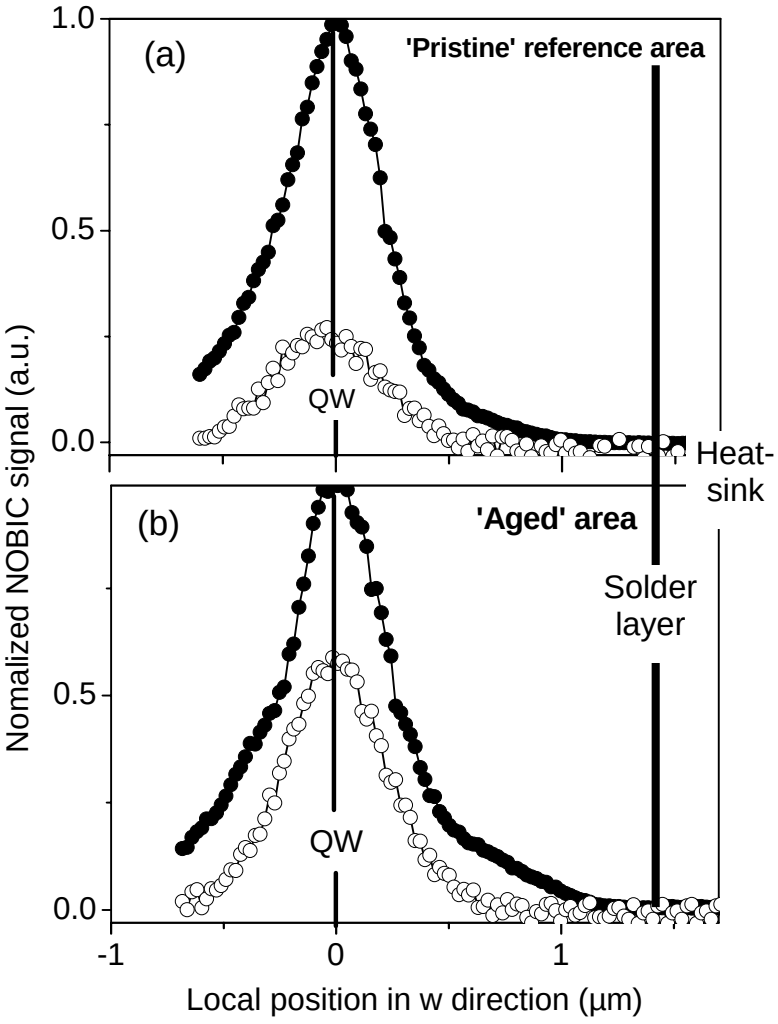

Figure 5.10:

NOBIC scans parallel to the growth direction across the active region of the device at lateral positions of "pristine" reference area and "aged" area (see Fig. 5.7.a). Full circles represent data obtained at an excitation wavelength of 633 nm, open circles denote data obtained for 730 nm excitation. The scan was extended across the solder layer to the heat sink in order to ensure that even the highly doped GaAs-contact layer is completely included.

Even though a detailed discussion of the microscopic nature of the detected deep-level defects is far beyond the scope of our work, we can draw some conclusions about their microscopic nature. Since we do not observe any dark-line or dark-spot defects within the pristine devices, we assign the observed defects to point defects, probably caused by native point defects (e.g., vacancies or interstitials) or foreign impurity atoms. Fig. 5.8 (a) shows clearly that the ratio of the different contributions changes depending on the particular epitaxial test batch. Thus it is likely that a number of physically different types of defects contributes to the creation of the five absorption shoulders. The defect contributions with a depth of 1.1 and 0.9 eV are considered to be created by mid-gap states, which probably also act as recombination centers for processes of Shockley-Read-Hall type [145,146]. Our experiments on the localization of the deep level defects still leave the localization along the laser axis (v-direction along cavity) open. The "penetration depth" of the excitation beam for all three PC-related techniques described above is not longer than about 30 µm (estimate for GaAs-based materials). Therefore we have to clarify, whether the deep level defects are concentrated beyond the front facet or distributed along the whole cavity. Another important issue is the search after a correlation between the deep level configuration within a particular epitaxial batch and the long-term reliability of devices prepared from it. Further work on these important topics is continuing.

Summarizing, the waveguides of red-emitting HPDLs have been analyzed regarding the presence of deep level defects. Deep level configurations in pristine devices are discussed and the kinetics of defect creation during device operation is monitored. For pristine device, a fit of the absorption bands monitored by photocurrent measurements reveals level depths of 1.10, 0.90, 0.65, 0.45, and 0.215 eV. For one device batch, we show the concentration of the 0.45 and 0.215 eV deep defect levels to grow within 55 h of device operation. In addition, we provide a clear localization of the defects within the epitaxial layer sequence by using LBIC and NOBIC techniques. We show that light, which is confined within the laser waveguide, interacts strongly with the deep level defects detected. As a consequence, these defects, if present in higher densities, can affect device output properties in a direct way.

5.4. Analysis of high power diode laser degradation by optical techniques

The preceding sections of this chapter have provided information on defects in HPDLs. However, we did not address defect-related degradation in detail. In this section, we will deal with degradation behaviour of HPDLs based on the results achieved from some representative devices. The methodology in the studies focuses on optical techniques.

5.4.1. Laser-beam-induced-current analysis of degradation properties in high power diode laser bars

In the preceding sections, we already showed the powerful capabilities offered by the LBIC technique for the detection of defects in HPDLs. Now, we will demonstrate the efficiency of the LBIC approach even as a screening tool as well as its capacity for predicting device failure well before any degradation of the emission properties is observed.

First, we present the results performed on AlGaAs-HPDL cm-bars emitting at 808 nm. The two devices under test, namely BB-2 and BB-3 (see Table 2.1) were chosen exemplarily out of a batch of 20 nominally identical devices generating optical output powers of 30 W.

The experiments started with the application of the μPC and LBIC techniques. The absorption properties of the active region of the devices are inspected by μPC [142] whereas LBIC was measured for two different excitation wavelengths, namely 633 and 830 nm. In terms of excitation energy, the particular wavelength 830 nm in LBIC allows for the excitation energetically slightly below the lowest quantum-confined transition within the QW. It is used for defect recognition purposes, similar to using of 1064 nm or 730 nm excitation wavelengths in the investigations of section 5.3. It is worthwhile to address the advantage of the LBIC technique, namely the small measuring time. As described in section 2.1.3, with a medium spatial resolution, the LBIC scan is performed within a few minutes only. Therefore, the LBIC allows for quicker screening of the HPDL bars compared to, e.g. μPCS, where the measuring time per inspected location along a bar is expected to be three orders of magnitude larger.

Fig. 5.11 (a) shows μPC maps including 75 photocurrent spectra representing the absorption along 5 emitters of the pristine array BB-2 in the photon energy range just below the onset of the QW absorption edge at 1.543 eV, corresponding to the emission wavelength of 808 nm. Figure 5.11 (b) displays LBIC scans along the whole device at 633 nm and 830 nm excitations. Considering the defect absorption along the marked line at 830 nm in μPC spectra map of Fig. 5.11 (a) between 2 and 4 mm, one finds qualitatively the same information of pronounced defect signatures at emitter number 1 and 3 in this segment as obtained by the LBIC scan measured at an excitation wavelength of 830 nm displayed in Fig. 5.11 (b). For the device BB-3, under similar conditions, we obtained LBIC data as shown in Fig. 5.12 (d). Again, the 830nm LBIC scan exhibits pronounced peaks at specific emitters of the cm-bar.

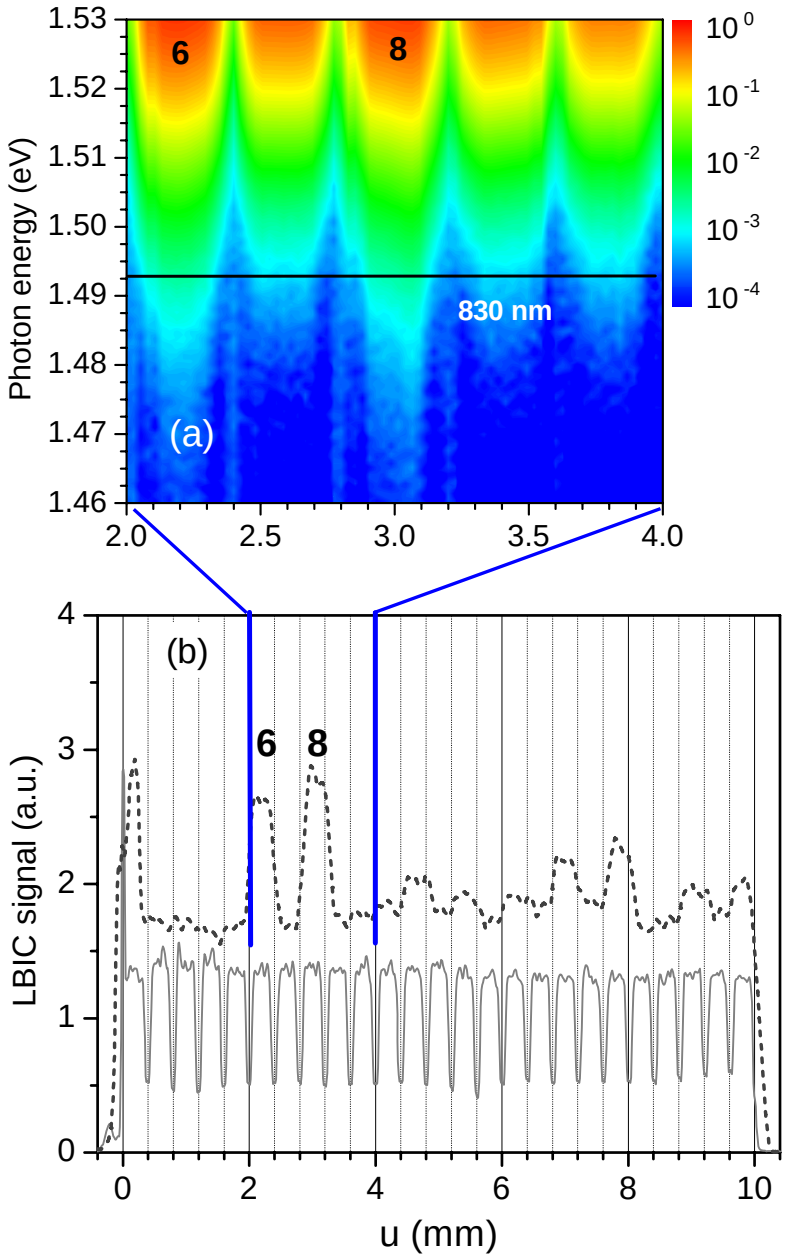

Figure 5.11:

(a) Map involving 75 µPC spectra monitored along 5 emitters (from 6 to 10) of HPDL array A. The bar code scale represents the magnitude of the photocurrent on a logarithmic scale. The lateral step width is about 26.6 µm. The line marks the photon energy corresponding to a wavelength of 830 nm.

(b) LBIC scans along HPLD array BB-2 measured at two excitation wavelengths, 633 nm (solid line) for lateral structure overview and 830 nm (dotted line) for defect recognition. Two pronounced defect peaks appear at emitter number 6 and 8 that are marked also in µPC map.

After the first screening experiments, both devices were subjected to a burn-in test for 180 h at 25ºC at a constant optical power of 30 W. Careful analysis of the emission properties of both pristine devices BB-2 and BB-3 after burn-in below (EL) and above threshold (lasing) have not revealed any unusual emission properties of the emitters that indicated the pronounced defect-peaks in 830 nm LBIC of Fig. 5.12 (d). In particular, they have not shown any indication of degradation, such as reduced emission or even dark line defects. Therefore, the device BB-2 was decided to age 1000 h more in constant current high-power operation. Afterwards emitter failures appear. It turns out that exactly those emitters fail that have formerly shown the peaks

in the 830 nm LBIC scan. This is an evidence for correlation between the defect signature in LBIC and degradation processes.

In order to get insight into the microscopic origin of the gradual aging processes observed above in device BB-2, device BB-3 was opened before any further operation by removing the p-side metallization employing a special etching technique that is described in Ref. [147]. Thus the active regions inside the cavity were directly accessible for further analysis using the high penetration of the excitation e^--beam. In particular, panchromatic CL images as well as spectral imaging CL [148,149] were applied in this stage of investigation. The latter measurements were done at $T = 77$ K, whereas all other measurements, in particular the screening, were done of course at ambient temperature.

The optical active cavity of all 25 emitters was inspected from the top by panchromatic CL. Figures. 5.12 (a) - (c) and (e) - (g) show the CL images from exemplarily selected emitters characterized either by the presence or the absence of 830 nm LBIC peaks, respectively (see arrows). Obviously, these two groups of images differ systematically. Arrays of dark spots are observed at the emitters exhibiting 830 nm LBIC peaks, whereas the other group of emitters shows a rather uniform CL pattern free of dark regions. Monochromatic CL images clearly show that the dark spots are localized in the QW, whereas the cladding and confinement layers are free of any defects.

The CL spectra from exemplarily selected emitters were monitored, too. Fig. 5.13 shows two typical CL spectra from two specific emitters that are representative for the behavior of all monitored emitters of the two respective groups and, more generally, the difference between degraded and non-degraded QW areas. The dashed line indicates the spectrum of a dark spot of the emitter shown in Fig. 5.12 (a), whereas the solid line represents a spectrum of the emitter shown in Fig. 5.12 (e). The substantially different luminescence efficiency, which is already qualitatively observable in the panchromatic CL images, is confirmed. In addition, a 2.3 meV red-shift is observed for the emitters showing the poorer luminescence. This shift is an average value and depends on the "darkness" of the region studied, i.e., concentration of defects. This phenomenon is a common behavior observed in degraded HPDLs of this type. It can be associated with exciton localization effects at interface defects or with stress relaxation due to the formation of dislocations [149,150] or with bandgap renormalization by the generation of defects located near bandtail states. It should be noted that these dark spots are still emitting, which means that they are at very early stages of degradation and do not indicate the formation of extended defects at such an early degradation stage. This rather weak and gradual degradation should account for the absence of any noticeable decay in the electro-optical parameters of the device. On

the other hand, the clear indication for defects at the very on-set of damage mechanism clearly confirms the excellent screening capability of the LBIC technique.

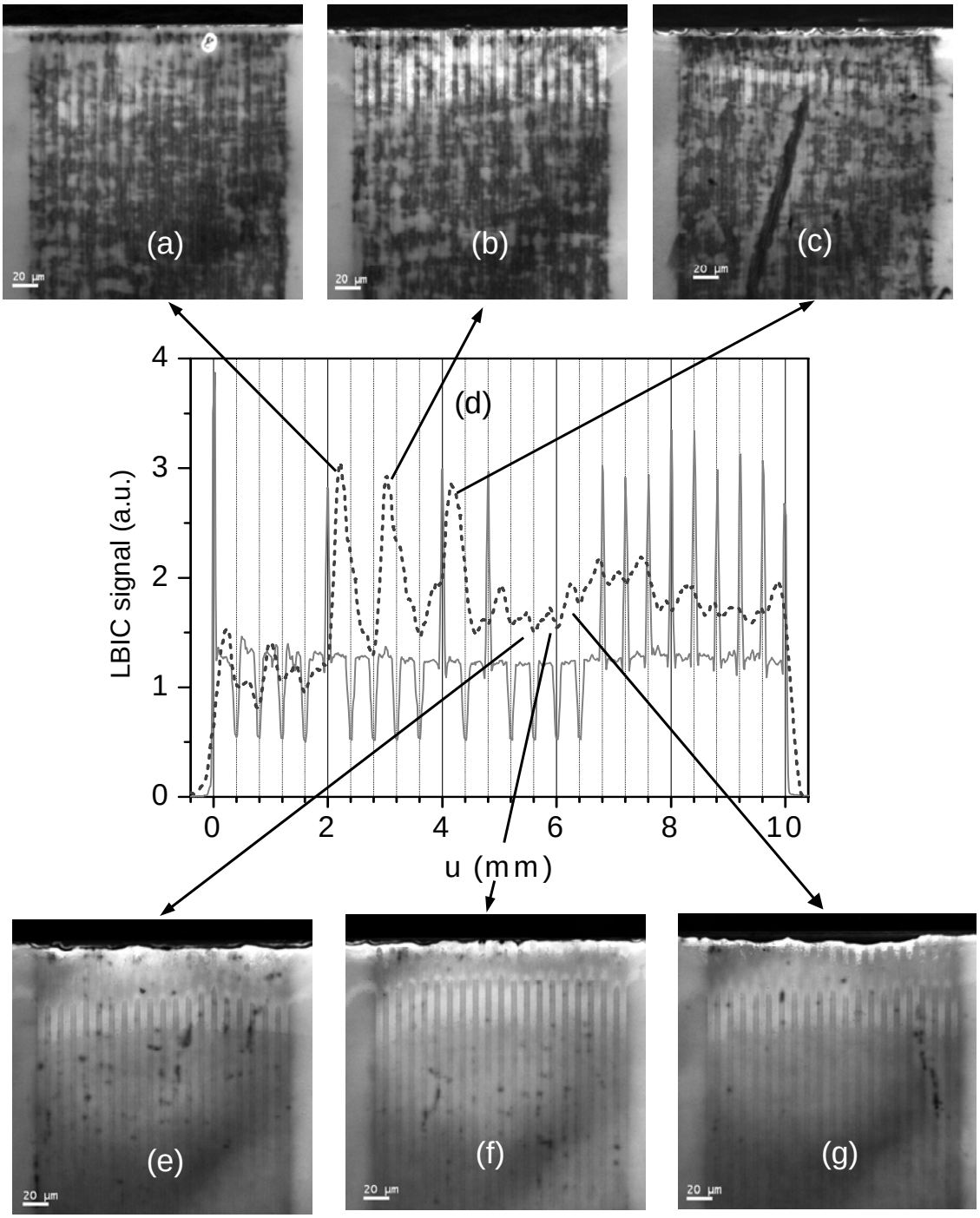

Figure 5.12: Correlation between LBIC data measured at 633 nm (solid line) and 830 nm (dotted line) laser excitation, Fig. (d) and panchromatic CL images observed at a fresh/aged cm-bar BB-3:

Note that, at the emitters, where the 830 nm excited LBIC signal shows peaks also exhibit a panchromatic CL images with a large number of dark areas; see (a)-(c).

Three randomly selected reference emitters from the same bar without special LBIC signature also show rather bright panchromatic CL with a substantially lower density of dark areas; see (e)-(g).

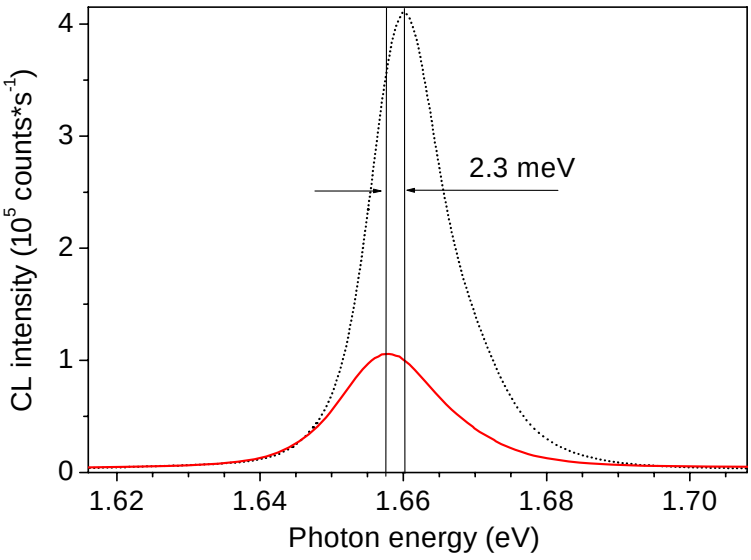

Figure 5.13:
CL spectra from selected emitters represent the behavior of all emitters of the two groups (a-c) and (e-g) in Fig 5.12. The dotted spectrum is taken from the emitter shown in Fig. 5.12 (a), whereas the solid one is monitored from the emitter shown in Fig. 5.12 (e). The shift between the two spectra amounts to 2.3 meV

In addition, we would like to recall here the results that were presented partly in section 5.3.1. The LBIC measurements done for the 980 nm tapered bar, namely TB2-11 with the defect detection wavelength of 1064 nm are shown in Fig. 5.14. The LBIC scans of 633 nm excitation (before and after aging) in Fig.5.14 (a) show a comparable intensity that provides normalization for the comparison of the defect concentration via the 1064 nm LBIC intensity. The pronounced defect peaks that appear in LBIC of the fresh device, see solid line in Fig. 5.14 (b), are a signature of the degradation process. This device was aged and the degradation has been monitored after 500 h of operation. The LBIC of the degraded device (dotted line in Fig.5.14 (b)) show a significant enhancement of defect concentration confirming correlation of defect signature and degradation of 980 nm tapered bar.

Now we address the implications of these experimental results. Obviously, the collection of LBIC data is done rather quickly as described above since the spectral information of a PC spectrum is reduced to one specific wavelength (display in Fig. 5.11 with 830 nm substitute for whole spectral range of PC spectrum). If the LBIC scanning wavelength is appropriately chosen, defects may be located even within an extended device. Considering the results presented, it becomes clear that LBIC scanning can be sensitive to specific defects even before these defects degrade the emission properties of the particular device. This allows the prediction of failure events for specific emitters within an array. Additional advantages of LBIC compared, e.g. to CL, are the non-destructive character of the method and the fact that no sample preparation is required. Because of these features, we can consider LBIC an efficient screening tool for investigation and prediction of degradation effects at HPDLs.

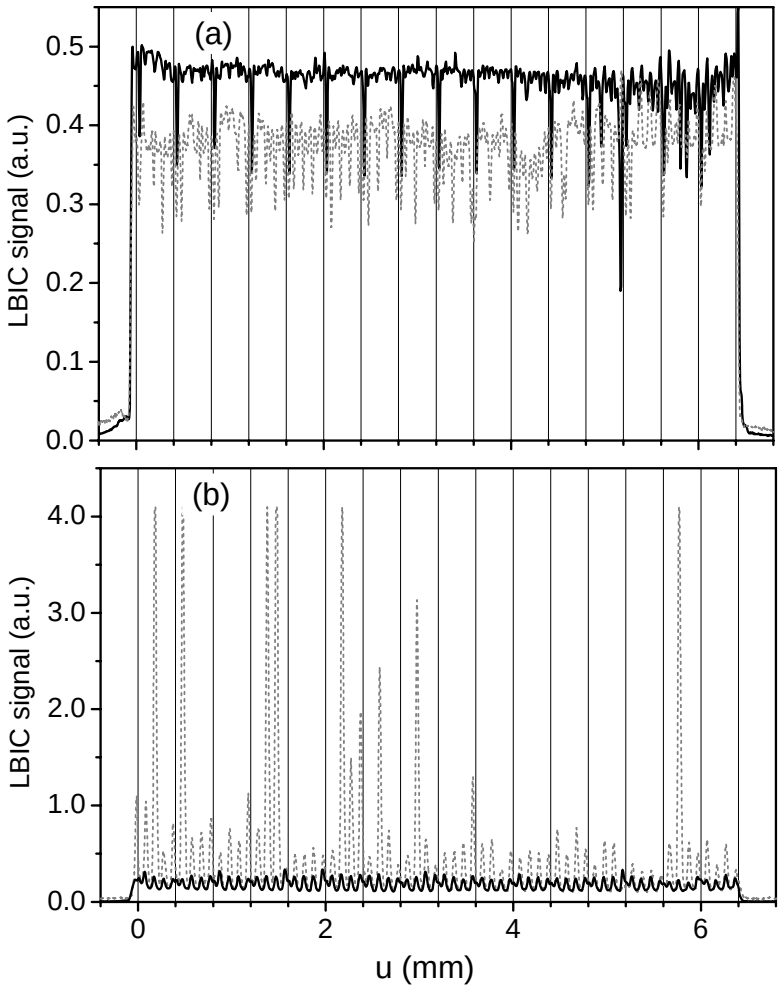

Figure 5.14:

LBIC measurements for 980 nm emitting tapered HPLD bar TB2-11 before aging (solid lines) and after 500 h aging (dotted lines):

(a) LBIC signals obtained for 633 nm wavelength excitation show lateral structure of the device before and after aging.

(b) LBIC signals of 1064 nm wavelength excitation visualize the defect distribution along the bar. After aging the LBIC result shows a substantial enhancement of defect contributions.

However, there are also limitations for the successful applicability of LBIC-screening. Tests carried out with devices packaged by soft-soldering on Cu have not shown the nearly 1:1-correlation observed for hard soldering on Cu-W alloys. Furthermore, if 980-nm emitting devices are considered, the correlation between 'defect-LBIC' and subsequent emitter failure is also poorer. In all cases, however, it is clear that inhomogeneous LBIC-scans across a bar, in particular for below-QW-edge excitation photon energies, are indicative for a potentially reduced reliability. Our measurements therefore have to be understood as one specific example, where failure prediction becomes possible even for high-quality devices, at least, as long as there is one particular dominating degradation mechanism, which is addressed by LBIC.

5.4.2. Investigation of Al-free broadened laser structures at 915 nm by photocurrent spectroscopy

Degradation takes place in very complex ways. In this section, we will discuss about another degradation signature that is related to an important parameter of

semiconductor materials or structures, namely the Urbach parameter [24]. The device under test, in this case, are Al-free laser structures emitting at 915 nm. The PCS technique was used as the main investigation tool.

The devices are single laser chips with 0.1 mm emitter width and 1 mm cavity length and classify into three groups according to QW structures (detail description presented in section 2.2). The first group includes two SQW devices (SC1-1 and SC1-2). The devices from the second group, namely SC2-1 and SC2-2, are also SQW structure but with different waveguide material. In the last group, two devices (SC3-1 and SC3-2.) were fabricated based on double QW structure. The optical output power of the devices from the three groups is about 1W at operating current of 1.8 A

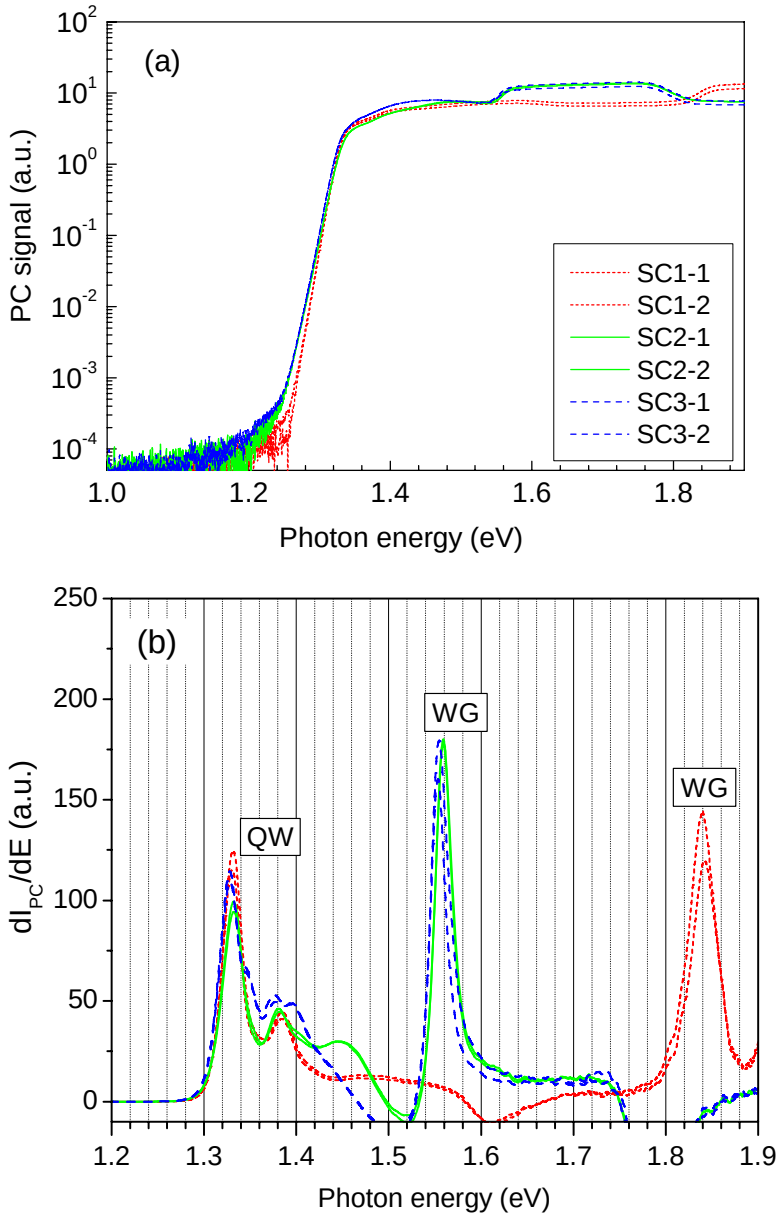

Figure 5.15:

(a) PCS overview spectra of Al-free 915 nm BA HPLDs from 3 different batches (SC1, SC2, and SC3); there is no pronounced defect shoulder appearing in any of the devices.

(b) First derivative of the PC overview spectra show optical transitions in the Al-free 915nm BA lasers: the different architectures are indicated by different first derivatives; the spectral position of the lasing transition differs only slightly and is batch-specific.

All of the six devices were measured by taking PC overview spectra. The results are shown in Fig 5.15 (a). We do not see any signature of defect bands below the QW edge. The first derivatives of the PC spectra are shown in Fig 5.15 (b). The different architectures are highlighted by differences of first derivatives. The spectral positions of the lasing transitions (first QW transitions) differ only slightly and are batch-specific. But within one batch, they are almost the same. The first QW transitions of devices from the two groups of single QW structures are almost not shifted with respect to each other, whereas the double QW structures are slightly red-shifted by about 3 meV.

Although there is no pronounced defect band in any of the PC spectra, the devices show differences regarding the band tail states (or slopes of QW absorption edges) in PC spectra that are described by the Urbach parameter. This specific behavior is displayed in Fig. 5.16. The slope E_0 describes the exponential part of the QW-PC edge according to

$$I_{PC} \propto exp(E/E_0)$$

Here I_{PC} is the photocurrent and E is the photon energy. E_0 represents the Urbach parameter and is a measure for the homogeneity of the SQW or MQW [34]. In SQWs, the main source of the Urbach parameter increase is related to structure inhomogeneity, e.g., well-thickness or well composition non-uniformity or both within the well layer, the roughness of QW/waveguide interface and the built-in strain. For MQWs we must take into account an additional mechanism, namely the reproducibility of the QW layers that also influences the Urbach parameter. The behavior of E_0 is comparable to the expected behavior of low temperature PL linewidths of QW structures and has the same physical origin, namely the broadening of the interband density of states by the non-uniformity of certain parameters. The Urbach parameter is proportional to kT [151]. A sharp absorption edge is represented by small E_0 values. In addition, aging also influences E_0. Assuming early stages of gradual degradation are accompanied by point defect creation, one could make them responsible for smoothing the Coulomb-potential of the quantum well, eventually resulting in an increasing Urbach parameter E_0 [27]. This statement implies a correlation between Urbach parameter and lifetime of QW devices. The correlation was shown in Ref. [34] with diode lasers operating at 1.3 μm. According to this result, the lifetime decreases 10 times when Urbach parameter increase by 20 %. Therefore, analysis of Urbach parameters can potentially also provide a lifetime prediction tool.

For the devices investigated here, we observed E_0-values of about 7.5 meV, 9.0 meV, and 8.5 meV for the groups of SC1, SC2, and SC3, respectively (see Fig. 5.16 dotted lines, solid lines and dashed lines, respectively). The samples from one batch have almost identical values (with a small error). The E_0 of the single QW – InGaP waveguide (SB1) is the smallest one. Surprisingly, the double QW of the InGaAsP

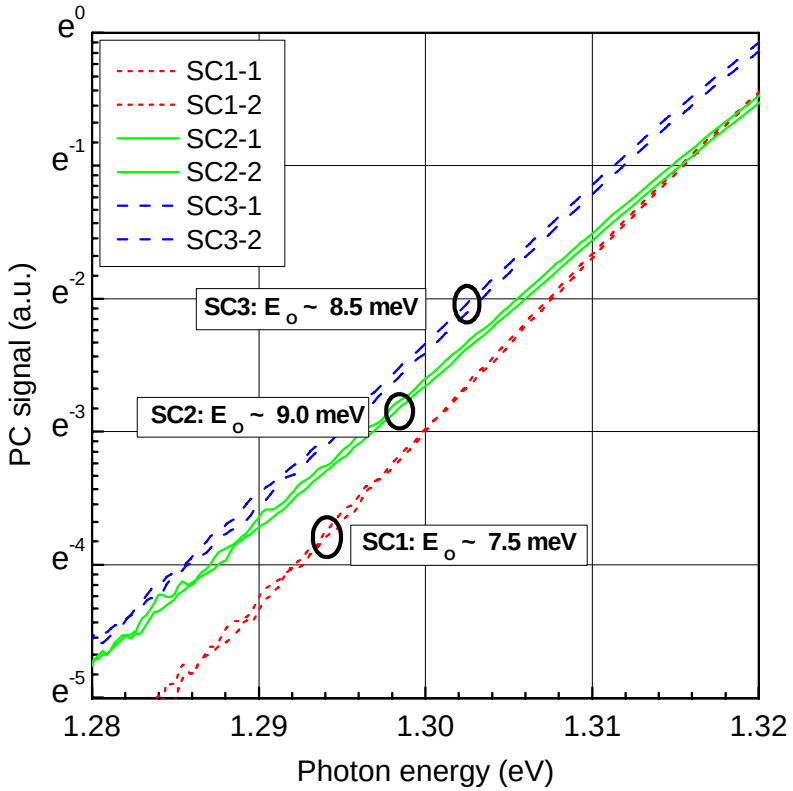

Figure 5.16:

Extraction of the Urbach parameter of Al-Free 915nm broad-area HPDLs from PC spectra: in Fig 5.15 (a): the Urbach-tail parameters E_0 obtained from the PCS spectra differ clearly and systematically from batch to batch. The corresponding E_0 values for batch SC1, SC2 and SC3 are 7.5, 8.5 and 9.0 meV, respectively. The best samples have the smallest E_0 - values. The samples from one batch have almost identical values

waveguide (SC3) shows a smaller E_0 than single QW one (SC2). That means the uniformity of the two QWs is better than the one of the single QW. However, the more important evidence that we want to emphasize here is the observation of early degradation of devices from the groups with a larger Urbach parameter. This shows a correlation between the Urbach parameter and the presence of degradation processes.

Chapter 6.

Interplay between strains and defects in high power diode lasers

The packaging induced strain is known as one major source of defect generation even in unaged HPLD bars [114,121]. Vice versa, defects created in HPLDs contribute to the internal strain within the laser structure [142]. Therefore, strain and defects are strongly correlated and both influence device reliability. In this chapter, we show some evidence for defect-strain relations that we observed in some particular devices. Afterwards, we will discuss the quantification of microscopic defects and an internal strain-defect relationship that show the link between different types of defects and internal strain.

6.1. Observation of stress (strain) – defect correlations

First we present results on the evolution observation of microscopic defects under external stress. The experiment was performed by applying artificial stress perpendicular to the QW plane of single HPLD chips. This stress is expected to generate external strain in the direction perpendicular to QW plane. At each stress magnitude, we collect one PC spectrum. The PC spectra for different external stress are shown in Fig. 6.1 (a) and (b) for representative single HPLD chips, namely SB1-2 and SB1-3. These chips can be considered as single emitters cleaved from regular 808 nm emitting HPLD bars and were described in section 2.2. The device SB1-2 contains a wide defect band that is already clearly visible in the PC spectrum with zero external stress in Fig 6.1 (a, solid curve). When external stress is applied to the chip, this defect

band shows a substantial enhancement. The enhancement grows further with increasing external stress. This behavior is typical for devices, where defects already exist inside the laser structure. The behavior of device SB1-3 is very different. In Fig. 6.1 (b), we can see that a defect band as observed for device SB1-3 is almost absent. When the external stress is increased the defect region below the QW absorption edge is nearly unchanged. Thus it seems that external stress increases the concentration of defects if they are already present. In turn, in nominally defect-free devices the creation of additional defects is less likely.

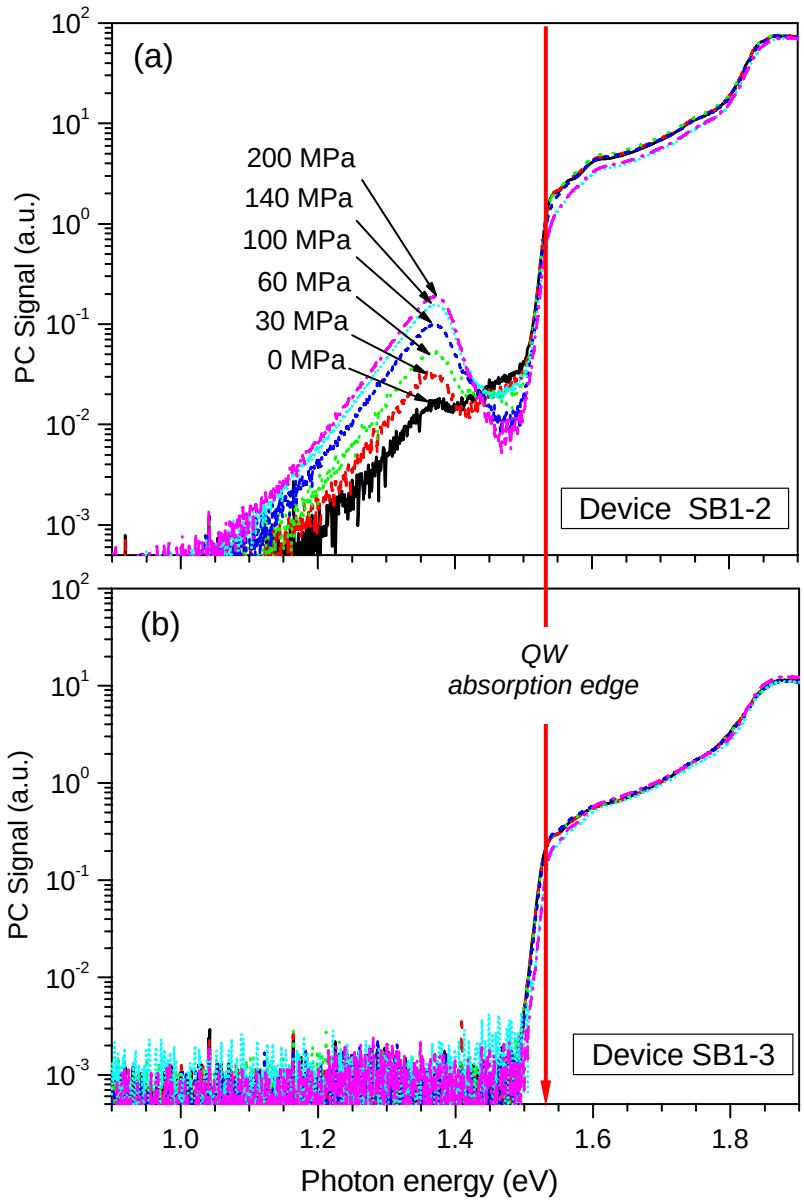

Figure 6.1:

PC spectra of a single 808 nm HPLD single chip SB1-2 (a) and single chip SB1-3 (b) measured at different external stress in z-axis perpendicular to the QW-plane. Device SB1-2 already contained a wide defect band, see solid line in (a). The defect band is significantly enhanced by increasing the external stress. While the device SB1-3 is defect-free before measurement. With the experiment condition similar to performing for device SB1-2, we do not see any defect bands below the QW absorption edge.

Second, we introduce a strain-defect relation for a 980 nm tapered HPLD bar that has already been analyzed in section 5.3.1 (device TB1-1). Besides performing an LBIC scan we did PC measurements. Fig. 6.2 (a) shows the spectral positions of the

hh1-e1 transitions extracted from PC spectra. This provides an estimate for the strain distribution versus local position inside the bar. Figure 6.2 (b) represents the LBIC pattern of the same device measured at a wavelength of 1064 nm, which allows for defect excitation. The most striking effect visible in Fig. 6.2 (a) is the substantial increase of compressive strain in the left part of the tapered bar that is indicated by the blue shift of the hh1-e1 transitions. The maximum of compression is located near u = 2 mm. This behavior was also observed for the waveguide transitions independently

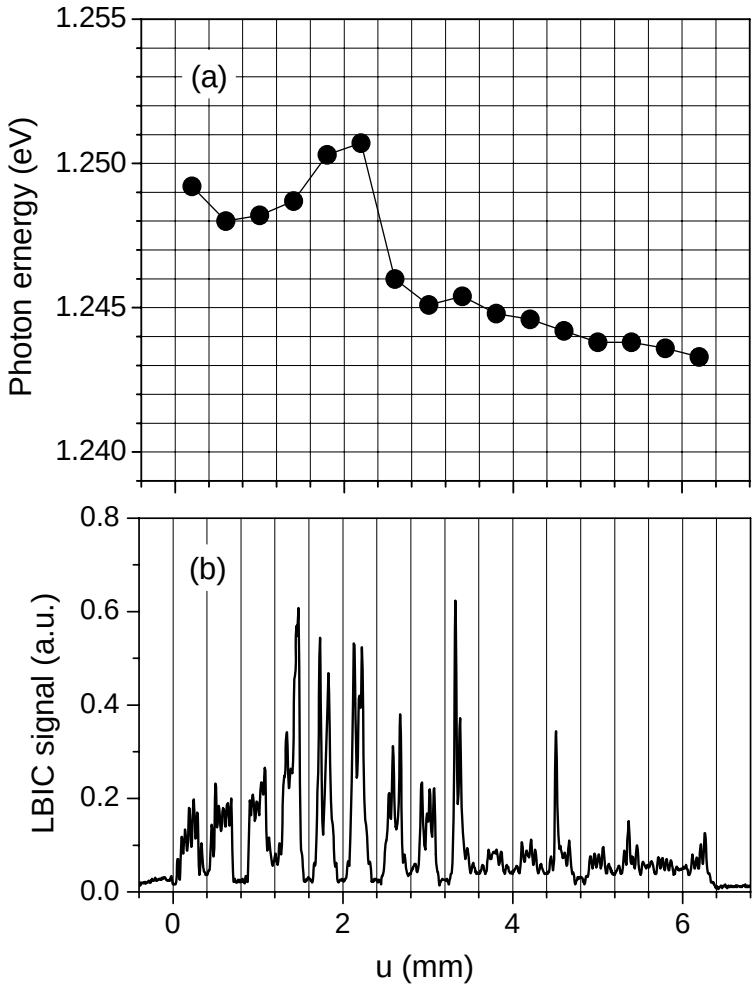

Figure 6.2:

(a) Spectral positions of the hh1-e1 transition of the 980 nm tapered HPLD bar TB1-1 along the device were extracted from PC spectra measured at the emitter centers.

(b) The LBIC scan of the tapered bar at 1064 nm excitation laser shows the defect distribution along the device

supporting the assignment of the observed shift to compressive strain. In the LBIC defect-scan in Fig. 6.2 (b), we can see a high defect concentration in the left-side of the tapered bar at the region with compressive strain in Fig 6.2 (a). The highest amount of defects is concentrated in the vicinity of u = 2 mm. This agrees well with the position where the strain maximum is located. The right-hand side of the device shows less pronounced defect bands corresponding to a lower amount of compressive strain. The facts indicate that the defect enhanced area (where the defects arise during the

operation) leads to compressive strain inside the bar. A similar effect was not observed in other devices that are of the same structure but contain a lower amount of defects.

Finally, in this section, we present another example for a strain - defect relation observed in the HPLD cm-bar BD-1 (sample description presented in section 2.2.5). The µPC result has been shown in section 5.2 (see Fig. 5.3). This result provides the information of defect enhancement in one emitter of the bar after 1500 h aging. Beside that, we are able to extract the strain distribution from µPC data for this particular emitter too. Fig. 6.3 shows the raw data for spectroscopic strain analysis at the considered emitter. The µPC data, [Fig. 6.3 (b)] represent the spectral positions of the hh1-e1 absorption transitions in the QW along the active region of the emitter before and after aging, whereas Fig. 6.3 (a) shows µPL data taken from traces along the substrate. Here we plot the PL peak position, which is influenced by both, the hh-e and the lh-e bulk transitions in the substrate. The parameter in this case is the depth of the

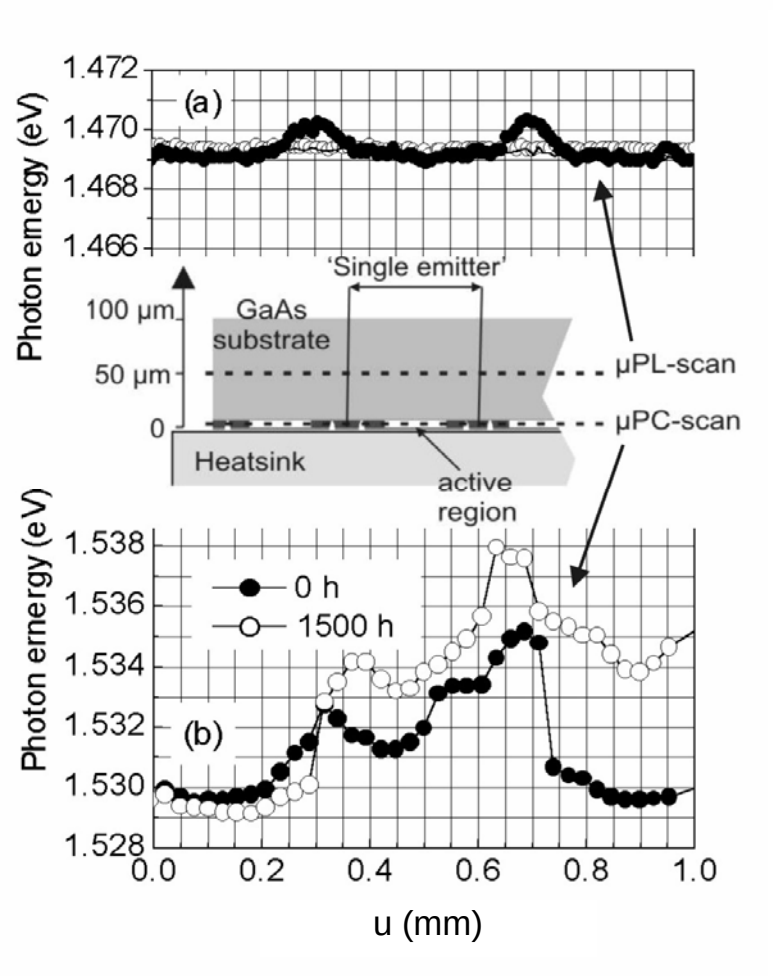

Figure 6.3:

Data obtained from spectroscopic strain analysis of device BD-1:

(a) µPL peak-positions extracted by fitting the luminescence spectra. The parameter is the distance of the scan path from the active region, cf. ordinate scale in the inset. Full circles indicate data measured at a trace 10 µm away from the active region, whereas open circles and the full line refer to data taken at 30 and 50 µm, respectively.

(b) Spectral positions of the hh1-e1 transitions in the QW along the emitter before and after 1500 h aging.

vertical position where the PL-scan was taken, i.e., the vertical distance of the PL-scan trace from the active region, cf. ordinate scale in the inset of Fig. 6.3. These data show a significant increase of the internal strain at the active region of the emitter where the defect photocurrent has been enhanced after operation. An interfering effect of

packaging-induced strain to these particular results is not very likely. First, the packaging on a Cu-W heat spreader is expected to minimize the packaging induced strain. Second, even packaging on a Cu heatsink causes a rather small gradient in such a small region as an emitter stripe that is considered here.

6.2. Quantification of defects and internal strain relationship

The discussion of this section is based on the data from the 808 nm HPLD cm-bar BD-1, which were presented in the preceding sections (5.2 and 6.1). First, we address the strain data. The quantitative analysis requires knowledge on the strain symmetry. Considering the limiting cases, i.e. uniaxial (along <110> direction) and hydrostatic pressure, a 1 meV blue shift corresponds to a compression by -0.048 % and -0.004 %, respectively. This calculation is based on the strain sensitivities provided in section 1.2.3. Thus the actual strain in the QW structure of HPLD bar must be in between these limits. In any case, the blue shifts always indicate the compression of the QW structure.

Note that in Fig. 6.3 (b) the peaks at 0.35 and 0.65 mm are caused by strain fields that are related to the groove regions with the insulating stripe between the single emitters. Such fields are already discussed in detail in section 3.4. For this particular case, they are not directly related to our analysis of the defective emitter. The vertical decay of these strain fields into the substrate is illustrated by the µPL data shown in Fig. 6.3 (a). The µPL peak-positions correspond to the maximum of the µPL spectra for each position. These maxima are extracted from the luminescence spectra using a 5th order polynomial fit. At a scanning position 10 µm into the substrate, see inset in Fig.6.3, the peaks are clearly visible, whereas at 30 µm almost nothing remains to be seen. Additionally, the µPL scans in Fig. 6.3 (a) clearly show that there are no residual strain fields in the substrate. This finding is important for our further discussion because it excludes the hypothesis of an impact of a dislocation line, e.g. related to a V-defect in the substrate [141], which might have caused the defect accumulation in the emitter.

With aging, a non-uniform strain behavior of the emitters in the array is observed; see Fig. 6.3 (b). The left emitter shows a rather typical behavior for such devices without defects [152], namely a slight relaxation of the compressive uniaxial packaging-induced stress, which results in an effective tension of the lattice (~ -0.5 meV shift corresponds here to +0.024 % lattice tension [see also the strain sensitivity in section 1.2.3]). Obviously, in the other two emitters (center and rightmost), this effect is highly overcompensated by lattice compression.

We now combine the available data on strain and defects for the central emitter. The complex shape of the wide defect band in Fig. 5.3 (a) already indicates that more

than one defect-to-(sub)-band transition might be effective. Furthermore, the large dynamic range of the defect absorption (more than 3 orders of magnitude as shown in Fig. 5.3) provides a sufficient decoupling of the contributions from various defects, which are easily distinguished by the absorption bands starting at different photon energies. We tentatively identify these onset photon energies as level depths similar to the discussion in section 5.3.2.

Fig. 6.4 provides the combination of the results on strain and defects of device BD-1. We divide the entire below-gap spectral region from 0.6 to 1.5 eV into 6 spectral channels and integrate the µPC signal within the corresponding channel. This signal, indicative for the defect density in this very channel, is shown as a function of the spectral position of the hh1-e1 transitions taking from strain analysis data at the corresponding local position in Fig 6.3 (b). This analysis was restricted to the region underneath the metallized emitter stripe of the central emitter, i.e. the region from 0.4 mm to 0.6 mm in Fig. 6.3 (b).

In Fig. 6.4, we see a completely different behavior of midgap levels (detected at channel of 0.6-0.9 eV), shallower deep levels (detected at channel of 1.2-1.3 eV), and shallow defects and band-tail states (detected at channel of 1.45-1.50 eV). It has to be stressed again that in this figure there are two parameters that contribute to the spread of the parameter strain, which is represented by the photon energy of the absorption peaks of the hh1-e1 transitions at the abscissa of Fig. 6.4 (c). First, this is the local position in the emitter stripe, where the spectrum was measured and, second, device operation time that substantially enhances the strain. From the results in Fig. 6.4, we conclude that:

- Device operation time increases the midgap-level concentration substantially; in the particular case of Fig. 6.4 (c) by a factor of 3. Generally, there is no correlation between the midgap-level concentration and the internal strain at various locations in the emitter.

- For transitions via shallow defects and band-tail states, the situation appears to be quite different; see Fig. 6.4 (a). The change in the internal strain is caused here by the co-action of two independent parameters, namely local position and device age. Remarkably, linear fits to both of data sets, the pristine and the aged devices result in nearly identical fit parameters; see Fig. 6.4 (a). From such a uniform strain-defect relationship, we conclude that the creation of shallow defects and band tail states is strongly correlated with the internal strain, regardless of its origin.

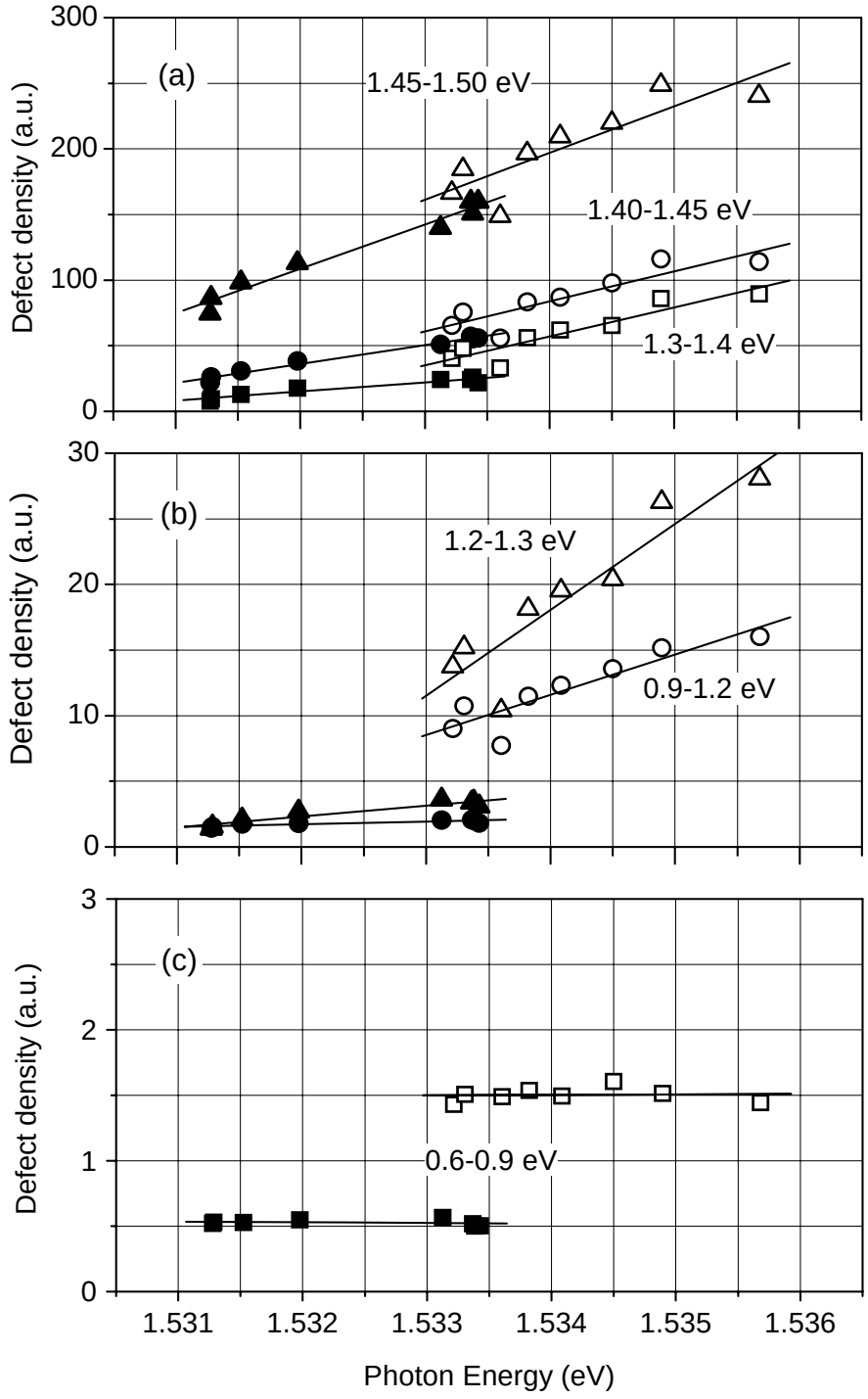

Figure 6.4: Local defect absorption versus local strain within the defect absorption range spectral channels are arbitrarily chosen. The plot shows the spread of the defect-related µPC signal for the different channels within one device emitter versus spectral positions of the hh1-e1 transitions (that quantify the strain) at the corresponding local position. Full symbols represent data obtained at 0 hours, open symbols mark data measured in the same spectral range after 1500 hours of operation. The analysis includes those local positions only, which are located underneath the metallized stripe of the central emitter (0.4-0.6 mm in Fig 6.3.b). The lines are linear fits to the corresponding data.

- One expects a linear defect relationship, such as the one in Fig. 6.4 (a), if strain fields grow due to subsequent defect creation. Thus, we consider the additional creation of shallow defects and band-tail states as the driving force for generation of hydrostatic pressure. In HPLDs there are other scenarios possible for defect creation, e.g., external stress similarly to the case of packaging-induced strain (that has been shown to generate defects, too) [121,153]. Under such circumstances even strain thresholds were observed in the process of defect creation, i.e. a non-linear behavior [154]. Our present results show clearly that even different strain-defect-relationships can coexist if different defects are created simultaneously by device operation.

In this chapter, we have studied the interplay between strain and the presence of defects in HPLDs. We have shown a correlation between strain and defect in some different types of HPLDs in different situations. We are able do distinguish between effects caused by physically different defects. By quantitative analysis, we can draw the following conclusions:

- for midgap levels as well as shallow defects and band tail states, which are assigned to physically different defects, distinctively different strain-defect relationships are observed;
- the concentration of shallow defects and band-tail states is strongly correlated to compressive strain in their vicinity, no matter how the strain is created;
- for midgap levels, in contrast, there is no straight correlation.

In this analysis, HPLD arrays serve as model devices, only. We think that the results can be extended to other GaAs-based materials and devices.

Summary

In this thesis, we use spectroscopic analysis as main methodology to investigate HPLDs. The devices under test include both types single emitters and laser diode arrays (bars and stacks); the wavelength ranges from the red to the near infrared region (650-1000 nm); and the geometry of structures are conventional (broad area) or tapered. In particular, we focus on results that come out of the application of photoelectrical techniques, namely, PC spectroscopy, LBIC and NOBIC. By using these spatially and spectrally resolved techniques and some complementary spectroscopic methods (e.g. PL and CL), we study issues that are related tightly to device reliability: strain, thermal tuning properties, defects, and interplay between strain and defects.

- In our study, strain analysis was performed in order to confirm theoretical calculations of the strain sensitivities of the spectral positions of the relevant quantum-confined optical transitions within particular QWs. Then this theoretical model has been applied to explain the strain phenomena observed after the packaging process and later during operation. The absolute strain values are quantified in each particular case. By analyzing the whole sequence of QW-transitions, we determine - up to a certain degree - even strain symmetry. The results that we achieve include:

  - Analysis of packaging-induced strains of HPLD arrays. For In-soldered cm-bars, which are packaged on Cu-heatsinks, the main component of this strain is uniaxial along the <110> direction.

  - Mechanical strain evolution during high power operation in In-soldered HPDL arrays, which are packaged on Cu-heatsinks. These results show relaxation process of the packaging- induced strain (strain reduction) after several hundred aging hours.

  - The observation and analysis of additional strain contributions in the immediate vicinity of grooves, which separate the emitter in laser diode arrays:

this strain contribution is closely associated with packaging-induced strain, but exhibits a biaxial in-plane symmetry.

- The comparison of the packaging-induced strains measured in center of the substrate and in the active region of high-brightness tapered laser diode bars shows: the strain is not relaxed from the center of substrate towards the active region in the center of the bars.

- A study on thermal tuning properties of HPDL arrays at typical operation temperatures is presented:

  - The analysis of experimental results provides values for the temperature dependence of the thermal tuning rate as well as separates the contributions caused by pressure tuning driven by the relaxation of compressive packaging-induced stress for increasing temperatures. The pressure tuning contribution is separated from actual thermal tuning rate.

  - The measurements performed for both standard and expansion-matched heat sinks [Cu (In-solder) and Cu-W (AuSn-solder)] show the improvement of the thermal tuning characteristics for expansion-matched heat sinks. We do not find any pressure tuning contribution in the tuning rate of devices packaged on expansion-matched heat sinks.

- Defects were also investigated by PC related techniques (PC spectroscopy, LBIC and NOBIC). Based on the application of these techniques, defects are localized and characteristic parameters are determined. The results involve:

  - The evolution of defects during device operation: A clear enhancement of defects is shown after certain running hours at devices containing “initial” defect before aging.

  - The distributions of defects along HPDL arrays: this tells us where the defect concentration is higher in all of lateral positions of the array. Based on this information, degradation areas can be identified and “weak points” of device designs are predicted.

  - The localization of deep level defects within waveguides of high-power red-emitting lasers was confirmed by NOBIC measurements. As a consequence, these defects, if present in high densities, can deteriorate device properties in a direct way.

  - Analysis of degradation in high-power laser diodes due to defect creation has been monitored by optical techniques. These results demonstrate clearly the efficiency of the LBIC technique (as a quick screening method) as well as PC spectroscopy for analyzing defects or imperfect epitaxial structures. Therefore both techniques display a certain potential for predicting device failure.

- Finally, we address the interplay between defects and strain in cm-bar high-power diode laser arrays. An enhancement of the concentration defect levels in single-emitters is observed for increasing of external stress. We are able do distinguish between effects caused by different defects. Midgap levels, shallow defects, and band tail states, the latter two of which are assigned to physically different defects, exhibit distinctively different strain-defect-relationships. The analysis shows a strong correlation between defect concentration and strain for shallow defect levels and no correlation to midgap defect levels. The study provides knowledge about defect creation scenarios, which help to identify bottlenecks in device design and technology.

Our approach applied for studying HPLDs can be extended to other semiconductor optoelectronic devices.

References

[1]. R. V. Steel, “Review and forecast of laser markets: 2005-Part II,” Laser Focus World, Vol. 41, No. 2, pp. 69-80, 2005.

[2]. R. V. Steel, “Review and forecast of laser markets: 2006-Part II,” Laser Focus World, Vol. 42, No. 2, pp. 52-72, 2006.

[3]. D. F. Welch, “A brief history of High-Power Semiconductor Lasers”, IEEE J. Select. Top. Quan. Electron., Vol. 6, No. 6, pp. 1470-1477, 2000.

[4]. http://www.jold.com.

[5]. Knigge, G. Erbert, J. Jönsson, W. Pittroff, R. Staske, B. Sumpf, M. Weyers and G. Tränkle, "Passively cooled 940 nm laser bars with 73 % wall-plug efficiency at 70 W and 25° C", Electronics Letters, Vol. 41, No. 5, pp. 250-251, 2005.

[6]. http://www.bright-eu.org.

[7]. G. Erbert, G. Beister, R. Hülsewede, A. Knauer, W. Pittroff, J. Sebastian, H. Wenzel, M. Weyers, G. Tränkle, "High-Power Highly Reliable Al-Free 940-nm Diode Lasers", IEEE J. Select. Top. Quan. Electron., Vol. 7, No. 2, pp. 143-148, 2001.

[8]. http://catalog.osram-os.com/media/_en/Graphics/00029998_0.pdf

[9]. B. Sumpf, M. Zorn, R. Staske, J. Fricke, P. Ressel, G. Erbert, M. Weyers, G. Tränkle, "High-efficient 650 nm laser bars with an output power of about 10 W and a wall-plug efficiency of 30%", Proc. SPIE 6133, pp. 78, 2006.

[10]. P. G. Eliseev, “Reliability Problems of Semiconductor Lasers”, Nova Science Publishers, Commack, 1991.

[11]. M. Fukuda, “Reliability and Degradation of Semiconductor Lasers and LEDs”, Artech House Inc., Boston, London, 1991.

[12]. O. Ueda, “Reliability and Degradation of III-V-Optical Devices”, Artech House Inc., Boston, London, 1996.

[13]. G. Bastard, “Wavemechanics applied to semiconductor heterostructures”, Les Editions de Physique and Halsted Press - Jonh Wiley & Sons Inc., 1988.

[14]. C. Weisbuch and B. Vinter, “Quantum Semiconductor Structures: Fundamental and Applications”, Academic Press, Inc., 1991.

[15]. F. T. Vasko and A. V. Kuznetsov, “Electronic States and Optical Transitions in Semiconductor Heterostructures”, Springer-Verlag New York, Inc. 1999.

[16]. P. K. Basu, “Theory of Optical Processes in Semiconductors: Bulk and Microstructures”, Oxford University Press Inc., 1997.

[17]. Bahaa. E. A. Saleh and M. C. Teich, “Fundamentals of Photonics”, John Wiley & Sons, Inc., 1991.

[18]. M. J. Kelly, “Low-Dimensional Semiconductors: Materials, Physics, Technology, Devices”, Oxford University Press, Inc., 1995.

[19]. A. Shik, “Quantum Wells: Physics and Electronics of Two-Dimensional Systems”, World Scientific Publishing Co. Pte. Ltd., 1997.

[20]. R. Dingle, W. Wiegmann, C. H. Henry, “Quantum state of Confined Carriers in very thin $Al_xGa_{1-x}As$ – GaAs - $Al_xGa_{1-x}As$ Heterostructures”, Phys. Rev. Lett. 33, pp. 827, 1974.

[21]. L. A. Coldren and S. W. Corzine, “Diode Lasers and Photonics Intergrated Circuits”, John Wiley & Sons, Inc., 1995.

[22]. H. J. Queisser and E. E. Haller, “Defects in semiconductors: Some Fatal, Some Vital”, Science, Vol. 281, pp. 945, 1998.

[23]. S. Adachi, Ed., “Properties of Aluminium Galium Arsenide”, INSPEC, the Institution of Electrical Engineers, London 1993.

[24]. F. Urbach, “The Long-Wavelength Edge of Photographic Sensitivity and of the Electronic Absorption of Solids”, Phys. Rev. 92, pp. 1324, 1953.

[25]. E. F. Schubert, “Doping in III-V Semiconductors”, Cambridge University Press, 1993.

[26]. G. Lucovsky, “On the photoionization of deep impurity centers in semiconductors” Sol. State Commun., 3, pp, 299, 1965.

[27]. J. W. Tomm, A. Bärwolff, A. Jaeger, T. Elsaesser, J. Bollmann, W. T. Masselink, A. Gerhard, and J. Donecker, “Deep level spectroscopy of high-power laser diode arrays” J. Appl. Phys. 84, pp. 1325, 1998.

[28]. W. Gärtner, “Depletion-Layer Photoeffects in Semiconductors”, Phys. Rev. 116, pp. 84, 1959.

[29]. A. Lopez and L. Anderson, “Photocurrent spectra of Ge-GaAs heterojunctions”, Solid-State Electron., 7, pp. 695, 1964.

[30]. J. Nelson, M. Paxman, K.W.J. Barnham, J. S. Roberts, and C. Button, "Steady state carrier escape from single quantum wells" IEEE J. Quan. Electron. 29, pp. 1460, 1993.

[31]. T. Kitatani, Y. Yazawa, S. Watahiki, K. Tamura, J. Minemura and T. Warabisako, “Photocurrent and Photoluminescence in InGaAs/GaAs Multiple Quantum Well Solar Cells”, Jpn. J. Appl. Phys. Vol. 35, pp. 4371, 1996.

[32]. C. H. Henry, P. M. Petroff, R. A. Logan, and F. R. Merrit, “Catastrophic damage of $Al_xGa_{1-x}As$ double heterostructure laser material” J. Appl. Phys. 50, pp. 3721, 1979.

[33]. J. W. Tomm, A. Bärwolff, Ch. Lier, T. Elsaesser F.X. Daiminger, and S. Heinemann, "Laser Based Facet Inspection System" SPIE Proc. 3000, pp. 90, 1997.

[34]. J. W. Tomm, A. Gerhardt, D. Lorenzen, P. Hennig, H. Roehle, "Diode laser testing by taking advantage of its photoelectric properties" SPIE Proc. 4648, pp. 9, 2002.

[35]. Colace, A. DiVergilio, S. Vaidyanathan, T. P. Pearsall, H. Presting and E. Kasper, "PCS measurements of Si-Ge alloys and superlattices",Appl. Surf. Sci. 102, pp. 272, 1996.

[36]. P. T. Landsberg, "Recombination in semiconductors", Cambridge Univ. Press, 1991.

[37]. C. Kittel, "Introduction to Solid State Physics", 3rd Ed., John Wiley & Sons, Inc., 1967.

[38]. T. Numai, "Fundamental of semiconductor lasers", Springer-Verlag, NewYork, Inc., 2004.

[39]. S. Adachi, "Physical Properties of III-V semiconductor compounds", John Wiley & Sons, Inc., 1992.

[40]. G. E. Pikus and G. L. Bir, "Effect of deformation on the hole energy spectrum of germanium and silicon", Sov. Phys.-Solid State. 1, pp. 1502, 1960.

[41]. J. M. Luttinger and W. Kohn, "Motion of Electrons and Holes in Perturbed Periodic Fields", Phys. Rev. 97, pp. 869, 1955.

[42]. L. D. Laude, F. H. Pollak, and M. Cardona, "Effects of Uniaxial Stress on the Indirect Exciton Spectrum of Silicon", Phys. Rev. B 3, pp. 2623, 1971.

[43]. T. B. Bahder, "Eight-band k•p model of strained zinc-blende crystals", Phys. Rev. B 41, pp. 11992, 1990.

[44]. D. D. Nolte, W. Walukiewicz, and E. E. Haller, "Band-edge hydrostatic deformation potentials in III-V semiconductors", Phys. Rev. Lett. 59, pp. 501, 1987.

[45]. S. Adachi, "Material parameters of $In_{1-x}Ga_xAs_yP_{1-y}$ and related binaries", J. Appl. Phys. 53, pp. 8775, 1982.

[46]. S. Adachi, "GaAs, AlAs, and $Al_xGa_{1-x}As$ Material parameters for use in research and device applications", J. Appl. Phys. 58, pp. 3274, 1985.

[47]. Landolt-Börnstein, in Numerical Data and Function Relationships in Science and Technology, edited by O. Madelung, Vols. 17a and 22a, New Series, Group III. Spring-Verlarg, Berlin, 1982.

[48]. S. L. Chuang, "Physics of Optoelectronic Devices", John Wiley & Sons, NewYork, 1996.

[49]. D. L. Smith and C. Mailhiot, "k•p theory of semiconductor superlattice electronic structure. I. Formal Theory", Phys. Rev. B 33, pp. 8345, 1986.

[50]. P. O. Löwdin, "A note on the quantum-mechanical perturbation theory", J. Chem. Phys. 19, pp. 1396, 1951.

[51]. J. N. Schulman and Y. C. Chang, "Band mixing in semiconductor superlattices", Phys. Rev. B 31, pp. 2056, 1985.

[52]. M. L. Biermann, S. Duran, K. Peterson, A. Gerhardt, J. W. Tomm, A. Bercha and W. Trzeciakowski, "Spectroscopic method of strain analysis in semiconductor, quantum-well devices", J. Appl. Phys. 96, pp. 4056, 2004.

[53]. T. H. Stievater, W. S. Rabinovich, D. Park, P. G. Goetz, J. B. Boos, D. S. Katzer, M. L. Biermann, S. Kanakaraju and L. C. Calhoun, "Strain relaxation, band structure deformation, and optical absorption in free-hanging quantum well microstructures", J. Appl. Phys., 97, pp. 114326, 2005.

[54]. C. Mailhiot and D. L. Smith, "k•p theory of semiconductor superlattice electronic structure. II. Application to $Ga_{1-x}In_xAs$-$Al_{1-y}In_yAs$ [100] superlattices", Phys. Rev. B 33, pp. 8360, 1986.

[55]. C. Mailhiot and D. L. Smith, "Electronic structure of [001]- and [111]-growth-axis semiconductor superlattices", Phys. Rev. B 35, pp. 1242, 1987.

[56]. I. Vurgaftman, J. R. Meyer and L. R. Ram-Mohan, "Band parameters for III-V compound semiconductors and their alloys", J. Appl. Phys. 89, pp. 5815, 2001.

[57]. D. A. B. Miller, D. S. Chemla, T. C. Damen, A. A. Gossard, W. Wiegmann, T. H. Wood and C. A. Burrus, "Band-Edge Electroabsorption in Quantum Well Structures: The Quantum-Confined Stark Effect", Phys. Rev. Lett. 53, pp. 2173, 1984.

[58]. J. W. Tomm, A. Gerhardt, R. Müller, M. L. Biermann, Joseph P. Holland, Dirk Lorenzen, and Eberhard Kaulfersch, "Quantitative strain analysis in AlGaAs-based devices", Appl. Phys. Lett. 82, pp. 4193, 2003.

[59]. G. Rau, A. R. Glanfield, P. C. Klipstein, N. F. Johnson, and G. W. Smith, "Optical properties of $GaAs/Al_{1-x}Ga_xAs$ quantum wells subjected to large in-plane uniaxial stresss", Phys. Rev. B 60, pp. 1900, 1999.

[60]. M. L. Biermann, J. Diaz-Barriga, and W. S. Rabinovich, "Enhanced optical polarization anisotropy in quantum wells under anisotropic tensile strain", J. of Quantum Electron. 39, pp. 401, 2003.

[61]. G. Rau, P. C. Klipstein, V. Nikos Nicopoulos, and N. F. Johnson, "Analytic solutions for the valence subband mixing at the zone center of a $GaAs/Al_xGa_{1-x}As$ quantum well under uniaxial stress perpendicular to the growth direction", Phys. Rev. B 54, pp. 5700, 1996.

[62]. H. Qiang, Fred H. Pollak, C. Mailhiot, G. D. Pettit and J. M. Woodall,

"Uniaxial stress study of the quantum transitions in a strained layer (001) $In_{0.21}Ga_{0.79}As/GaAs$ single quantum well", Surf. Sci. 267, pp. 103, 1992.

[63]. H. Qiang, Fred H. Pollak, R. N. Sacks, "Piezospectroscopy of a $GaAs/Ga_{0.73}Al_{0.27}As$ single quantum well structure: Piezoelectric effects", Solid State Comm. 84, pp. 51, 1992.

[64]. H. Qiang, Fred H. Pollak, C. Mailhiot, G. D. Pettit and J. M. Woodall, "Externally generated piezoelectric effect in semiconductor micro- structures", Phys Rev. B 44, pp. 9126, 1991.

[65]. E. P. O'Reilly, "Valence band engineering in strained-layer structures", Semicon. Sci. Tech. 4, pp. 121, 1989.

[66]. M. L. Biermann and W. S. Rabinovich, "Double polarization anisotropy in asymmetric, coupled quantum wells under anisotropic, inplane strain", Opt. Express, 10, pp. 1105, 2002.

[67]. U. Zeimer, J. Grenzer, T. Baumbach, D. Lübbert, A. Mazuelas, and G. Erbert, "Strain and temperature distribution in broad-area high-power laser diodes under operation determined by high resolution X-ray diffraction and topography", Material Science and Engineering, B 80, pp. 87, 2001.

[68]. Z.-H. Cai, W. Rodrigues, P. Ilinski, D. Legnini, B. Lai, W. Yun, E. D. Isaacs, K. E. Lutterodt, J. Grenko, R. Glew, S. Sputz, J. Vandenberg, R. People, M. A. Alam, M. Hybertsen, and L. J. P. Ketelsen, "Synchrotron x-ray microdiffraction diagnostics of multilayer optoelectronic devices", Appl. Phys. Lett. 75, pp. 100, 1999.

[69]. De Wolf, "Micro-Raman spectroscopy to study local mechanical stress in silicon integrated circuits" Semicon. Sci. Tech. 11, No. 2, pp. 139, 1996.

[70]. Atkinson, S. C. Jain, "Spatially resolved stress analysis using Raman spectroscopy", J. Raman Spec. 30, Iss. 10, pp. 885, 1999.

[71]. J. W. Tomm, E. Thamm, A. Bärwolff, T. Elsaesser, J. Luft, M. Baeumler, S. Mueller, W. Jantz, I. Rechenberg, and G. Erbert "Facet Degradation of High-Power Diode Laser Arrays" Appl. Phys. A 70, pp. 377, 2000.

[72]. S. Perkowitz, "Optical Characterization of Semiconductor: Infrared, Raman and Photoluminescence Spectroscopy", Academic Press, 1993.

[73]. A. V. Andrianov, S. R. A. Dods, J. Morgan, J. W. Orton, T. M. Benson, I. Harrison, and E. C. Larkins, F. X. Daiminger, E. Vassilakis and J. P. Hirtz, "Optical and photoelectric study of mirror facets in degraded high power AlGaAs 808 nm laser diodes", J. Appl. Phys 87, Iss. 7, pp. 3227, 2000.

[74]. R. Xia, H. Xu, I. Harrison, B. Beaument, A. Andrianov, S. R. A. Dods, J. M. Morgan and E. C. Larkins, "Spectrally resolved electroluminescence microscopy and μ-electroluminescence investigation of GaN-based LEDs", J. Crys. Grow. 230, Iss. 3-4, pp. 467, 2001.

[75]. A. Klehr, G. Beister, G. Erbert, A. Klein, J. Maege, I. Rechenberg, J. Sebastian, H. Wenzel, and G. Tränkle, "Defect recognition via longitudinal mode analysis of high power fundamental mode and broad area edge emitting laser diodes", J. Appl. Phys. 90, Iss. 1, pp. 43, 2001.

[76]. R. Xia, A.V. Adrianov, S. Bull, I. Harrison, J.P. Landesman, E.C. Larkins, "Micro-electroluminescence spectroscopy investigation of mounting-induced strain and defects on high power GaAs/AlGaAs laser diodes", Opt. Quan. Electron. 35, pp. 1099, 2003.

[77]. S. Bull, A. V. Andrianov, I. Harrison, M. Dorin, R. B. Kerr, J. Noto, E. C. Larkins, "A spectroscopically resolved photo- and electroluminescence microscopy technique for the study of high-power and high-brightness laser diodes", IEEE Trans. Ins. Meas. 54, Iss. 4, pp. 1079, 2005.

[78]. B. G. Yacobi and D. B. Holt, "Cathodoluminescence scanning electron microscopy of semiconductors", J. Appl. Phys. 59, Iss. 4, pp. R1-R24, 1986.

[79]. O. Martínez, M. Avella, J. Jiménez, B. Gérard, R. Cuscó and L. Artús, "Optical properties of epitaxial lateral overgrowth GaN structures studied by Raman and cathodoluminescence spectroscopies", J. Appl. Phys. 96, Iss. 7, pp. 3639, 2004.

[80]. K. Chin, H. Temkin, and R. J. Roedel, "Transmission cathodoluminescence: A new SEM technique to study defects in bulk semiconductor samples", Appl. Phys. Lett. 34, Iss. 7, pp. 476, 1979.

[81]. M. Pommiès, M. Avella, E. Cánovas, J. Jiménez, T. Fillardet, M. Oudart and J. Nagle, "Cation intermixing at quantum well/barriers interfaces in aged AlGaAs-based high-power laser diodes bars", Appl. Phys. Lett. 86, pp. 131103, 2005.

[82]. T. Q. Tien, A. Gerhardt, S. Schwirzke-Schaaf, J. W. Tomm, M. Pommiès, M. Avella, J. Jiménez, M. Oudart, and J. Nagle, "Screening of high-power diode laser bars by optical scanning" , Appl. Phys. Lett. 87, pp. 211110, 2005.

[83]. A. Kozlowska, M. Latoszek, J. W. Tomm, F. Weik, T. Elsaesser, M. Zbroszczyk, M. Bugajski, B. Spellenberg and M. Bassler "Analysis of thermal images from diode lasers: Temperature profiling and reliability screening" Appl. Phys. Lett. 86, pp. 203503, 2005.

[84]. A. Kozlowska, P. Wawrzyniak, J. W. Tomm, F. Weik, and T. Elsaesser, "Deep level emission from high-power diode laser bars detected by multi-spectral infrared imaging", Appl. Phys. Lett. 87, pp. 153503, 2005.

[85]. B. L. Meadows, F. Amzajerdian, N. R. Baker, V. Sudesh, U. N. Singh, and M. J. Kavaya, "Thermal characteristics of high power long-pulsewidth quasi-CW laser diode arrays", Proceeding of SPIE Vol. 5336, pp. 203, 2004.

[86]. A. L. Moretti, F.A. Chambers, F.A.; Devane, G.P.; Kish, F.A, **"**Characterization of GaAs/$Al_xGa_{1-x}As$ structure using scanning photoluminescence", IEEE, J. Quantum Electron. 25, pp. 1018, 1989.

[87]. H. P. Lee et. al., In Heteroepitaxy on Silicon: Fundamental, Structures and devices, Materials Research Society Symposia Proc. 116, Pittburg: Material Research Society, pp. 219, 1988.

[88]. E. C. Lightowlers, In Growth and Characterization of Semiconductors (R. A. Stradling and P. C. Klipstein, eds), Bristol: Adam Hilger, pp. 135, 1990.

[89]. V. Saptari, "Fourier-Transform Spectroscopy Instrumentation Engineering", SPIE Press, 2004.

[90]. J. W. Tomm, T. Günther, Ch. Lienau, A. Gerhardt, and J. Donecker, "Near-field Photocurrent Spectroscopy of Laser Diode Devices", J. Cryst. Growth 210, pp. 296, 2000.

[91]. C. Ropers, T. Q. Tien, Ch. Lienau, and J. W. Tomm, P. Brick, N. Linder, B. Mayer, M. Müller, S.Tautz, and W. Schmid, "Observation of deep level defects within the waveguide of red-emitting high-power diode lasers", Appl. Phys. Lett. 88. pp. 133513, 2006.

[92]. A. Richter, Ch. Lienau and J.W. Tomm "Wave Guide Effect on the Image Formation Process in Near-Field Photocurrent Spectroscopy of Semiconductor Laser Diodes" Surface and Interface Analysis 25, pp. 573, 1997.

[93]. P. Martin, J. P. Landesman, E. Martin, A. Fily, J. P. Hirtz, R. Bisaro, "Microphotoluminescence mapping of packaging-induced stress distribution in high-power AlGaAs laser diodes", SPIE 3945, pp. 308, 2000.

[94]. E. Martin, J. P. Landesman, J. P. Hirtz and A. Fily , "Microphotoluminescence mapping of packaging-induced stress distribution in high-power AlGaAs laser diodes", Appl. Phys. Lett. 75, 17, pp. 2521, 1999.

[95]. D.T. Cassidy, "Spatially-resolved and polarisation-resolved photoluminescence for the study of dislocations and strain in III-V materials", Mater. Sci. Eng., B91-92, pp. 2, 2002.

[96]. B. Lakshmi, D. T. Cassidy, and B. J. Robinson, "Quantum-well strain and thickness characterization by degree of polarization", J. Appl. Phys. 79, issu.10, pp.7640, 1996.

[97]. J. W. Tomm, T. Q. Tien, and D. T. Cassidy, "Spectroscopic strain measurement methodology: Degree-of-polarization photoluminescence vs. photocurrent spectroscopy" , Appl. Phys. Lett. 88, pp. 133504, 2006.

[98]. G. Erbert, A. Bärwolff, J. W. Tommt, "High-power broad-area diode lasers and laser bars", Topics in Applied Physics Vol. 78, pp. 173, Springer-Verlag, Berlin, 2000.

[99]. http://www.fbh-berlin.de

[100]. M. Weyers et al, “Epitaxy of High-power diode laser structures”, Topics in Applied Physics Vol. 78, pp. 83, Springer-Verlag, Berlin, 2000.

[101]. J. W. Tomm, A. Bärwolff, T. Elsaesser, and J. Luft „Selective excitation and photoinduced bleaching of defects in InAlGaAs/GaAs high-power diode lasers“ Appl. Phys. Lett. 77, pp. 747, 2000.

[102]. J. W. Tomm and J. Jimenez, “Quantum-Well Laser Array Packaging: Nanoscale Packaging Techniques”, The McGraw-Hill Companies, New York, 2006.

[103]. K. A. Williams, R. V. Penty, I. H. White, D. J. Robbins, F. J. Wilson, J. I. Lewandowski, B. K. Nayar, “Design of high-brightness tapered laser arrays”, IEEE J. Select. Top. Quan. Electron., Vol. 5, No. 3, pp. 822, 1999.

[104]. M. Mikulla, “Tapered High-power, High-Brightness diode lasers: Design and Performance”, Topics in Applied Physics Vol. 78, pp. 265, Springer-Verlag, Berlin, 2000.

[105]. S. Sujecki, L. Borruel, J. Wykes, P. Moreno, B. Sumpf, P. Sewell, H. Wenzel, T. M. Benson, G. Erbert, I. Esquivias, E. C. Larkins, “Nonlinear properties of tapered laser cavities”, IEEE J. Select. Top. Quan. Electron., Vol. 9, No. 3, pp. 823, 2003.

[106]. L. Borruel, I. Esquivias, P. Moreno, M. Krakowski, S. Ch. Auzanneau, M. Calligaro, O. Parillaud, M. Lecomte, S. Sujecki, J. Wykes, E. C. Larkins, “Clarinet laser: Semiconductor laser design for high-brightness applications”, Appl. Phys. Lett. 87, pp. 101104, 2005,

[107]. N. Michel et al.: Tapered high-brightness laser design for WWW.BRIGHT.EU project.

[108]. G. Erbert, J. Fricke, R. Hülsewede, A. Knauer, W. Pittroff, P. Ressel, J. Sebastian, B. Sumpf, H. Wenzel and G. Tränkle, "3 W - high brightness tapered diode lasers at 735 nm based on tensile strained GaAsP-QWs", Proceedings of SPIE Vol. 4995, pp.29, 2003.

[109]. Database from Fraunhofer Institute IAF (see http://www.iaf.fraunhofer.de/)

[110]. http://www.eagleyard.com/products/packages.php

[111]. P. Loosen, “Cooling and Packaging of High-power diode lasers”, Topics in Applied Physics Vol. 78, pp. 289, Springer-Verlag, Berlin, 2000.

[112]. M. Behringer, M. Philippens, W. Teich, A. Schmitt, S. Morgott, J. Heerlein, G. Herrmann, J. Luft, G. S., J. Biesenbach, T. Brand, and M. Marchiano, “More brilliance from high-power laser diodes”, Proc. SPIE 4993, pp. 68, 2003.

[113]. S. C. Jain, M. Willander, and H. Maes, “Stresses and strains in epilayers, stripes and quantum structures of III - V compound semiconductors”, Semicon. Sci. Tech. 11, pp 641, 1996.

[114]. J. W. Tomm, R. Müller, A. Bärwolff, T. Elsaesser, A. Gerhardt, J. Donecker, D. Lorenzen, F. X. Daiminger, S. Weiß, M. Hutter, E. Kaulfersch, and H. Reichl, “Spectroscopic measurement of packaging-induced strains in quantum-well laser diodes“ J. Appl. Phys. 86, pp. 1196, 1999.

[115]. S. Kasap and P. Capper (Eds.), Handbook of Electronic and Photonic Materials, Springer Science+Business Media Inc., 2006.

[116]. http://www.ioffe.rssi.ru/

[117]. http://www.matweb.com/

[118]. R.T.Collins, L. Vina, W. I. Wang, L. L. Chang, L. Esaki, K. v. Klitzing and K. Ploog, “Mixing between heavy hole and light hole and light hole excitation in GaAs/AlGaAs quantum well in electric field”. Phys. Rev. B36, pp. 1531, 1986.

[119]. M. Biermann et al. (University of Eastern Kentuckey, USA): Theoretical calculation of Electronic band structure for Single QW and Double QW of GaAs-based structures (unpublished).

[120]. J. W. Tomm, R. Müller, A. Bärwolff, T. Elsaesser, D. Lorenzen, F. X. Daiminger, A. Gerhardt, and J. Donecker “Direct spectroscopic measurement of thermally induced strain in high-power optoelectronic devices” Appl. Phys. Lett. 73, pp. 3908, 1998.

[121]. J. W. Tomm, A. Gerhardt, T. Elsaesser, D. Lorenzen, and P. Hennig, ”Simultaneous quantification of strain and defects in high-power diode laser devices”, Appl. Phys. Lett. 81, pp. 3269, 2002.

[122]. J. W. Tomm, A. Gerhardt, R. Müller, V. Malyarchuk, Y. Sainte-Marie, P. Galtier, J. Nagle, and J.-P. Landesman, "Spatially resolved spectroscopic strain measurements on high-power laser diode bars", J. Appl. Phys. 93, pp.1354, 2003.

[123]. P.D. Colbourne and D. T. Cassidy, “Imaging of stresses in GaAs diode lasers using polarization-resolved photoluminescence”, IEEE. J. Quant. Electron. 29 pp. 62, 1993.

[124]. D.T. Cassidy, S.K.K. Lam, B. Lakshmi, and D.M. Bruce, “Strain Mapping by Measurement of the Degree of Polarization of Photoluminescence”, Appl. Opt. 43, pp. 1811, 2004.

[125]. Z. Huang, P. Crump, T. R. Crum, M. A. DeVito, J. Farmer, M. Grimshaw, Scott A. Igl., S. Macomber, “High-power long-wavelength (1.4 to 1.5 μm) laser array and stacked arrays”, Proc. SPIE Vol. 5336, pp. 188, 2004.

[126]. A. Baliga, D. Trivedi and N. G. Anderson, "Tensile-strain effects in quantum-well and superlattice band structures", Phys. Rev. 49, pp.10402, 1994.

[127]. A. Gerhardt, F. Weik, Tien QuocTran, J. W. Tomm, T. Elsaesser, J. Biesenbach, H. Müntz, G. Seibold, and M. L. Biermann "Device deformation during low-frequency pulsed operation of high-power diode bars" , Appl. Phys. Lett. 84, pp. 3525, 2004.

[128]. G. L. Harnagel, P. S. Cross, D. R. Scifres, D. F. Welch, C. R. Lennon, D. P. Worland, and R. D. Burnham, "High-power quasi-cw monolithic laser diode linear arrays", Appl. Phys. Lett. 49, pp.1418, 1986.

[129]. A. Borowiec, D. M Bruce, Daniel T. Cassidy, and H. K. Haugen, "Imaging the strain fields resulting from laser micromachining of semiconductors", Appl. Phys. Lett. 83, pp. 225, 2003.

[130]. T. Sugaya, K. Y. Jang, T. Wada, M. Ogura, K. Komori, "V-grooved InGaAs quantum-wire FET fabricated under an As_2 flux in molecular beam epitaxy", Proc. Molecular Beam Epitaxy International Conference, pp.133, 2002.

[131]. J. W. Tomm et al.(Max-Born Institute), Results of POWERPACK - European Union project (2004)

[132]. T. Q. Tien, A. Gerhardt, Sandy Schwirzke-Schaaf, Jens W. Tomm, Holger Müntz, Jens Biesenbach, Myriam Oudart, Julien Nagle, and Mark L. Biermann "Relaxation of packaging-induced strains in AlGaAs-based high-power diode laser arrays" Appl. Phys. Lett. 86, pp. 101911, 2005.

[133]. M. E. Klein, D.-H. Lee, J.-P. Meyn, K.-J. Boller, and R. Wallenstein, "Singly resonant continuous-waveoptical parametric oscillator pumped by a diode laser", Optics Letters, Vol. 24, Issue 16, pp. 1142, 1999.

[134]. D. J. M. Stothard, M. Ebrahimzadeh, and M. H. Dunn, "Low-pump-threshold continuous-wave singly resonant optical parametric oscillator", Optics Letters, Vol. 23, Issue 24, pp. 1895, 1998.

[135]. J.W. Tomm, F. Weik, A. Gerhardt, T.Q. Tran, J. Biesenbach ,H. Müntz, and G. Seibold "Transient thermal tuning properties of single emitters in actively cooled high-power cm-bar arrays" , SPIE Proc. 5336, pp. 125, 2004.

[136]. D. Lorenzen, "Methoden zur zuverlässigkeítsorientierten Optimierung der Aufbau- und Verbindungstechnik von Hochleistungs-Diodenlaserbarren", pp. 152, PhD thesis, Technical University Berlin, Verlag Dr. Köster, Berlin, 2003.

[137]. M. Kreissl, T. Q. Tien, J. W. Tomm, D. Lorenzen, A. Kozlowska, M. Latoszek, M. Oudart, and J. Nagle, "Spatially-resolved and temperature-dependent thermal tuning rates of high-power diode laser arrays" , Appl. Phys. Lett. 88. pp. 133510, 2006.

[138]. D. Lorenzen, M. Schröder, J. Meusel, P. Hennig, H. König, M. Philippens, J. Sebastian and R. Hülsewede, "Comparative performance studies of Indium and gold-tin packaged diode laser bars", SPIE Proc. Vol 6104, pp. 30, 2006.

[139]. J. W. Tomm , A. Jaeger, A. Bärwolff, T. Elsaesser, A. Gerhardt, J. Donecker, "Aging Properties of High Power Laser Diode Arrays Analyzed by Fourier-Transform Photo-Current Measurements", Appl. Phys. Lett. 71, pp. 2233, 1997.

[140]. J. W. Tomm, R. Müller, A. Bärwolff, T. Elsaesser, A. Gerhardt, and J. Donecker, D. Lorenzen, and F. X. Daiminger, S. Weiß, M. Hutter, E. Kaulfersch, and H. Reichl, "Spectroscopic measurement of packaging-induced strain in quantum-well laser diodes", J. Appl. Phys. 86, pp. 1196, 1999.

[141]. J.P. Landesman, "Micro-photoluminescence for visualisation defects, stress and temperature profiles in high-power III-V's devices", Materials Science and Engineering B91-92, pp. 55, 2002.

[142]. T. Q. Tien, J.W. Tomm, M. Oudart and J. Nagle "Mechanical strain and defect distributions in GaAs-based diode lasers monitored during operation", Appl. Phys. Lett. 86, pp. 111908, 2005.

[143]. A. Kozlowska, P. Wawrzyniak, A. Malag, M. Teodorczyk, J. W. Tomm, and F. Weik, "Reliability screening of diode lasers by multi-spectral infrared imaging", J. Appl. Phys. 99, pp. 053101, 2006.

[144]. Ch. Lienau, A. Richter, and J.W. Tomm "Near-Field Photocurrent Spectroscopy: A Novel Technique for Studying Defects and Aging in High-Power Semiconductor Lasers" Applied Physics A 64, pp. 341, 1997.

[145]. W.Shockley and W.T. Read, "Statistics of the Recombinations of Holes and Electrons", Phys. Rev. 87, pp. 835, 1952.

[146]. R. N. Hall "Electron-Hole recombination in Germanium" Phy. Rev. 87, pp. 387, 1952.

[147]. M. Pommiès, M. Avella, G. Patriarche, M. Bettiati, G. Hallais, J. Jiménez, "**E**ffect of the p(+)-GaAs contact layer doping level on the gradual degradation of InGaAs/AlGaAs pump lasers", Eur. Phys. J. Appl. Phys. 27, pp. 465, 2004.

[148]. O. Martinez, M. Avella, J. Jimenez, B. Gerard, R. Cusco and L. Artus, "Optical properties of epitaxial lateral overgrowth GaN structures studied by Raman and cathodoluminescence spectroscopies", J. Appl. Phys. 96, pp. 3639, 2004.

[149]. M. Pommiès, M. Avella, E. Cánovas, J. Jiménez, T. Fillardet, M. Oudart, and J. Nagle, "Cation intermixing at quantum well/barriers interfaces in aged AlGaAs-based high-power laser diodes bars"**,** Appl. Phys. Lett. 86, pp. 131103, 2005.

[150]. J. Jiménez, E. Cánovas, M. Avella, "Spectroscopic techniques for the assessment of optoelectronic materials: application to laser diodes", Eur. Phys. J.: Appl. Phys. 27, pp. 67, 2004.

[151]. S. R. Johnson and T. Tiedje, “Temperature dependence of the Urbach edge in GaAs”, J. Appl. Phys. 78, pp. 5609, 1995.

[152]. J. W. Tomm, “Probing Diode Lasers with Light - Photocurrent Reveals Information on Defects and Strain in Optoelectronic Devices”, LEOS Newsletter 13, pp. 20, 1999.

[153]. P.W. Epperlein, A. Fried and A. Jakubowicz, “Stress-induced defects in GaA quantum well lasers”, Inst. Phys. Conf. Ser. 112, pp. 567, 1990.

[154]. R. Xia, E. C. Larkins, I. Harrison, S. R. A. Dods, A. V. Andrianov, J. Morgan and J. P. Landesman, “Mounting-induced strain threshold for degradation of high-power AlGaAs laser bars”, Photon. Tech. Lett. 14, pp. 893, 2002.

List of publications

Publication in conjunction with this thesis

[1]. Axel Gerhardt, Fritz Weik, Tien QuocTran, Jens W. Tomm, Thomas Elsaesser, Jens Biesenbach, Holger Müntz, Gabriele Seibold, and Mark L. Biermann "Device deformation during low-frequency pulsed operation of high-power diode bars" , Appl. Phys. Lett. 84, 3525-3527(2004).

[2]. Tran Quoc Tien, Axel Gerhardt, Sandy Schwirzke-Schaaf, Jens W. Tomm, Holger Müntz, Jens Biesenbach, Myriam Oudart, Julien Nagle, and Mark L. Biermann "Relaxation of packaging-induced strains in AlGaAs-based high-power diode laser arrays" , Appl. Phys. Lett. 86, 101911, 1-3 (2005).

[3]. Tran Quoc Tien, Jens W. Tomm, Myriam Oudart and Julien Nagle "Mechanical strain and defect distributions in GaAs-based diode lasers monitored during operation" , Appl. Phys. Lett. 86, 111908, 1-3 (2005).

[4]. Tran Quoc Tien, Axel Gerhardt, Sandy Schwirzke-Schaaf, Jens W. Tomm, M. Pommiès, M. Avella, J. Jiménez, Myriam Oudart, and Julien Nagle, "Screening of high-power diode laser bars by optical scanning" , Appl. Phys. Lett. 87, 211110, 1-3 (2005).

[5]. Jens W. Tomm, Tran Quoc Tien, and Daniel. T. Cassidy, "Spectroscopic strain measurement methodology: Degree-of-polarization photoluminescence vs. photocurrent spectroscopy" , Appl. Phys. Lett. 88. 133504, 1-3 (2006).

[6]. Jens W. Tomm, Tran Quoc Tien, Myriam Oudart, Julien Nagle, and Mark L. Biermann, "Strain relaxation and defect creation in diode laser bars" , Materials Science in Semiconductor Processing 9, 215-219 (2006).

[7]. Claus Ropers, Tran Quoc Tien, Christoph Lienau, and Jens W. Tomm, Peter Brick, Norbert Linder, Bernd Mayer, Martin Müller, Sönke Tautz, and Wolfgang Schmid, "Observation of deep level defects within the waveguide of red-emitting high-power diode lasers", Appl. Phys. Lett. 88. 133513, 1-3 (2006).

[8]. Michael Kreissl, Tran Quoc Tien, Jens W. Tomm, D. Lorenzen, Anna Kozlowska, Mateusz Latoszek, Myriam Oudart, and Julien Nagle, "Spatially-resolved and temperature-dependent thermal tuning rates of high-power diode laser arrays" , Appl. Phys. Lett. 88. 133510, 1-3 (2006).

[9]. Tran Quoc Tien, Fritz Weik, Jens W. Tomm, Bernd Sumpf, Martin Zorn, Ute Zeimer, and Götz Erbert "Thermal properties and degradation behavior of red-emitting high-power diode lasers" Appl. Phys. Lett. 89, 181112, 1-3 (2006).

Conference contributions

[1]. Jens W. Tomm, Fritz Weik, Axel Gerhardt, Tien QuocTran, Jens Biesenbach, Holger Müntz, and Gabriele Seibold “Transient thermal tuning properties of single emitters in actively cooled high-power cm-bar arrays” , SPIE Proc. 5336, 125-131 (2004).

[2]. Jens W. Tomm, Mark L. Biermann, B. S. Passmore, M. O. Manasreh, A. Gerhardt, and Tran Q. Tien “Spectroscopic analysis of external stresses in semiconductor quantum-well materials” , Mater. Res. Soc. Symp. Proc. 829, 233-242 (2005).

[3]. Jens W. Tomm, Tran Quoc Tien, Myriam Oudart, and Julien Nagle “Aging properties of High-Power Diode Laser Bars: Relaxation of Packaging-Induced Strains and Corresponding Defect Creation Scenarios” CLEO®/Europe-EQEC 2005, Munich, Germany, Wednesday, JUNE 2005 Room 2, CB6-1-WED 08:30-8:45

[4]. Tran. Q. Tien and J. W. Tomm, “Optical techniques for investigation of defects in high power laser diodes” International Workshop on Photonics and Applications (IWPA-2006), Cantho, Vietnam, pp 291-297 (August 15-19, 2006).

[5]. Jens W. Tomm, Tran Quoc Tien, Mathias Ziegler, Fritz Weik, Bernd Sumpf, Martin Zorn, Ute Zeimer, and Götz Erbert, “Degradation behavior and thermal properties of red (650 nm) high-power diode single emitters and laser bars”, Photonics West 2007, San Jose, CA, USA, Jan 22-28, 2007.

Other publications and conference contributions

[1]. M. Zorn, T. Q. Tien, J. W. Tomm, H. Kissel, U. Zeimer, F. Saas, U. Griebner, M. Weyers, “MOVPE growth of semiconductor disk laser (SCDL) structures", Proc. 11th European Workshop on Metalorganic Vapour Phase Epitaxy, June 2005, Lausanne, Switzerland, F09, p. 309-311.

[2]. Thomas Koprucki, Michael Baro, Uwe Bandelow, Tran Q. Tien, Fritz Weik, Jens W. Tomm, Markus Grau, and Markus-Christian Amann, “Electronic structure and optoelectronic properties of strained InAsSb/GaSb multi quantum-well” , Appl. Phys. Lett. 87, 181911, 1-3 (2005).

Acknowledgement

The studies described in this thesis had been done at Max-Born-Insitut Berlin (MBI) with great support from the Institute.

First, I wish to convey my gratitude to Prof. Dr. Günther Tränkle Director of Ferdinand-Braun-Institut Berlin, who accepted as scientific adviser for my PhD work. I have been motivated by his encouragement and kind help.

I thank Prof. Dr. Thomas Elsässer Director of MBI for providing me an opportunity to carry out the research works at MBI.

I am deeply indebted to my supervisor Dr. Jens Wolfgang Tomm. This PhD thesis would not be possible if there were no his great supports. He gave me a chance to join his group. I learnt a lot from his daily guidance. He spent a lot of time to train me on physics and to correct my thesis. Without his help and advices, I could not overcome the challenges that I was faced with in daily life and the research works.

I also would like to thank Dr. Günter Steinmeyer (Department Head of C2 – Solid State Light Sources - MBI) for his leadership, kindness and careful correction of this thesis; Fritz Weik for very kind help and sharing opinions as well as emotion everyday.

My warm thanks go to my colleagues in my group Optoelectronic Devices for daily help, collaboration and discussion: Sandy Schwirzke-Schaaf, Mathias Ziegler, Tobias Grunske, Vadim Talalaev and Frau Regina Lendt.

During four years working in Department C2, I got a lot of good technical supports and helpful discussions from my colleagues in the department, who are very kind with me: Florian Saas, Mathias Mönster, Uwe Griebner, Herr Wolfgang Goleschny, Frau Monika Tischer, Frau Marina Friedrich, Herr Roland Müller, Herr Peter Glas, Frau Dorit Fischer, Gero Stibenz and Rüdiger Grunwald. I would like to thank them for everything.

In MBI, I already enjoyed a very nice environment with German colleagues and the colleagues come from many countries, many thanks to them: Nguyen Phuc Duong, Takuya Satoh, Kim Jineun, Wang Zhongyang, Nils Huse, Satoshi Ashihara, Matteo Rini, Corneliu-Catalin Neacsu, Anna Kozlowska, Federica Causa, Delia Massanoti, Erik Nibbering, Claus Ropers, Matias Bargheer.

I also highly appreciate the assistance from Frau Margret Lehmann, Kathleen Krüger, Herr Bernd Kinski and other MBI's staffs in administrative works.

The success of this research work is partly contributed by the efficient cooperation with Prof. Dr. Mark Biermann (Eastern Kentucky University – USA),

Alcatel III-V Laboratory (France), OSRAM Semiconductor GmbH (Germany), Ferdinand-Braun-Institut Berlin, DILAS GmbH and JOLD GmbH (Germany) in frame work of European Union projects: POWERPACK, BRIGHT.EU and BMBF projects: BRIOLAS, TRUST.

To all my friends in Vietnam, Germany and around the world, who shared difficulties, happiness and sadness with me as well as warmly welcome me and my wife in the wonderful holidays after hard working days, I would say: thanks a lot my friends.

Needless to say, I got continuously support from Institute of Materials Science Hanoi (IMS). I thank the director board of IMS Prof. Dr.Sc. Nguyen Xuan Phuc, Prof. Dr. Do Xuan Thanh, Prof. Dr. Nguyen Quang Liem. Many thanks go to Prof. Dr. Sc. Vu Van Luc, Prof. Dr. Vu Doan Mien, staffs of Semiconductor Laser Laboratory, and other colleagues in IMS and physics community in Vietnam, who indirectly contribute to the success in my PhD works.

The PhD course belongs to the Training Scientific and Technical Cadres in Institutions Overseas with the State Budget (Project 322). I would like to thank the funding from Vietnamese government.

Last but not least, I thank all people in my "*big family*" for their supports and encouragement continuously, especially my parents and my sister, who always give me love and help. Final thanks, I reserve them to my "*small family*": to my beloved, who change my life; to my baby, who has not been born at the moment but it is the great success of my wife and I.

Cảm ơn Việt Nam and ***Danke Deutschland*** **!**

Berlin, March 2007

Tran Quoc Tien

Curriculum Vitae

Personal data

Family & Middle name:	Tran Quoc
Name:	Tien
Date of birth:	July 27th, 1974
Place of birth:	Hanoi, Vietnam
Nationality:	Vietnamese
Marital status:	married

Education & Career

1980 – 1988:	Huy Van Primary & Secondary School, Dong da, Hanoi.
1988 – 1991:	Hanoi-Amsterdam High School, Hanoi
1991 – 1996:	Hanoi University of Technology
1997 – 1999:	Master of Science (Physics) in Institute of Physics, Hanoi. Master Thesis: Physical characteristics and fabricated technology of laser transmitter module used for fiber optic systems and other purposes.
Since 1996:	Researcher (permanent staff), Semiconductor Laser Laboratory, Institute of Materials Science, Hanoi.
Since 2003:	join in Max-Born-Institut Berlin (Optoelectronic Devices group) working as PhD candidate

Berlin, 15.3.2007

Tran Quoc Tien